Toward Rapid Flood Mapping Using Modeled Inundation Libraries

By

Kevin Dobbs
DPhil, The University of Kansas, 2017
M.A., The University of Kansas, 2010
B.A., The University of Kansas, 2001

Submitted to the graduate degree program in Geography and the Graduate Faculty of the University of Kansas in partial fulfillment of the requirements for the degree of Doctor of Philosophy.

_____

Chair: Dr. Stephen L. Egbert

_____

Dr. Jerome E. Dobson

_____

Dr. William C. Johnson

_____

Dr. Xingong Li

_____

Dr. Alfred Parr

_____

Dr. Jude H. Kastens

Date Defended: 20 January 2017

The dissertation committee for Kevin Dobbs certifies that this is the approved version of the following dissertation:

Toward Rapid Flood Mapping Using Modeled Inundation Libraries

Chair: Dr. Stephen L. Egbert

Date Approved: 20 January 2017

Abstract

New methods are needed for mapping floods in near real-time that leverage the increasing availability of remotely sensed data during flood disasters, availability of improved elevation data, and improvements in web-based mapping technology. There are important, ongoing improvements in elevation data production and availability that support new methods of flood disaster mapping. Concurrently, there is a rapid increase in the temporal frequency of high resolution remote sensing data that is being acquired that can also support novel application development. This study focuses on the use of prebuilt, modeled inundation libraries capable of using traditional and novel inputs as proxies for water surface elevation to produce near real-time estimates of flood inundation. Thus, the research explores potential synergies between inundation libraries and ancillary datasets with the goal of expediting the timeline for information extraction from remotely sensed data and the improving flood inundation map accuracy. It also profiles the computational cost of the modeling algorithm used. The study presents strategies for production of wide area, modeled flood inundation libraries. Gage-based interpolation methods using the FLDPLN model showed little difference in flood extent estimation accuracy between horizontal and vertical interpolation methods for FLDPLN model depth-to-flood (DTF) values. Conditioning of DTF profiles using HEC-RAS modeled water surface elevations (WSE) showed sensitivity to reference flood levels, while conditioning with two HEC-RAS model WSE profiles showed the best results. Simulation of imagery-derived flood boundary points as inputs to flood extent estimation using

interpolated DTF profiles showed very good results with a very limited number of input points. The results showed improved, asymptotic behavior when correspondence was measured with an increasing number of input points when compared to reference floods. Larger magnitude floods showed better correspondence relative to moderate magnitude floods. Baseline computational performance measures for inundation library generation with the FLDPLN models showed that longer stream segments show better overall computational efficiency. Some landscape factors can influence overall computational runtime, including proximity to reservoirs and lakes, wide floodplains, and complex tributary geometries.

ACKNOWLEDGMENTS

I would like to thank the members of my committee, Drs. Steve Egbert (my advisor), Alfred (Dave) Parr (my mentor), Jude Kastens (my close collaborator), Bill Johnson, Jerry Dobson, Xingong Li for their keen insight and suggestions in research preparations and the writing of this document. I would also like to thank Dr. Edward Martinko for his support over these many years.

This work is dedicated to my amazing children, Willow, Finn, Persephone, and Jet - you are my inspiration. Thank you so much for your understanding during my absences. Now, again, I'll try to make it up to you. And to my parents, Kay and Luther Dobbs, whom, from day one, have sacrificed so much for me and provided invaluable support in every way - thank you.

TABLE OF CONTENTS

LIST OF TABLES

LIST OF FIGURES

CHAPTER 1

INTRODUCTION

Flooding has the greatest economic and human impact of all natural disasters across all geographic scales. Although a great deal is known about the hydrologic behavior of water across the landscape and the steady and unsteady open-channel flow properties of water, implementing broad area, real-time inundation mapping has been difficult. Due to the lack of observed data, and incomplete and short-term records of stream flow, producing accurate and timely information for flood extent, severity, and timing continues to be a practical challenge (Grimaldi, Li, Pauwels, & Walker, 2016). With recent improvements in digital elevation model (DEM) datasets, gains in both the accuracy and precision of horizontal and vertical positional measurements of commercial GPS, improved computational methods for flood models, and new web-based mapping applications using real-time data, the time is right for making significant advances in flood prediction and real-time flood mapping.

Research Context

Hydrologic and hydrodynamic modeling

One and two-dimensional hydraulic modeling approaches are often used to map potential flood scenarios, most notably for risk-based assessments to help guide development decisions and to establish National Flood Insurance Program (NFIP) rates. However, these traditional approaches have not been effectively implemented over wider areas for real-time flood inundation mapping. The

National Weather Service (NWS) Advanced Hydrologic Prediction Service (AHPS) has coordinated the construction of inundation libraries using approved models such as the US Army Corps of Engineers HEC-RAS model in proximity to 92 stream gage locations for which NWS provides forecasts (Merwade, Olivera, Arabi, & Edleman, 2008b). Generally, however, these libraries are limited to an approximately two-mile stretch centered on the gage, and they are not dynamically linked to current stream conditions. This NWS approach uses measured state-discharge relationships as the basis for flood modeling along the selected stream reach, and modeled water surface profiles are used in conjunction with high-quality DEMS, usually generated with lidar data, to determine flood extents and depth grids along the reach. The selection criteria for such projects call for high quality elevation data, high risk status, and high impact potential. While a valuable exercise, these projects are expensive, generally $25-50K per stream mile, making their availability very limited.

The FEMA 100-year floodplain delineation is the primary flood risk modeling that has been performed to date in many areas of the US, though many counties have never been mapped. This activity, however, is of limited utility for responding to actual flood events. Ad hoc flood mapping is sometimes done with FEMA HAZUS-MH software at a local level, particularly in response to isolated flood events. Evaluations have shown that HAZUS modeling has a number of limitations that make it cumbersome and potentially unsuitable for inundation extent library production. These limitations include program crashes, discontinuous flood depth values, insufficient stream buffer distances, difficulty

handling backwater effects, and excessive user interaction for library development. Use of HAZUS is certainly appropriate for many applications (Gall, Boruff, & Cutter, 2007; Scawthorn et al., 2006), but for large area inundation extent library development it has many limitations.

Imagery-Based Approaches

Mapping of flooded areas using remotely sensed imagery can be an effective tool for flood disaster response (Klemas, 2014). Satellite imagery based mapping efforts vary widely, based on the flood event, and are tied to the scope of the flooding, geographic area, available resources, supporting government or humanitarian response agencies involved, weather conditions, and satellite overpass characteristics and timing, among other factors. Generally, the imagery used to map floods falls into two broad categories, microwave remote sensing, such as synthetic aperture radar, and optical remote sensing. Nearly all approaches attempt to classify image pixels as water or non-water. With few exceptions, topography and elevation data are not integrated into the classification process (Kwak, Park, & Fukami, 2014). A thorough review of all available sensors and studies is beyond the scope of this overview, so the focus will be on operational systems that use remotely sensed data to map floods.

Operationally, the Dartmouth Flood Observatory and, more recently, NASA use 250 m resolution MODIS data to monitor flooding on a global basis (Adhikari et al., 2010). This approach is subject to resolution constraints, cloud and cloud shadow contamination, and terrain shadow effects, all of which degrade the quality of the resulting data. The Global Flood Detection System, operated by

the Europe Commission Joint Research Centre (JRC), uses TRMM, AMSR, and AMSR2 coarse resolution passive microwave data to monitor flood conditions at a network of sites across the globe (Revilla-Romero, Thielen, Salamon, De Groeve, & Brakenridge, 2014; Robert Brakenridge et al., 2012; Wu, Adler, Hong, Tian, & Policelli, 2012). Although these data are not generally affected by cloud cover, the 10km pixel resolution of the data makes this approach appropriate for flood detection over wide areas, but not for fine scale inundation mapping. Remotely sensed data are also used to drive global hydrologic models, but these generally use precipitation estimates that are derived from the satellite sensors, so direct mapping of floods is not the focus (Wu et al., 2012).

A broader effort, supported by an international collaboration to make a wide array of national remote sensing assets available for disaster response is the International Charter – Space and major Disasters. Founded in 2000, the Charter is an agreement among fifteen signatory nations that each provide a limited amount of satellite remote sensing data to support disaster response effort for qualifying events across the globe. Supporting national assets include those of the US, Argentina, Japan, UK, China, DMC nations, Germany, Korea, Brazil, the EU, and Russia. The satellite assets available via the Charter are wide-ranging. To date, there have been over 500 activations of the Charter, the majority of which have been for flood events (Onyango & Uwase, 2017).

Various other governmental and non-governmental organizations use commercial and non-commercial satellite data from a wide variety of sources to map flooding using systematic classification workflows and ad hoc techniques.

Nearly all of these efforts, however, operate in the image domain without leveraging topographic data, which could be used to refine the mapped flood extent to offer an improved assessment of the conditions.

FLDPLN Model

The FLDPLN model (Kastens, 2008) is a static model that relies entirely on topographic data. First, standard fill, flow direction, and flow accumulation procedures are applied to a DEM. The model then applies a two-step, iterative backfill and spillover procedure that is seeded with stream pixels derived from the flow accumulation layer. In essence, each stream pixel is flooded to specified depth, or step size, and all upstream, connected pixels (as specified by the corresponding flow direction layer) are tagged as flooded if the reference pixel elevation value plus the step size value exceeds the boundary pixel value. This is followed by a spillover step(s), which addresses discontinuities created by flow divides. These steps are repeated in small increments (steps) to build a library of inundation extents (Dobbs, 2010). The following is a synopsis of the FLDPLN algorithm (from Kastens, 2008):

i) Initialize the depth-0 floodplain to be the stream segment. Initialize flood depth $h = dh$, for some depth increment dh.

ii) Use the topography and the gradient direction field to backfill flood outward from the floodplain boundary to depth h. Add these points to the current floodplain.

iii) Locate points on the current floodplain boundary where spillover flooding will occur. Determine the "spillover flood depth" for each spillover point.

iv) Use the gradient direction field to determine new floodwater routes originating from the spillover flood points. Halt each route when it returns

to the main channel downstream, or when it returns to the current floodplain, or when it reaches the study area boundary, whichever comes first.

v) Backfill flood each new floodwater route to its respective spillover flood depth.

vi) Add the newly flooded points to the current floodplain. Since these new points largely will have resulted from backfill flooding, it is possible that additional points will now be present on the floodplain boundary that require spillover flooding.

vii) Repeat steps *(iii)* – *(vi)* until the steady-state is reached.

viii) Increase *h* if necessary, and go back to step *(ii)*.

As noted above, a pilot study found that, for a major flood event in 2007, the FLDPLN model flood extent estimate yielded an 87.2% accuracy figure when compared to flood extent boundaries derived manually from satellite imagery acquired during the flood. The advantages of the FLDPLN model are the minimal inputs required and an architecture that makes it ideal for inundation extent library production.

Subsequent research by the author examined the effect of elevation data quality on modeled inundation extent estimation by comparing modeled flood extents for both the FLDPLN model and HAZUS using pre-lidar and lidar-derived NED data for 50 and 100-year events (Dobbs, 2010). The findings showed that elevation data quality does have an effect on the mapped flood extent for both models that is greater at lower flood levels. The author also compared modeled inundation extent estimates for HEC-RAS, HAZUS, and the FLDPLN model over a range of stream discharges, from low to high flow conditions, and

compared the mapped inundation estimates among all three models over the range of scenarios. In general, the findings indicated that the agreement between all models increases as the flood severity increases, and that the HEC-RAS and FLDPLN model are in better agreement than either are with the HAZUS model.

Current Research

The Segmented Library of Inundation Extents (SLIE) conceptual framework, outlined in Figure 1-2, serves as a general roadmap for understanding the production workflow, application areas, and research pathways. The research elements outlined in this dissertation address three different asp[1]ects of flood inundation mapping with the FLDPLN model; 1) production, 2) improved accuracy, and 3) practical applications. There are many research topics that could be explored to advance the wider production and application of FLDPLN model derived inundation libraries, but these three key topics are outlined in the objectives below.

OBJECTIVES

1) *Evaluate three techniques for calculating SLIE DTF profiles, two using simple interpolation approaches and one that conditions the profile with modeled WSE profiles. The goal is to develop improved estimation of inundation extent for flood events.*
2) *Develop and test techniques for utilizing point locations derived from modeled flood boundaries that simulate manually interpreted imagery flood boundary points. These point locations will be translated into a set of linearly*

interpolated depth-to-flood (DTF) values, which will be used to extract custom flood extents from an inundation library developed using the FLDPLN model.

3) *Profile the FLDPLN model code to characterize computational performance. The model code performance is profiled by measuring computation time and key variable size over the range of flood depth iterations for each stream segment in several test datasets.*

Objective 1 *Evaluate three techniques for calculating SLIE DTF profiles, two using simple interpolation approaches and one that conditions the profile with modeled WSE profiles. The goal is to develop improved estimation of inundation extent for flood events.*

The FLDPLN model overcomes some of the issues by estimating flood inundation based on sparse water surface profile inputs through an implicit de-trending of the floodplain elevation values. Earlier investigations by the author and others have indicated that the accuracy of inundation extent estimation may be improved by "conditioning" each stream segment DTF profile with modeled flood profiles or DEM stream surface profiles. These approaches have the potential to make the SLIE libraries more flexible in their implementation. The methods developed here for conditioning the DTF profile will be evaluated against the unconditioned approach to quantify the potential improvements in inundation estimates when using the conditioned SLIE.

Objective 2 *Develop and test techniques for utilizing point locations derived from modeled flood boundaries that simulate manually interpreted imagery flood*

boundary points. These point locations will be translated into a set of linearly interpolated depth-to-flood (DTF) values, which will be used to extract custom flood extents from an inundation library developed using the FLDPLN model.

Previous research by the author has shown that stage values at gaging stations can be transformed to water surface elevations that are then used to map flood extent when translated to DTF values for the gaged stream segments. For wide-area flood mapping the challenge becomes filling in the gaps between gaged locations. Although the FLDPLN model overcomes some of these problems over short distances by de-trending the stream elevations, the greater the distance between known water surface elevations the greater the uncertainly of the inundation estimates. This objective will examine sources of water surface elevations other than gage data that can be used as intermediate water surface elevations between gages, or even as the sole source of water surface elevations. One of the most promising sources of these data is medium to high-resolution satellite or aerial imagery of flooded areas taken during or shortly after a flood. With the increasing number of spaceborne imaging platforms that can deliver event-specific imagery in near real-time this approach warrants further evaluation. In practice, using manual image interpretation, a limited number of flood boundary locations could be selected along the affected area. The DTF values derived by intersecting these point locations with the FLDPLN model values at the same locations would be interpolated, then used for custom inundation extent estimation along the affected area.

Ultimately, the limited user input approach has a wide range of potential sources of input data. Examples include input from crowdsourced data, on-the-ground GPS locations, x-y-z location information from semi-autonomous pods, digital surface models derived from unmanned aerial systems, and others. Some users of this application also would be interested on placing an upper bound on a potential flooded area. The upper bound could then be used as a mask to limit the area under consideration for classification with traditional pixel-based or object-oriented image classification techniques. Aside from limiting the potential for errors of commission, this approach may also expedite the manual cleanup of the classified data.

Objective 3 *Profile the FLDPLN model code to characterize computational performance. The model code performance is profiled by measuring computation time and key variable size over the range of flood depth iterations for each stream segment in several test datasets.*

Although the FLDPLN model has been run routinely to develop Segmented Libraries of Inundation Extents (SLIEs), no in-depth analysis has been performed to evaluate the computational performance of the code. While many stream segments run though the entire range of iterations in a matter of minutes, some segments exhibit anomalous behavior that can lead to much longer runtimes. There is a clear need to investigate and understand the factors that yield these types of bottlenecks. Large area SLIE production will be most efficiently implemented in a distributed, parallel computing environment. This analysis will inform future phases of research aimed at migrating to a high-performance

computing environment needed for continental-scale, high resolution SLIE production. It is important to point out that to be effective rapid flood mapping tools, SLIEs must be produced well in advance of flood events over any potentially affected area.

Study Areas

Montgomery County, Kansas will be the study area for objectives one and two (Figure 1-3). The primary requirements for this analysis are the availability of high-resolution lidar-derived bare earth elevation data. The study area is rectangular in shape and covers an area of approximately 458.6 km^2 (177.1 square miles), with dimensions of 17.62 x 26.03 kilometers (10.95 mi x 16.18 mi) that stretches from the city of Independence, Kansas, on the northern end to past the city of Coffeyville on the southern end. The study area serves as a bounding box that contains the urban areas of Independence and Coffeyville that have been impacted by major floods, covers the floodplain of the Verdigris River that stretches between the two towns, and covers the areas surrounding two USGS stream gages that would be used to generate near real time (NRT) flood maps if the approach outlined in the study were operationalized. There is also one NWS stream gage situated to the north of Coffeyville that is a staff gage, read manually during extreme flood events.

The study area for objective 3 covers 11,455 km^2 of the Verdigris and Caney River watersheds in southeast Kansas (Figure 1-4), or about 5.4% of the land area of Kansas. This area covers all or most of Montgomery, Wilson, Chautauqua, Elk, and Greenwood counties, and smaller portions of Cowley, Butler, Chase, Lyon

Woodson, Neosho, and Labette counties. This area of Kansas receives from 32 to 39 inches of precipitation annually, with moderate seasonal flooding in the spring and summer months. In 2007, all the counties in the study area experienced major flooding in late June and early July. It was this event that spurred the development of flood mapping applications using the FLDPLN model. In 2008, with support from the Kansas Water Office, the FLDPLN model was used to develop a segmented inundation library (SLIE) for this 20-county area using the USGS 10m National Elevation Dataset (NED) that was available at the time.

This study area was chosen for both practical reasons that leverage the DEM pre-processing that has been done for the State of Kansas sponsored SLIE development, and because it is covers a relatively representative sample of the floodplain sizes that occur in the region. Wider floodplains, such as those that occur along major rivers such as the Kansas, Missouri, and Mississippi, to name only a few, present computation challenges that are not addressed in this study, but which will be discussed briefly in later sections.

Figures

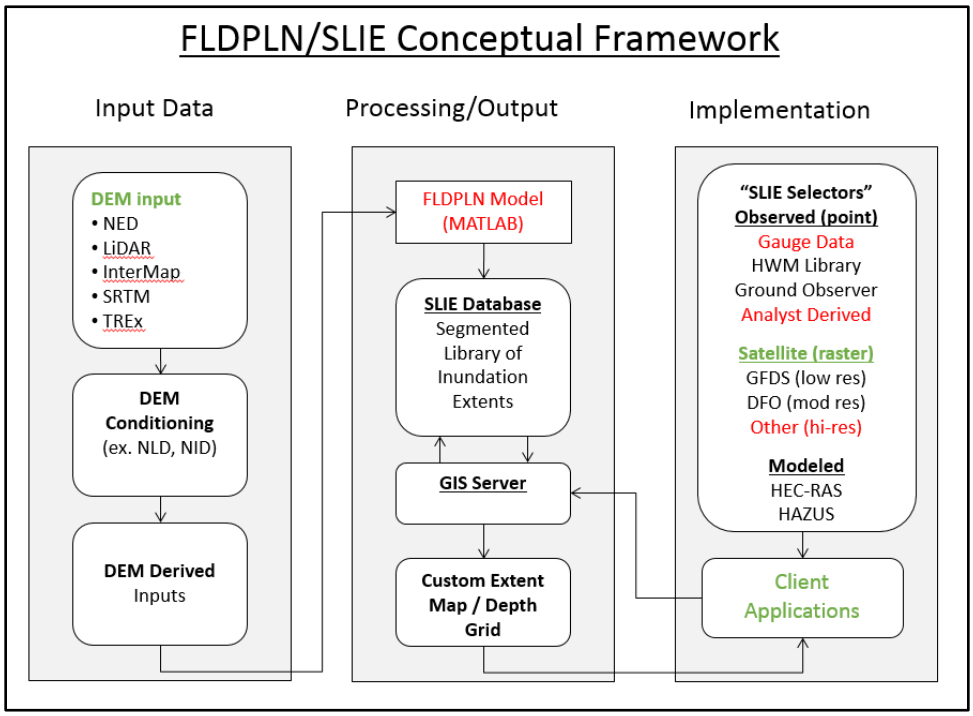

Figure 1-1: Workflow and conceptual of the FLDPLN model. Red text indicates the focus of the current work. Green text indicates elements of model data inputs supporting implementation datasets that are experiencing rapid growth and technology development.

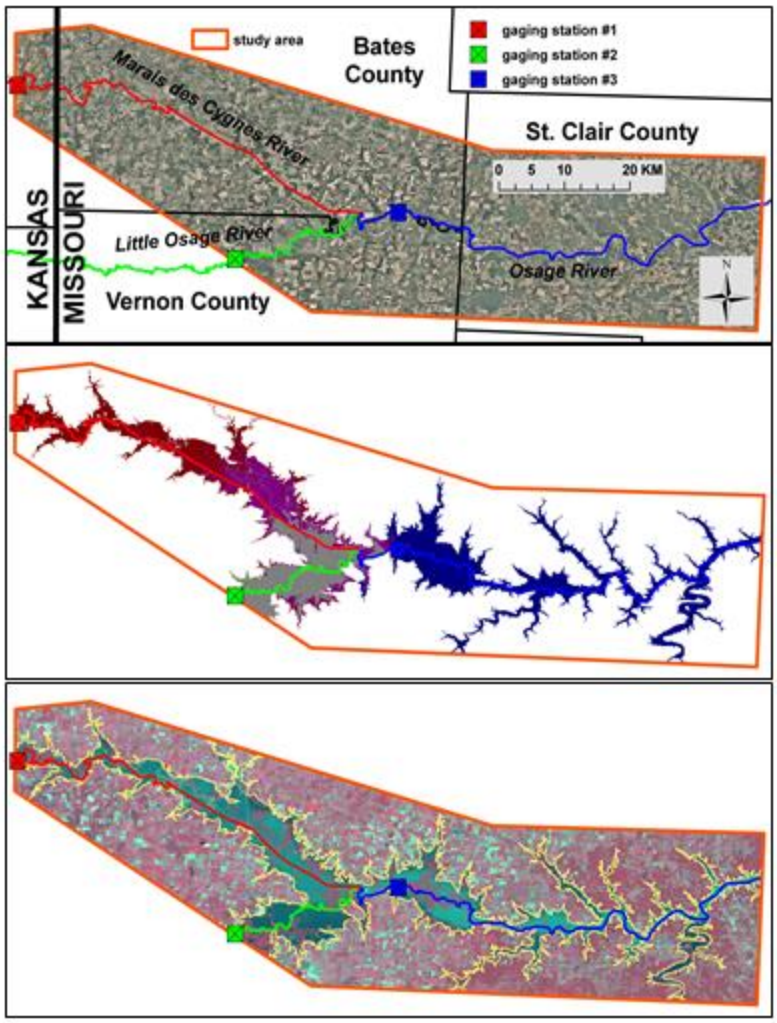

Figure 1-2: Pilot study area along the Marais des Cygnes, Little Osage, and Osage Rivers in Missouri. Floods crested in early July, several days before acquisition of the above Landsat 5 scene, which can be seen in the bottom graphic. Peak stage values were used from three USGS gaging stations as inputs to the FLDPLN model. The combined flood extent estimate for the three river segments, shown in red, blue, and green, is shown in the middle graphic. The yellow boundary in the bottom graphic corresponds to the model estimated flood extent. The estimated extent had an accuracy of 81.7%.

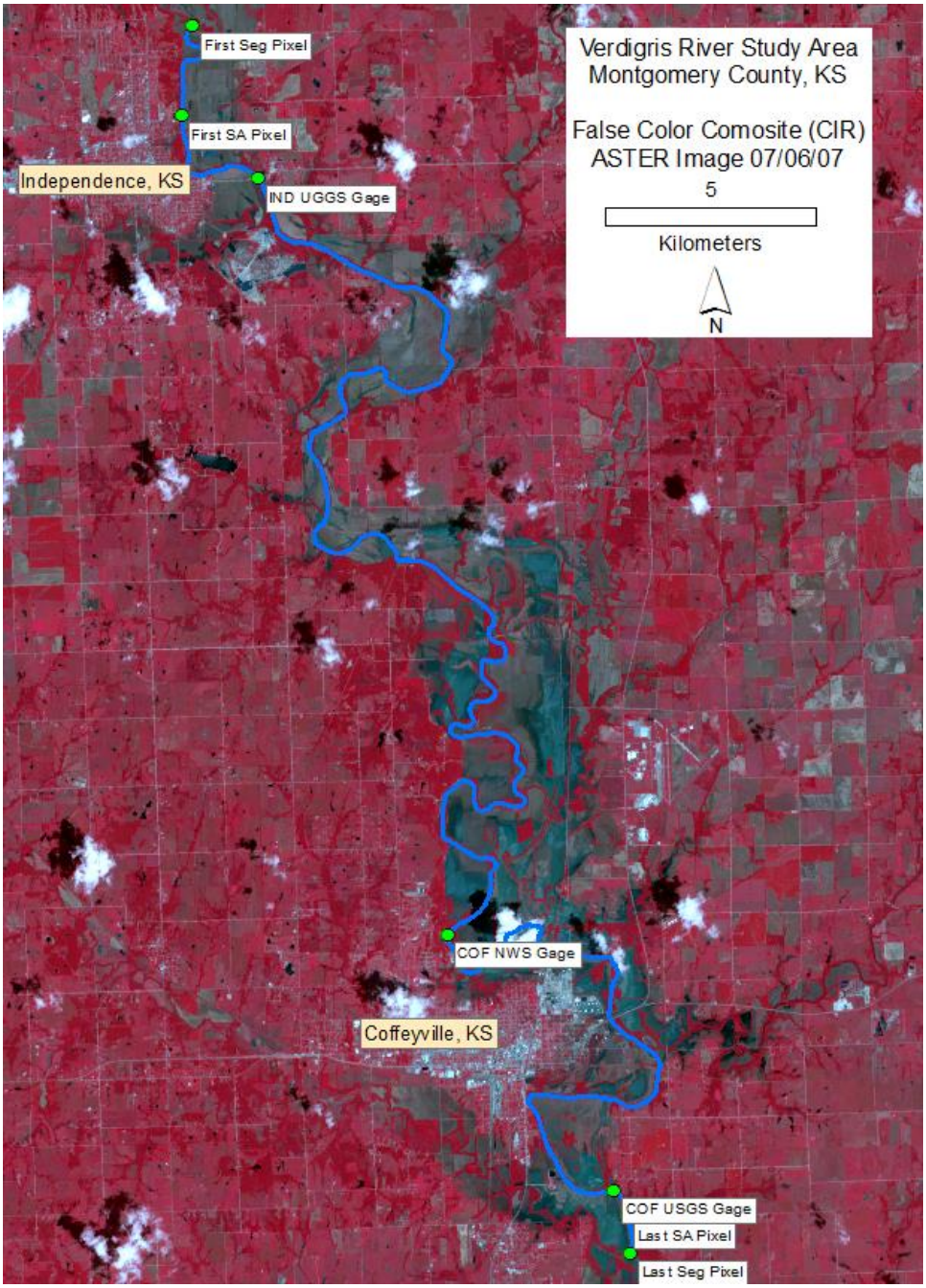

Figure 1-3: Study area for objectives 1 and 2. This area experienced major flooding in 2007, as can be seen in the post-flood imagery.

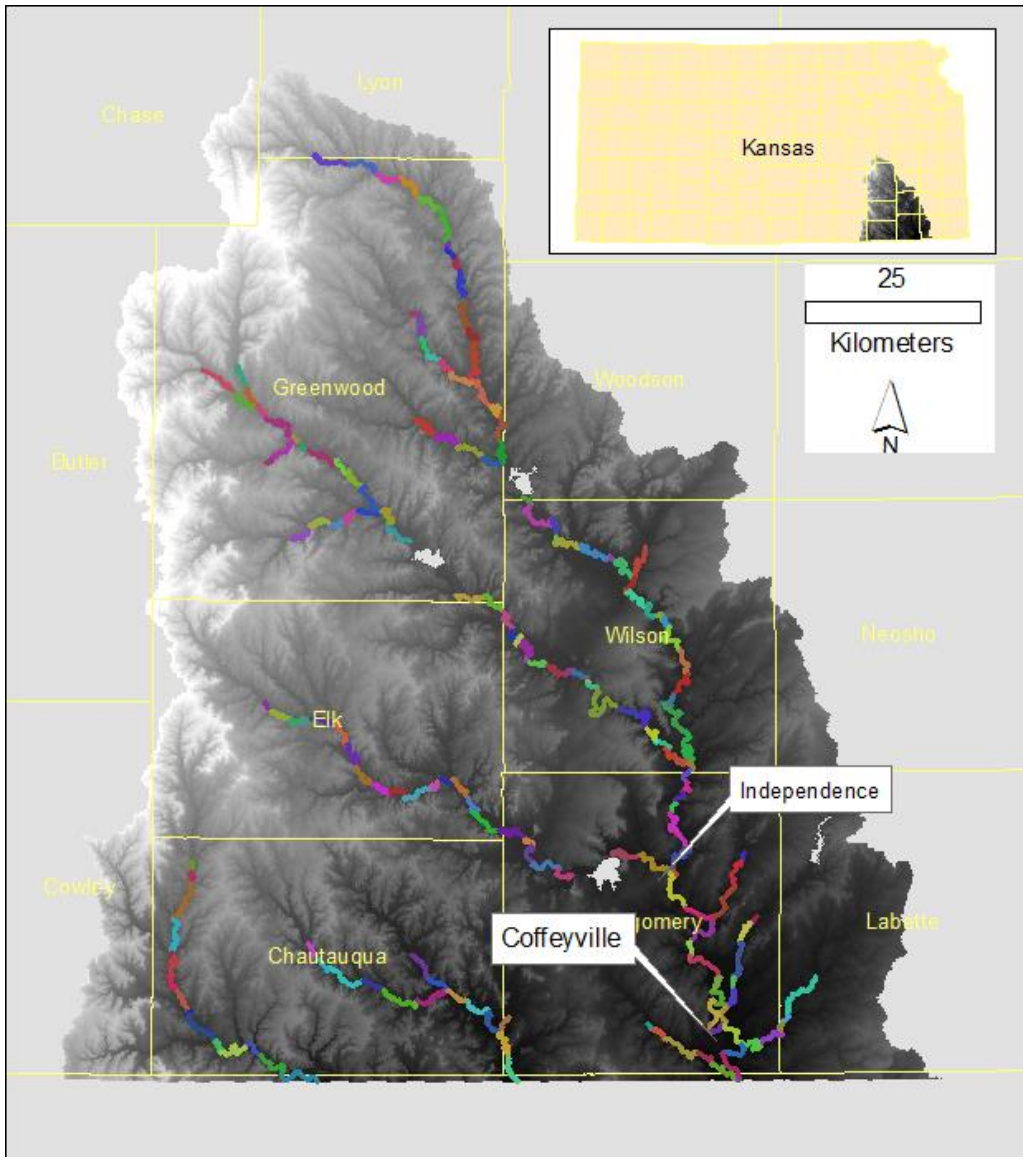

Figure 1-4: Study area for objective 3.

References Cited

Adhikari, P., Hong, Y., Douglas, K. R., Kirschbaum, D. B., Gourley, J., Adler, R., & Robert Brakenridge, G. (2010). A digitized global flood inventory (1998–2008): compilation and preliminary results. *Natural Hazards, 55*(2), 405-422. doi:10.1007/s11069-010-9537-2

Dobbs, K. E. (2010). *Evaluation of the USGS national elevation dataset and the Kansas Biological Survey's FLDPLN ("floodplain") model for inundation extent estimation.* (1477630 M.A.), University of Kansas, Ann Arbor. Dissertations & Theses @ University of Kansas; ProQuest Dissertations & Theses Global database.

Gall, M., Boruff, B. J., & Cutter, S. L. (2007). Assessing Flood Hazard Zones in the Absence of Digital Floodplain Maps: Comparison of Alternative Approaches. *Natural Hazards Review, 8*(1), 1-12.

Grimaldi, S., Li, Y., Pauwels, V. R. N., & Walker, J. P. (2016). Remote Sensing-Derived Water Extent and Level to Constrain Hydraulic Flood Forecasting Models: Opportunities and Challenges. *Surveys in Geophysics, 37*(5), 977-1034. doi:10.1007/s10712-016-9378-y

Klemas, V. (2014). Remote Sensing of Floods and Flood-Prone Areas: An Overview. *Journal of Coastal Research*, 1005-1013. doi:10.2112/JCOASTRES-D-14-00160.1

Kwak, Y., Park, J., & Fukami, K. (2014). Estimating floodwater from MODIS time series and SRTM DEM data. *Artificial Life and Robotics, 19*(1), 95-102. doi:10.1007/s10015-013-0140-y

Merwade, V., Olivera, F., Arabi, M., & Edleman, S. (2008b). Uncertainty in Flood Inundation Mapping: Current Issues and Future Directions. *Journal of Hydrologic Engineering, 13*(7), 608-620.

Onyango, M. A., & Uwase, M. (2017). Humanitarian Response to Complex Emergencies and Natural Disasters A2 - Quah, Stella R *International Encyclopedia of Public Health (Second Edition)* (pp. 106-116). Oxford: Academic Press.

Revilla-Romero, B., Thielen, J., Salamon, P., De Groeve, T., & Brakenridge, G. R. (2014). Evaluation of the satellite-based Global Flood Detection System for measuring river discharge: influence of local factors. *Hydrol. Earth Syst. Sci., 18*(11), 4467-4484. doi:10.5194/hess-18-4467-2014

Robert Brakenridge, G., Cohen, S., Kettner, A. J., De Groeve, T., Nghiem, S. V., Syvitski, J. P. M., & Fekete, B. M. (2012). Calibration of satellite measurements of river discharge using a global hydrology model. *Journal of Hydrology, 475*, 123-136. doi:http://dx.doi.org/10.1016/j.jhydrol.2012.09.035

Scawthorn, C., Blais, N., Seligson, H., Tate, E., Mifflin, E., Thomas, W., . . . Jones, C. (2006). HAZUS-MH Flood Loss Estimation Methodology. I: Overview and Flood Hazard Characterization. *Natural Hazards Review, 7*(2), 60-71.

Wu, H., Adler, R. F., Hong, Y., Tian, Y., & Policelli, F. (2012). Evaluation of Global Flood Detection Using Satellite-Based Rainfall and a Hydrologic Model. *Journal of Hydrometeorology, 13*(4), 1268-1284. doi:doi:10.1175/JHM-D-11-087.1

CHAPTER 2

EVALUATION OF STREAM WATER SURFACE ELEVATION PROFILE ADJUSTMENT APPROACHES FOR USE WITH THE FLDPLN MODEL

Abstract

In the aftermath of severe flooding events that left 20 counties in southeast Kansas declared as disaster areas in 2007, researchers at the Kansas Applied Remote Sensing (KARS) program began development of new tools to support rapid flood mapping for disaster response. The goal has been to support the unmet needs of emergency managers by developing simple tools, techniques, and datasets that add value and complement the situational awareness environments of emergency managers. At the core of this research is the FLDPLN model, developed at KARS. Earlier research has shown that the output of the model can be used to support rapid flood mapping using stage input data from the USGS and NWS gage networks. The current research examines different techniques for gage-to-gage interpolation to determine if there are advantages to implementing more sophisticated techniques that could yield more accurate flood extent estimation with gage data as the primary input. Simple horizontal interpolation, vertical interpolation, and "conditioned" interpolation techniques were examined for a stretch of the Verdigris River in southeast Kansas. Results showed that the horizontal interpolation slightly outperformed the vertical interpolation for two different discharges, and that the simple conditioned interpolation performance was sensitive to the reference flood water surface elevation. A more complex, two-profile conditioned interpolation, however, yielded superior results.

Terms and Abbreviations

[DEM] Digital Elevation Model

[DTF] Depth to flood: the output of the FLDPLN model developed by Kastens (2008) relating the minimum flood depth required to inundate a non-stream pixel from a reference stream pixel. In some circumstances the DTF can be used as a proxy for stage.

[FAC]Flow Accumulation layer: raster data derivative of DEM data with catchment area calculated for every cell.

[**FLDPLN**] FLDPLN model used to derive a segmented library of inundation extents (SLIE).

[FPP] Floodplain pixel: pixels flooded from FSPs at a given flood depth (DTF).

[FSP] Flood source pixel: stream pixels derived from a DEM-derived synthetic stream network, utilized by the FLDPN model to determine relative height above the stream.

[LISFLOOD-FP] "LISFLOOD-FP is a two-dimensional hydrodynamic model specifically designed to simulate floodplain inundation in a computationally efficient manner over complex topography."

[NED] National Elevation Dataset: US DEM dataset maintained by the USGS

[SLIE] Segmented library of inundation extents: database of outputs from running of the University of Kansas FLDPLN model.

[USGS] United States Geological Survey

[US / DS] Upstream / Downstream

Units and measures

Stream discharge (flow): given in cubic meters per second (cms) or cubic feet per second (cfs), discharge is a measure of the volume of water flowing through a vertical plane oriented perpendicular to the direction of stream flow. Often referred to as a measured quantity, it is actually a value calculated from a set of measured velocities along a stream channel cross section. When calculated for a range of river levels and combined with an adequate historical baseline of stage data (see below), discharge can be plotted on a logarithmic scale to develop a flood frequency regression equation to estimate the return period of a given magnitude flood event.

River stage: a measured quantity that relates the WSE at a monitored point on a stream (e.g. at a stream gage) to an arbitrary reference datum with a known elevation. The reference datum is usually chosen to be below the streambed to avoid negative stage values. With datum and stage information, the WSE at the gage location can be determined for any given stage.

Introduction

One of the key strengths of the FLDPLN/SLIE approach (Kastens 2008) to inundation mapping is the flexibility of the data structure. Where traditional hydraulic models require *a priori* knowledge of discharge, the FLDPLN model has been developed to be adaptable to situations when discharge measures are not available. Hence, non-traditional approaches can be developed with the SLIE that are not possible with other methods. Examination of various models shows that while often requiring discharge as one of the primary inputs, these models are not concerned with discharge itself other than as a means by which to estimate a water surface elevation (WSE) profile associated with a sequence of pre-specified stream transects (cross sections), whereby each transect receives a single WSE value. The water surface profile is used to construct a 3D surface, which then is intersected with the landscape that is represented in the DEM. Flood extent and depth can be mapped from this. This approach to flood mapping has its roots in a period when river stage was the only source of information about WSE, which is still largely the case. Consequently, modeling approaches and stream discharge estimation techniques were developed that could extend this known WSE to other parts of the stream for which there are no gages. If observed WSE values had, at that time, been available with much higher density, more direct means of flood mapping may have been developed. We now live in an era when sufficiently accurate WSE observations will be possible in ways that should be driving new approaches to flood mapping. By now, however, the academic, professional, and regulatory framework is so tied to the traditional methods of flood mapping that

most research in this area is focused on more complicated model development, more sophisticated data assimilation, and incremental improvements in traditional approaches. This then, becomes a strength of the FLDPLN/SLIE approach because is it not tied to these traditional approaches for many of the current and potential applications.

Comparing the FLDPLN model with two well-known, representative flood models, LISPLOOD-FP and HEC-RAS, will serve to highlight the differences, limitations, and advantages of each, and establish the utility of the FLDPLN model approach for wide area, near real-time flood inundation mapping addressed in this study. Each of these models, FLDPLN, LISFLOOD-FP, and HEC-RAS, serves a different purpose. In general, the differences between the models can be explored by looking at the model setup requirements, inputs, and uses of each one. It should be noted that the FLDPLN model itself is in an earlier stage of application development compared to LISFLOOD-FP and HEC-RAS, which are more established in terms of their history of use, case studies, documentation, and widespread implementation. FLDLN model research and development to date, including this study, are specifically designed to accomplish near real-time (NRT) flood extent capabilities in ways that are not practical with other approaches (Bhatt, Rao, Diwakar, & Dadhwal, 2016; Dobbs, 2010; Kastens, 2008). Thus, the intent of the FLDPLN model applications is to fill a gap in applied NRT flood extent mapping that can be implemented on scales that make it useful to emergency managers and decision makers for flood response.

The HEC-RAS model enjoys wide acceptance and is an engineering solution to flood mapping, particularly for risk-based analysis (Leon & Goodell, 2016). In general, the knowledge and experience needed to build and implement HEC-RAS is the greatest of all three models considered here. The civil engineering community routinely uses it to model open channel flow at a range of scales, from very small catchments or for engineering projects at the scale of a small commercial or residential development to a county level flood risk analysis, or larger (Moya Quiroga, Kure, Udo, & Mano, 2016). It is capable of modeling steady and unsteady flow as well as sediment transport and more.

One of the advantages of HEC-RAS is its wide acceptance due to its physical science underpinnings and generally accepted accuracy, given that the model is constructed properly. For flood risk analysis, it is one of the most commonly used models (Sarhadi, Soltani, & Modarres, 2012). HEC-RAS is an appropriate tool for studies where consideration needs to be given to flow control structures, the influence of bridges, culverts, weirs, and other constructed and natural features that have well defined flow properties, and the sizing and placement of which can have safety and financial implications. The amount of surveyed data and model preparation needed for this level of detail is quite high, but the output is beyond the scope of what the other two models are designed to provide. In that sense, HEC-RAS is quite flexible and has great value (Knebl, Yang, Hutchison, & Maidment, 2005).

The key limitations for implementing HEC-RAS for NRT flood extent mapping include the model setup time, data inputs, and cost (Cook & Merwade,

2009a). It requires a considerable amount of training and professional experience to build and run a model correctly and effectively. As such, it is not generally a practical model for mapping floods in NRT. Discharge estimates are needed for steady flow analysis, and accurate hydrographs are needed for unsteady flow. Other than a handful of National Weather Service (NWS) Advance Hydrologic Prediction Service (AHPS) sites that have been modeled for short segments around gages, there is not a significant NRT implementation of HEC-RAS models.

LISFLOOD-FP was developed to be the simplest process representation capable of simulating dynamic flood inundation (Bates and De Roo 2000). It utilizes a 1-D hydraulic routing procedure, or propagation of the downstream flood wave, and a 2-D diffusive wave routing of water into the floodplain. This is designed to be the most basic approach possible, requiring the fewest inputs to achieve the goal of flood extent mapping.

The advantages of this approach are that it requires only basic inputs: 1) a DEM and parameters that are derived from the DEM (channel slope, channel width, bankfull depth), 2) inflow discharge, typically taken from gaging station records, 3) some initial estimate of in-channel flow, 4) channel and floodplain friction coefficients (Manning's N), which are also required for HEC-RAS models, and 5) a model time step, usually between 2-20s. Relative to HEC-RAS, this is a much simpler setup that requires much less time to construct a running model and can, thus, be applied over much larger regions, assuming there is appropriate discharge information available. LISFLOOD-FP has been

implemented in a risk modeling framework aimed at determining global flood risk zones that use regression models to determine the discharge parameter(Yan, Neal, Solomatine, & Di Baldassarre, 2015). The company SSBN, which was founded by the LISFLOOD-FP developers, is currently marketing products built with LISPFLOOD-FP and associated services to clients in the insurance, reinsurance, and disaster risk reduction and resiliency markets.

The primary limitation of LISFLOOD-FP is that some information must be known about the discharge being routed through the reach. For well-gaged areas, this may not be a problem. In much of the world, however, stream gages are not available, which limits that application of the model for NRT flood modeling. There may be other ways to extract discharge estimates from satellite imagery (David C. Mason, J-p. Schumann, & Bates, 2010; D. C. Mason, Schumann, Neal, Garcia-Pintado, & Bates, 2012), which, given the proliferation of smallsats and companies (Planet Labs, OmniEarth, Skybox, etc) that are attempting to build a business model around providing daily, high-resolution imagery of the entire planet, may be an application that can provide frequently updated flood extent information using LISFLOOD-FP.

The FLDPLN model offers a way to generate a continuum of potential flood extents that cover the full range of possible floods (Kastens 2008). Because the model is applied at the stream segment level (where a segment is a portion of a stream reach), when combined, these are referred to as a Segmented Library of Inundation Extents (SLIE). This is an intermediate dataset that can be used to take inputs from sparse sources of WSE values to produce custom flood extent

estimates that represent the flood that corresponds to those inputs. The development of this concept was driven by the need for improved tools for flood mapping using satellite data during KARS efforts to support the Kansas Division of Emergency Management during the floods of 2007 (Figure 2-1 and 2-2). Subsequent research showed that traditional approaches to flood extent mapping, particularly in a flood response scenario, were inadequate to meet the needs of emergency mangers and decision makers (Dobbs 2010).

The key value of the SLIE is its unique data structure. It is substantially more adaptable than hydrologically simpler models such as the Height Above Nearest Drainage (HAND) model (Nobre et al. 2011). Within the SLIE, each potentially inundated pixel is mapped to a stream flood source pixel (FSP) with the value of the lowest flood height from that FSP that will cause that pixel to become inundated through backwater and overflow processes (Kastens 2008). Conversely, each stream pixel can be thought of as mapped to the pixels that it can flood at a lower source depth than other stream pixels, along with the values of these minimum depths (referred to as depth to flood, or DTF). What this allows, and what serves as the basis for the research presented here, is for interpolated DTF values between gaged locations to be used to create a DTF profile that can be used to create a custom flood extent map during major flood events. This and other potential applications are outlined in the conceptual framework in Figure 2-3.

The limitations of the FLDPLN model are that, from a practical standpoint, inundation library development must occur in advance of an actual

flood event in order to take advantage of the NRT flood extent mapping capabilities. Other current research aims to make headway into accelerating the FLDPLN model code performance so that appropriate scalable workflows can be designed. Additionally, current efforts are exploring the inputs that can be used to couple with the SLIE to product NRT flood extent maps. There may be opportunities for coupling the SLIE with a hydrologic model, like CREST (Xue et al., 2013), or integration of a 1-D kinematic component like LISFLOOD-FP, which may be a workable synergy.

Though the motivations for flood model development are varied, each model that is in use represents a set of compromises between complexity, practicality, and performance. From an emergency management standpoint, knowing the maximum flood extent is critical for response. Emergency managers generally are not concerned with discharge, which is just a means to an end for most models. If we can develop new techniques that don't rely on this parameter, or can couple the FLDPLN model to models that do rely on discharge but don't map extent accurately or efficiently, this opens the door to new ways of thinking about flood extent estimation and mapping. The research in this study looks to make advances in gage-based applications of the FLDPLN model for NRT flood extent mapping that is in development for wide area flood mapping. Estimating WSE values along the stream pixels between gages is necessary for SLIE implementation. In this section, we examine alternative approaches for accomplishing this task.

Objective

Evaluate three techniques for calculating SLIE DTF profiles, two using simple interpolation approaches and one that conditions the profile with modeled WSE profiles. The goal is to develop improved estimation of inundation extent for flood events.

Study Area and Data

Southeast Montgomery County, Kansas, serves at the study area. The primary requirements for this analysis are the availability of high quality DEMs and real-time USGS gage data. Lidar data were acquired for Montgomery county in fall of 2012 (published in 2013) as part of a multi-year elevation enhancement campaign supported by the State of Kansas and other local and federal partners (www.kansasgis.org) The data are available as bare earth DEMs with a ground sample distance of 2m and a stated vertical accuracy of 24cm or better at the 95% confidence level over all land cover types. These data are the most accurate elevation data available for the study area and conform to industry standards for high quality elevation data.

The study area is rectangular and covers approximately 458.6 km^2 (177.1 square miles), with dimensions 17.62 x 26.03 kilometers (10.95 mi x 16.18 mi) that stretch from the city of Independence, Kansas on the northern (upper) end to past the city of Coffeyville on the southern (lower) end (Figure 2-2). The study area serves as a bounding box that comprises the urban areas of Independence and Coffeyville that have been impacted by major floods, covers the floodplain of the

Verdigris River that stretches between the two towns, and covers the areas surrounding two USGS stream gages that would be used to generate NRT flood maps if the approach outlined in the study were operationalized (Figures 2-4,2-6). There is also one NWS stream gage situated to the north of Coffeyville that is a staff gage, read manually during extreme flood events (Figure 2-5).

Methods

Four FLDPLN model DTF profile interpolation approaches are evaluated (horizontal, vertical, and two conditioned interpolations) through the following tasks by examining two flood scenarios, a 4.8K cms flood (4.8K) and a 1K cms flood (1K), with reference and evaluation data derived from HEC-RAS 2D models (HRM) that were constructed as part of this study:

A) Base Case For general reference, the base case for this analysis is the propagation of the USGS and NWS gage stages, translated to DTF, to the entire length of the Verdigris river within the study area, with no interpolation.

B) Best Case Also, for reference, a 'best case' scenario also is evaluated by utilizing the DTF values for each FSP derived from the two HRM WSEs, thus representing the most complete knowledge of the water surface profile to generate a FLDPLN model extent.

C) Horizontal Interpolation The first interpolation approach evaluated is the horizontal, distance-weighted linear stream profile interpolation method anchored to peak stage values (translated to DTF values) at the Independence and Coffeyville USGS gages for the 2007 event (4.8K cms) and a lower

flood, the 1K cms scenario, based on the HRM WSE values at those gage locations estimated for both floods.

D) Vertical Interpolation The second interpolation approach evaluated is the vertical stream profile interpolation method applied to the 4.8K and 1K scenarios for the study area. This approach applies a linear interpolation similar to the horizontal approach in B but dependent on vertical elevation changes (relative to the gage endpoint elevation values) rather than relative horizontal distance changes between the gage endpoints.

E) Horizontal Conditioned For third interpolation approach evaluated, the 4.8K HEC-RAS model for the study area is used to condition the DTF profile by enforcing and scaling the DTF values above and below the modeled water surface profile. A 1K cms DTF profile is generated using the horizontal interpolation. The flood extent derived from applying the conditioned DTF profile is then evaluated against the HRM extent. The same process is applied to the 1K flood and extrapolated to the estimate the 4.8K profile.

F) High and Low Bound-Conditioned The last interpolation approach uses a 500 cms HRM flood WSE in conjunction with the 4.8K flood WSE to produce an interpolated profile at the 1K cms level. The 500 cms WSE profile replaces the stream elevation profile as the lower bounding condition. Modified DTF values, using the difference between the 500 cms and 4.8K WSE at the US and DS gage locations, are used.

For all B though F above, correspondence is measured by calculating the F-statistic (described below), using the HRM floods as the reference. The modeling and procedures necessary to perform each these steps are outlined below.

FLDPLN Model

The fundamental inputs to the FLDPLN model are the sink-filled DEM (FIL), flow direction layer (FDR), and flow accumulation layer (FAC). Some manual editing of the FIL layer was performed to breach flow obstructions such as culverts and dams, and to burn in detailed levee information to ensure accurate representation of flood control structures in the DEM. The FLDPLN model algorithm was applied to sink-filled DEM and FDR data for the study area to generate the DTF and FSP information that serves as the basis for the analysis. The DEM data, described above, were resampled to 5m resolution to balance the computational time required to run the FLDPLN model with maintaining sufficient resolution for flood mapping. The ArcGIS Spatial Analyst tools were used to derive the FIL, FDR, and FAC layers.

Stream segments were derived from the FAC layer using FLDPLN model code that allows the specification of minimum flow accumulation and maximum segment length, which were set to 70 square miles and 5 miles, respectively, which are the same parameters used for the Kansas SLIE developed at KARS. The minimum flow accumulation thresholding is used to define the minimum contributing land surface area needed before stream pixels are identified as part of the stream network. The segment length maximum is used to divide the stream segments into smaller pieces for processing with the FLDPLN model. This

process yielded 14 stream segments on the Verdigris River from just north of Independence to south of Coffeyville (Figure 2-2). The FLDPLN model also requires a vertical flood step size and maximum flood height be specified. These were set to 1m and 17m respectively. The FLDPLN model code was then applied using the DEM and FDR data for the study area to produce a library of inundation extents for each stream segment. This initial output is in the form of a MATLAB ".mat" file that contains a list of all pixels inundated at or below 17m, the flood height at which the pixel was inundated, and the FSPs that are linked to FPPs being inundated at that height (Kastens, 2008). The FSPs that comprise the 14 stream segments were consolidated to one segment, as were the FPPs to facilitate the further analysis. The consolidation of segments represents a simplified case of the application of a DTF profile across multiple segments. A detailed comparative analysis of multi-segment profile implementations is left for future studies.

HEC-RAS modeling

A HEC-RAS version 5.0.1 2-D model was constructed with the purpose of generating a modeled flood extent and water surface elevations for the 4.8K, 1K, and 500 cms discharge scenarios needed for the study. A 2m DEM was used for the HEC-RAS model terrain input (Figure 2-7). The 2m DEM used for this purpose was the same DEM from which the 5m DEM used in the FLDPLN model was derived. The decision to use the higher resolution DEM for the HEC-RAS model and a lower, albeit high quality, DEM for the FLDPLN model was driven by two considerations. In practice, the 5m DEM is the resolution used for most

disaster response applications of the FLDPLN model processing. This is done for reasons of computational efficiency, as noted above. The HEC-RAS model, on the other hand, was intended to be the closest representation of reality that was practicable, so the 2m DEM was used. Land use and landcover (LULC) data were used to assign Manning's roughness coefficient values (Manning's n) used in HEC-RAS. The Manning's n values assigned are given in Table 2-1. LULC data were produced by the Kansas Applied Remote Sensing Program in the 2005 timeframe using Landsat data (Peterson et al., 2008)(Figure 2-7).

The grid used for the 2-D HEC-RAS model was set to 10m, which was chosen to be small enough to model the hydraulic behavior of the flood while offering reasonable computational time. Additional breaklines were added to the model to densify the cells surrounding key landscape features, which included river channels, levees, railroad and road embankments, and other features that might significantly alter flood flow dynamics. The time step of 10 minutes was used, which yielded stable results. For the 2007 flood simulation, a hydrograph was constructed with a base flow of 200 cms, which was interpolated to the maximum discharge of 4785 cms (4.8K-HRM) corresponding to the peak discharge for the Coffeyville USGS gage from the 2007 flooding (Figure 2-8). This discharge was selected because it represents a known discharge for a recent major event so the results could be compared to remotely sensed imagery acquired shortly after the peak flooding (Dobbs, 2010). To test the conditioned DTF profile, two floods with a peak discharge of 1,000 cms (1K-HRM) and 500 cms (500-HRM) were also modeled using the same methods described above.

A raster layer of maximum WSE values was exported from HEC-RAS for each flood scenario (Figure 2-9,2-10). These data were resampled from the 2m resolution that corresponded to the HEC-RAS terrain data to the 5m resolution used by the FLDPLN model. Because the water surface is a smooth, continuous surface at this scale, no appreciable degradation of the data occurred during this process. The WSE layers were used to determine point location WSE at gage, stream, and other key locations in the study and to derive DTF values for use in conjunction with the FLDPLN model inundation output (Table2-2).

ArcGIS data manipulation

To facilitate the comparison between the FLDPLN and HEC-RAS modeled flood extents, the HRM maximum flood extent layers for the 4.8K and 1K floods were exported from HEC-RAS polygon shapefiles that were utilized in the ArcGIS environment. The flood extent was converted to a raster band interleaved by line (BIL) file with 5m resolution and snapped to match all the FLDPLN model input/output raster geometries. This ensured a direct comparison between all modeled flood extents, which was performed within the MATLAB environment. A small amount of the modeled data, 1.3 km from the northern and 0.25 km from the southern areas of the study area, were cut from the data layers to minimize the effects of modeling boundary conditions and to ensure complete overlap between the HEC-RAS and the FLDPLN modeling areas (Figures 2-9 and 2-10).

Stream profile

The stream profile is a key tool in all the analyses outlined below. Stream pixel locations along the merged segment, described above, are assembled into an ordered list, from upstream (US) to downstream (DS), and utilized for a range of analysis steps outlined below. Because these pixels are derived from a sink-filled DEM, the corresponding stream surface (as represented in the FIL DEM) is guaranteed to have corresponding elevation values that decrease from US to DS, or in some cases are unchanged between successive pixels. Small level areas occur naturally in pools between stream riffles. Larger flat areas can occur in reservoirs or upstream of inline dams.

In this study the overall stream segment comprises 11,220 5m pixels. There are 9765 pixels from the US gage to the DS gage (G2G). There are 10,516 stream pixels in the subset of the study areas that is used for F-statistic calculations. Table 2-2 gives the pixel list order for key locations along the stream profile. These stream profile pixels serve as the flood source pixels (FSP) for the FLDPLN model and are referred to interchangeably as steam pixels or FSPs, depending on context.

Interpolation

Two sets of horizontal, vertical, and conditioned interpolations were performed, one each for the 4.8K and 1K cms scenarios. One additional two-profile bound-conditioned case was also evaluated. In all cases below, the interpolated values are calculated between FSP #1156 and FSP #10921. These

correspond to the gage locations along the stream segment. For the purposes of this study, the DTF values used between those locations and their respective endpoints, FSP #1 and #11220, were set to the value at the respective gage. This was used as a reasonable approximation where no additional information was available, which would be the case in a practical application of the technique for two gages. This is not deemed to have a significant impact on the F-statistic calculation because the results are clipped to a more restricted study area for the F-statistic determination at FSP #534 and #11050, respectively.

Horizontal interpolation

The horizontal interpolation is the most straightforward of all the techniques. It involves determining the starting and ending DTF values, then applying a simple linear interpolation based on position along the streamline to determine the DTF values associated with each intermediate FSP. The DTF for stream pixels between FSP_a and FSP_b was determined using the following formula:

$$DTF_i = DTF_a + (DTF_b - DTF_a) * (D_{ai} / D_{ab}) \quad (1)$$

where D_{ab} is the raster distance between upstream FSP_a and downstream FSP_b, D_{ai} is the raster distance between upstream FSP_a and FSP_i along the stream pixel path between FSP_a and downstream FSP_b, and DTF_a and DTF_b are the DTF values for the FSP_a and FSP_b (gages), respectively. Distance along the raster flow path is determined by assigning a value of distance = 1 to FSPs with corresponding FDR values of 1,4,16, or 64 (cardinal directions) and distance=1.4142 for corresponding FDR values of 2,8,32, and 128 (diagonals). Although it is not clear that inclusion of diagonal distance is necessary in this case, it was included in the

calculation. Because this distance is used for scaling purposes only, it is likely that with or without this step, the scaling would be similar because of the way the FDR algorithm determines the stream pixels at this scale. The FIL pixels are 5m resolution and the stream channel is significantly larger than that. The result is a streamline that obeys the FDR map, but does not necessarily map the shortest route over the steam surface.

Vertical interpolation

The vertical interpolation is conceptually like the horizontal interpolation, but incorporates changes in elevation into the calculation. This interpolation method makes changes in the DTF profile values only where there are elevation changes in the FIL DEM stream profile. This is accomplished using the following equation:

$$DTF_i = DTF_a + (DTF_b - DTF_a) * (E_{ai} / E_{ab}) \quad (2)$$

where E_{ab} is the elevation change between upstream FSP_a and downstream FSP_b, E_{ai} is the elevation change between upstream FSP_a and FSP_i along the path between FSP_a and FSP_b, and DTF_a and DTF_b are the DTF values for FSP_a and FSP_b (gages), respectively.

Conditioned

The conditioned interpolation method uses the horizontal interpolation method, as described above, but uses a modeled WSE profile as the reference instead of the FSP DEM stream elevation profile. In the 4.8K conditioned case, the difference between the 1K HRM WSE and the 4.8K HRM WSE at the US and DS ends serves

as DTF_a and DTF_b, respectively. The same horizontal interpolation is applied as described in (1), above. The DTF profile values are then added to the difference profile of the corresponding HRM WSE and FSP elevations to yield the conditioned DTF profile. For the 1K conditioned this is repeated, but with the 4.8K HRM WSE as the reference. This has the effect of removing the variability of the FSP elevation profile for the resulting WSE profile.

Bound-conditioned

The bound-conditioned case uses the same method as the conditioned, but replaces the lower bound, substituting the stream elevation profile with a modeled WSE profile that is lower than the scenario under consideration. In this study, the 500 cms HRM profile was used. This profile was chosen because it represents a WSE that is at or near bankfull conditions. Because of this, it serves as a reference that is a substantially smoother alternative to the stream elevation profile, without representing the hydrodynamic effects of overbank flow and the effects that this would have on the higher flood profiles. This is the simplest implementation of the bound-conditioned method. More on this will be discussed in the results section.

F-statistic calculation

First, a list of all BIL file indices is generated that corresponds with the refined study area in Figures 2-9 and 2-10. This is used to mask the pixels in the HRM scenarios to limit the area of analysis to the refined study area. Once all stream pixels have DTF values assigned based on the interpolation techniques outlined above, calculation of the corresponding F-statistic is performed by querying the FPP data file for the set of floodplain pixels linked to FSP_i that

correspond to the condition $DTF_{FPPi} <= DTF_i$ for each i. This list is first intersected (masked) with the list of pixels in the refined study as outlined above. The resulting flooded pixel set is intersected with the corresponding, masked HRM pixels list. The count of pixels in the resulting intersected list is tallied and used to calculate the F-statistic correspondence (Bates & De Roo, 2000; Cook & Merwade, 2009b; Horritt & Bates, 2001; Kastens, 2008; Tayefi, Lane, Hardy, & Yu, 2007):

$$F = 100 * (A_{op}/(A_o+A_p-A_{op})) \quad (3)$$

where A_o: observed area of inundation (model A)

A_p: predicted area of inundation (model B)

A_{op}: area that is both observed and predicted as inundated.

An F-statistic of 100 would indicate perfect correspondence between two flood extents. Areas of non-correspondence will lower the F-statistic score in proportion to the size (area) of non-correspondence. The correspondence statistics are summarized, analyzed, and reported.

Results

Before considering the result of the interpolation and flood extent correspondence analysis, it is beneficial to consider an analysis of the FLDPLN model output data. Figures 2-11:13 were prepared to offer insight into the potential behavior of the model at various flood levels. Beyond a deeper understanding of the data, this will also aid in design of future applications and analysis.

The FLDPLN model output is structured in a way that creates a one-to-many relationship between a given FSP and all FPPs that it is linked to. For instance, there are 11,220 FSPs that comprise the overall study area steam pixels, and there are 9,284,741 FPPs that are inundated at or below 17m (the upper limit for this study), per the output of the FLDPLN model. On average, then, each FSP would in theory be linked to 828 FPPs. What Figure 2-14 indicates, however, is that many FSPs are linked to a small number of FPPs at lower DTF levels, particularly within the channel, with fewer and fewer having any influence at all at higher flood levels. This reaches a minimum in the last several meters of the DTF range with fewer than 200 FSPs. The implication for the interpolation analysis below is that for the DTF values generated for the full stream profile, only a small number of them have any affect at all in determining the flood extent boundary for relatively large events. A review of Figures 2-12:14 shows that even fewer FPSs control most the flood extent boundary determination (note that the y-axis for these figures is on a log scale).

Figure 2-15 gives an indication of both the behavior of the FLDPLN model and the channel and floodplain morphology. The initial spike at 1.25m and below is caused by the addition of stream pixels surrounding the FSP pixels. Once this occurs, few new pixels are recruited until the bankfull condition is exceeded at about 6m. This value will vary by stream morphology, which is dependent on a range of factors. Once paths are established that give access to the floodplain, there is a sharp rise in the incremental recruitment of FPP that continues through a peak at around 10m. The floodplain valley morphology dictates that the rapid

lateral spreading will diminish and give way to a more even spreading that stabilizes at about 12m.

The FAC profile is presented in Figure 2-16. The jumps in FAC values correspond to the intersection of significant tributaries with the stream profile. The increase in FAC value is proportional to the size the tributary catchment. Because this study does not examine more complex cases where a significant discharge is added to the stream from tributaries between the gage locations, the FAC profile does not have a significant impact on this study. It is worth noting, though, that the inundation area in the floodplain of a tributary can add a significant amount of area to the inundation estimate. Previous studies have shown that mapping backwater in tributaries is a function that the FLDPLN model can perform effectively (Kastens, 2008).

The DTF profiles in figure 2-17 show the effect of implementing the horizontal and vertical interpolations based on the values in Table 2-1. The vertical DTF interpolation mimics the stream FIL elevation profile shape. When these DTF values are added back to the stream elevation profile, both DTF interpolations take on the shape of the stream elevation profile, which is covered later in Figures 2-20 and 2-21. The FLDPLN model profiles in these figures, however, should not be considered as WSE profiles in the sense that the HRM represents them. As noted above, the influence that the DTF profile has on the boundary extent is highly correlated, but not in the strict sense of the HRM. More research is needed to create tools to quantify and visualize this relationship and behavior, but that is beyond the scope of this study. The difference between the

horizontal and vertical interpolation along the stream profile is quantified in Figure 2-18. Clearly, the presence of the low-head dam at FSP #6575 has a significant influence over the vertical interpolation and should be consider as a factor in the results below.

Base case

The base case results are presented in the maps in Figure 2-19. Because of the very wide distribution of flood extents represented here, no F-statistic was calculated. Although previous work has shown that single point DTF inundation extent estimation can be useful in a localized area (Dobbs, 2010), over the large study area with a more diverse landscape, this method is would not be effective in this case.

[Tables 2-3 and 2-4 summarize the F-static findings for all cases presented below, but individual findings are given in line with the test for convenience]

Best case

The 'best case' scenario yielded interesting and informative results. For the 4.8K cms flood, the hypothetical 'best case' scenario in which WSE elevations are known for all FSP and translated to DTF values using the difference between the WSE and the stream elevation, an F-statistic (3) of 89.4 was calculated (note that the area figures are given in km^2, while the F-statistic itself is unitless):

Aop= 89.92
Ao = 99.92
Ap= 90.60
Fstat = 89.4

Most of the error appears to be due to underprediction.

The 'best case' scenario for 1K cms flood is substantially lower than that of the 4.8K flood, with an F-statistic of 76.4:

Aop= 54.68
Ao = 68.47
Ap= 57.76
Fstat = 76.4

This, however, agrees with previous studies that show that correspondence between FLDPLN model results for the single DTF case agree better with modeled and observed flood extents at higher flood levels (Dobbs, 2010). It is interesting to note that in separate results that relied on flood boundary points to inform DTF interpolation, the performance was slightly better, nearing an F-statistic of 85.0 for a similar number of inputs (~10,000). This indicated that an adjustment factor may need to be applied to WSE points. The explanation for this may lie in the way a FSP "spreads its influence." There is a subtle, yet fundamental difference between the way a HEC-RAS 1-D model, for instance, determines inundated areas and how the FLDPLN model is being used here. The HEC-RAS model forces the modeled water surface to extend laterally out from the stream, whereas the FLDPLN model approximates this by using DTF and relies on the model algorithm to locate pixels in the floodplain with that relative height differential, but pixels that are identified that fit that criteria are only determinable via the FDR layer. Instead of a lateral extension of the WSE elevation, this influence could be up the valley in the floodplain, or even down the valley. This difference, as noted, is subtle, but it could account for the differences

noted above. The other study noted, by starting at the flood extent boundary, not the stream, is accounting for this offset already.

Horizontal Interpolation

The error was split between over and under prediction for horizontal interpolation method in the 4.8K scenario, but it was close to the best case scenario.

Aop= 89.92
Ao = 99.92
Ap= 90.60
Fstat = 89.4

The WSE profile in figure 2-20 shows that there is generally good agreement in the northern and southern ends of the study area. There are several reasons that this may be. The width of the floodplain is relatively narrow in those areas compared to the middle portion of the study area, so these areas are generally associated with steeper valley walls that limit the opportunity for disagreement. These areas are also closest to the gage locations that serve as anchor points for the interpolation. It is reasonable that these areas would be expected to have the best agreement.

The performance of the 1K horizontal interpolation mirrored that of the 4.8K relative to both the best case and the vertical interpolation, with an F-statistic of 66.2, compared to the 76.4 and 65.9 of the others, respectively.

Aop= 48.87
Ao = 68.47
Ap= 54.22
Fstat = 66.2

The DTF profile indicates that the low head dam can produce divergences between horizontal and vertical methods. This is particularly important because, as Figure 2-21 shows, the stretch of river along which the pooling occurs behind the inline dam is also the stretch that has the narrowest spread in flood depth, according to the difference between the 500 cms and 4.8K cms WSE output of the HRM. The floodplain is also widest in this area, as shown in figures 2-9 and 2-10. This could amplify the effect of the stream surface elevation anomaly on the FLDPLN model flood extent estimation. This is covered in more detail in the bound-conditioned discussion below.

Vertical Interpolation

The vertical interpolation exhibited slightly better agreement than the horizontal interpolation, with an F-statistic of 85.3.

Aop= 90.34
Ao = 99.92
Ap= 96.36
Fstat = 85.3

This method produced more overlap than the horizontal interpolation. It is not clear what effects may be due in part to the low-head dam that is located at the NWS gage location (Figure 2-5). The stream elevation profile shows this feature quite clearly.

For the 1K scenario, the vertical interpolation correspondence was slightly lower than for the horizontal interpolation, with an F-statistic of 65.9.

Aop= 49.44
Ao = 68.47
Ap= 56.02
Fstat = 65.9

This result is not much different than the 66.2 yielded by vertical interpolation.

Conditioned

The single profile conditioning case yielded substantially different results between the two scenarios. The 4.8K case, where the 1K WSE profile was used as a reference to create the 4.8K DTF profile, has an F-statistic of 92.8, which is slightly better than the 'best case' scenario (Figure 2-22):

Aop= 96.84
Ao = 99.92
Ap= 101.31
Fstat = 92.8

In contrast with the best case example, the conditioned profile appears to derive most of the error through overprediction, whereas the best case derives most of it its error from underprediction

The 1K conditioned case, however, performed very poorly compared to all other cases, with an F-statistic of 37.7 (Figure 2-23):

Aop= 26.09
Ao = 68.47
Ap= 26.78
Fstat = 37.7

Examination of predicted, observed, and correspondence figures above, along with Figures 2-15 and 2-21 offers valuable insight into why this occurred. The HRM shows 68.47 km^2 of flooded area for the 1K flood. The conditioned FLDPLN model, however, shows only 26.78 km^2 of flooded area. With the Aop value of 26.09 km^2 nearly all the area predicted by the FLDPLN model corresponded with HRM pixels, but HRM flooded area was more than twice the

size of that predicted by the FLDPLN model. In Figure 2-21, the 1K horizontal conditioned profile dips below the 1K WSE profile from about FSP #2400 to just after the low head dam at FSP #6575. Figure 2-23 also shows a narrow range of HRM WSE values in the area, as noted above. In addition, this puts the interpolated DTF values below the bankfull WSE. Consequently, this area is not flooded, which is the zone that accounts for a large percentage of the flooded area for the 1K flood. This example highlights the sensitivity of the interpolation approach to the DTF profile being above or below the bankfull stage.

Conditioned: High and Low

One way to counter the conditions highlighted in the previous example is to bound the interpolation between two DTF profiles derived from HEC-RAS WSE profiles (Figure 2-24). In the conditioned examples above, the stream elevation profile serves as the reference datum for DTF. Here this is replaced by a HRM 500 cms WSE. As noted above, this level was chosen to be at approximately bankfull stage for most of the study area. Using this approach, an F-statistic of 76.6 was achieved:

Aop= 55.04
Ao = 68.47
Ap= 58.40
Fstat = 76.6

As with the best case scenario, this approach under predicts, which accounts for a majority of the disagreement. The WSE profile in Figure 2-25 shows good correspondence with the HRM profile, with no observable influence of the stream elevation profile. As noted above, other research that examined using simulated

flood boundary points to inform the interpolation of the DTF profile was able to achieve an average F-statistic of nearly 85.0 for the same scenario. This would indicate that use of WSE at the stream centerline may require some type of gain and/or bias to improve an F-statistic correspondence greater than those achieved in the current study.

Conclusions

These findings reflect earlier studies showing that when using limited WSE data input to guide DTF profile adjustments, FLDPLN-based inundation extent estimation is more reliable for higher magnitude floods than for low magnitude floods (Dobbs, 2010). The 4.8K-FPM showed better agreement with the reference flood extent than did the 1K-FPM, regardless of the interpolation method used. For both flood scenarios, the horizontal interpolation slightly outperformed the vertical interpolation. Though it would be worthwhile to apply the same comparison in other cases, there does not appear to be a clear benefit to using the vertical approach. The caveat, though, is that the low head dam at the NWS gage may have impacted the results, which would not be a typical scenario in most places. But, because of the common occurrence of these features, it would be worthwhile to study their impact on FLDPLN model performance more closely.

Although the goal of the FLDPLN model approach to mapping floods has been to keep the methods as simple and scalable as possible, the results above point toward the need and opportunity for innovative ways to improve the approach. For example, it is apparent that some method to reduce the influence of

the stream elevation profile is needed to improve the sparse DTF input approach. The properties exhibited in Figure 2-15 suggest that it may be possible to utilize a moving window along the FSP data to determine the localized DTF that corresponds with bankfull conditions. This might be utilized to simulate the bankfull reference, as done in the bound-conditioned example above, but without having to rely on other models that would add much greater complexity and expense to wide area, real-time flood mapping capability development. Also, identifying specific FSPs are that linked to the most FPPs might help identify specific elements of the profile that are responsible for sensitive or important areas in the floodplain.

The magnitude of the influence of the low head dam on the interpolation results is not clear. Follow-on work should include applying the techniques utilized in this study to an areas that have no inline structures, and a wider variety of stream and floodplain morphologies. In conjunction with the findings of this study, these investigations can also help guide procedures for handling inline structures, of which there are many, to enable scalable solutions that provide reliable, actionable information for emergency managers.

The conditioned and bound-conditioned examples were evaluated specifically because, in many areas, HEC-RAS or other modeled 100-year flood WSE may be available as a byproduct of the FEMA National Flood Insurance Program and RISKMAP programs. If these data can be easily incorporated into real-time application to produced improved flood inundation estimate, this is certainly worth pursuing given the results of the bound-conditioned case.

Tables

Table 2- 1: HEC-RAS Manning's n coefficients used for HEC-RAS 2D modeling.

Land Cover	Base Manning's n
Cropland	0.035
CRP	0.040
Grassland	0.030
Other	0.040
Urban industrial / commercial	0.050
Urban open land	0.030
Urban residential	0.045
Urban water	0.025
Urban woodland	0.100
Water	0.035
Woodland	0.100

Table 2-2: This table shows key values at FSP locations along the study area streamline. DTF values used for interpolation are highlighted in red. These values were extended to the segment endpoints on the DTF profile when calculating the F-statistic. Blue values represent overall segment extrapolations values, which are extended directly from gage values.

	StreamPx	FIL DEM	HR WSE 4.8k	DTF4.8k	HR WSE 1k	DTF1k	HR WSE 500	DTF500
Segment Start	1	221.95	N/A	14.97	N/A	11.53	N/A	10.28
US HR Area Bnd	274	221.12	236.04	14.92	232.38	11.26	230.17	9.05
US Study Area Bnd	534	220.35	234.87	14.52	231.73	11.38	230.29	9.94
Indep USGS gage	1156	219.06	234.04	14.97	230.59	11.53	229.34	10.28
Coff NWS gage	7731	212.94	221.99	9.05	219.71	6.77	218.79	5.85
Coff USGS gage	10921	206.16	216.63	10.47	213.48	7.32	211.15	4.99
DS Study Area Bnd	11050	205.83	214.70	8.88	212.47	6.64	210.43	4.60
DS HR Area Bnd	11089	205.72	214.21	8.48	212.06	6.34	210.01	4.29
Segment End	11220	205.42	N/A	10.47	N/A	7.32	N/A	4.99

Table 2-3: F-statistic value calculated for the 4.8K interpolations. The 'Best Case' uses the WSE at all FSP locations at DTF values in the profile, as though there were a gage at every FSP. The horizontal and vertical interpolations use equations (1) and (2), respectively, to calculate DTF values along the FSP profile between gage locations.

	4.8K cms Gage Interpolation F-Statistic			
	Best Case	Horizontal	Vertical	Horiz Cond
Aop	89.92	89.00	90.34	96.84
Ao	99.92	99.92	99.92	99.92
Ap	90.60	97.34	96.36	101.31
F-statistic	89.4	82.2	85.3	92.8

Table 2-4: F-statistic values calculated for the 1K interpolations. The 'Best Case' uses the WSE at all FSP locations at DTF values in the profile, as though there were a gage at every FSP. The horizontal and vertical interpolations use equations (1) and (2), respectively, to calculate DTF values along the FSP profile between gage locations.

	1K cms Gage Interpolation F-Statistic				
	Best Case	Horizontal	Vertical	Horiz Cond	H/L Cond
Aop	54.68	48.87	49.44	26.09	55.04
Ao	68.47	68.47	68.47	68.47	68.47
Ap	57.76	5.42	56.02	26.78	58.40
F-statistic	76.4	66.2	65.9	37.7	76.6

Figures

Figure 2- 1: Aerial photographs taken during the peak flooding in Montgomery County in July of 2007. The top two photos show oil release from a refinery in Coffeyville, which flowed south in the Verdigris River into Oklahoma. (www.kansasgis.org)

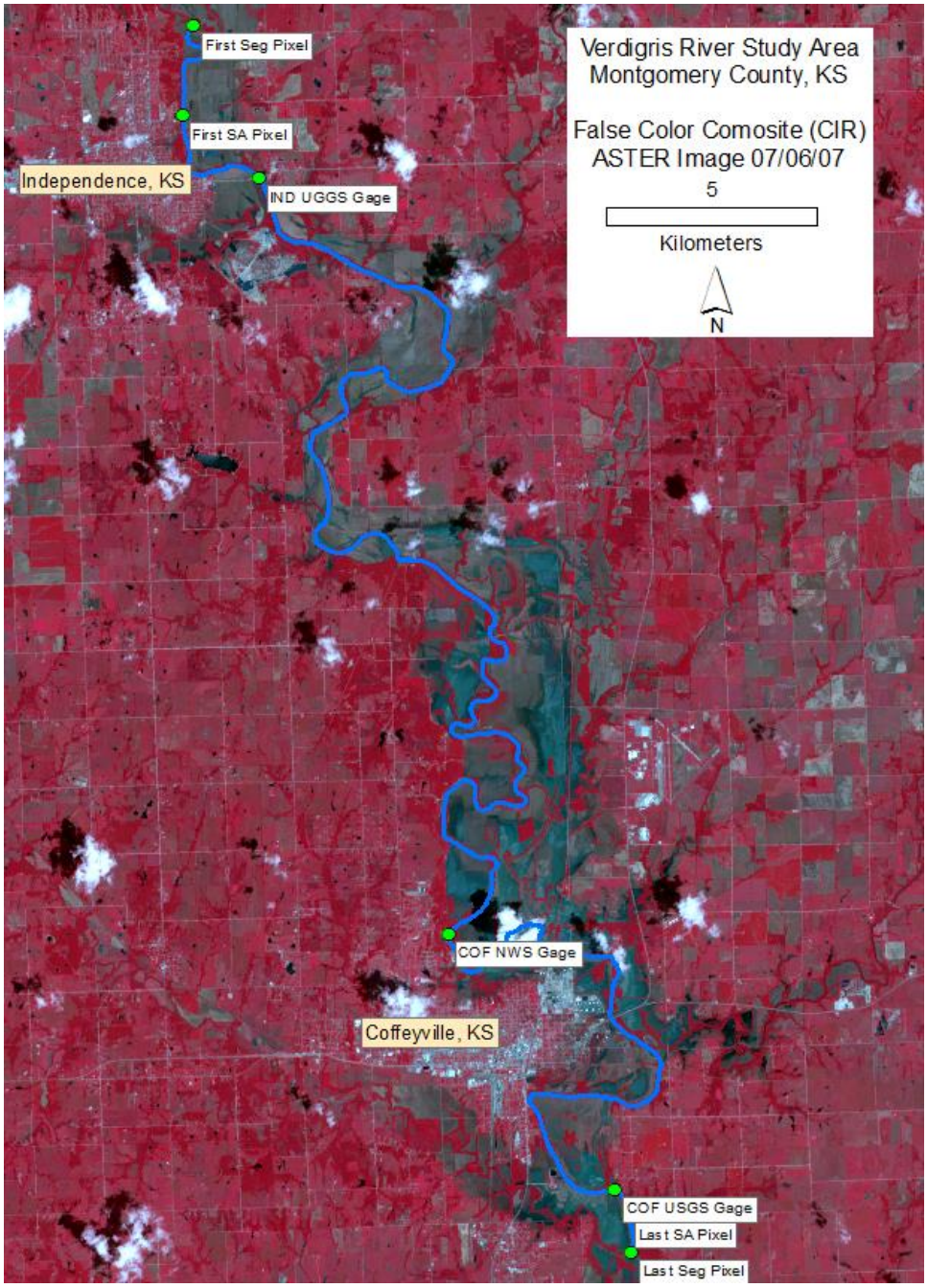

Figure 2- 2: ASTER flood image. The base image is a color infrared, 15m resolution ASTER image acquired on July 6th, 2007, four days after flood crest. Dark areas along the Verdigris River are either standing water still pooled in the floodplain, or areas denuded of vegetation by flood waters. Brighter red areas within the flood zone are woodland canopies that are minimally impacted by flood waters.

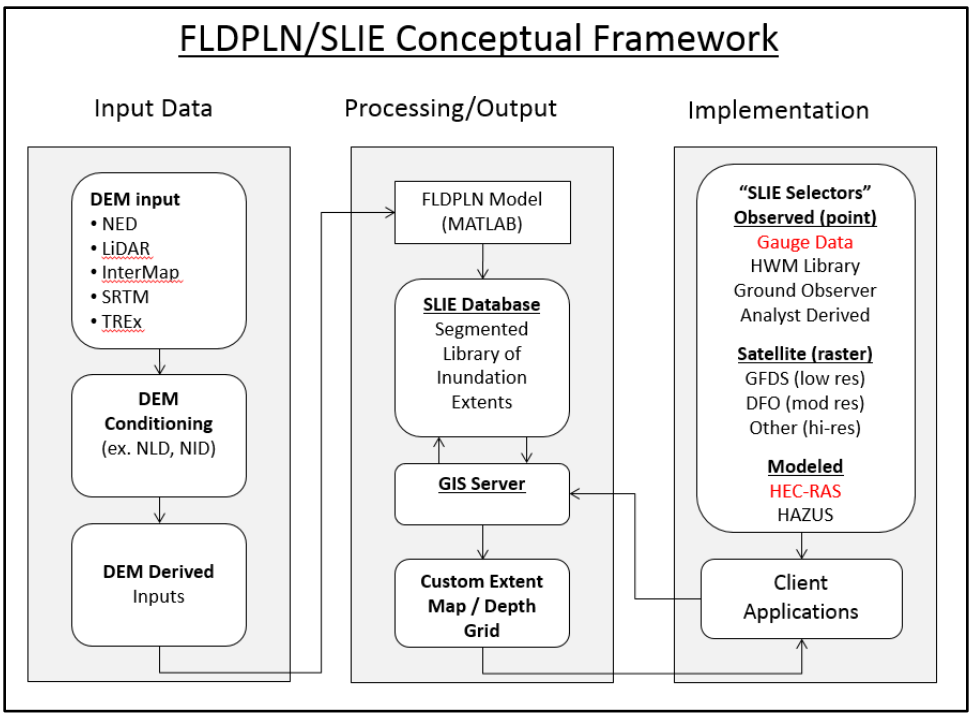

Figure 2- 3: Workflow and conceptual of the FLDPLN model. Red text indicates the focus of the current work.

Figure 2-4: Location of the Independence UGSS gage on the Verdigris River, to the east of Independence, KS.

Figure 2-5: Location of the NWS staff gage on the Verdigris River, to the north of Coffeyville, KS. The low-head dam can be seen across the width of the stream to the south of the gage location.

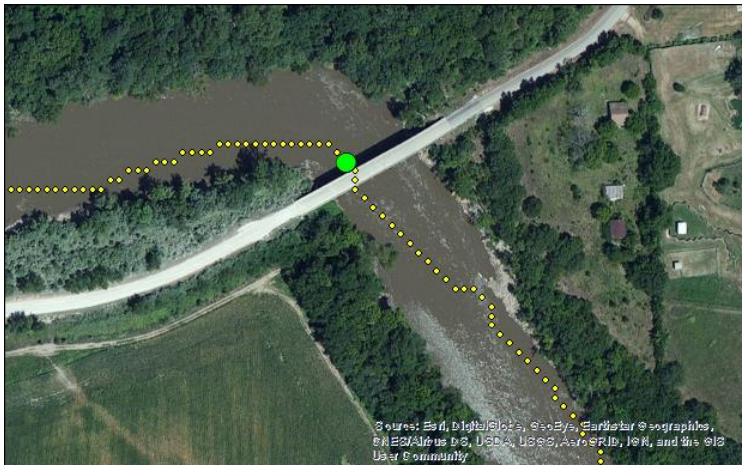

Figure 2-6: Location of the UGSS gage on the Verdigris River, to the south and east of Coffeyville, KS.

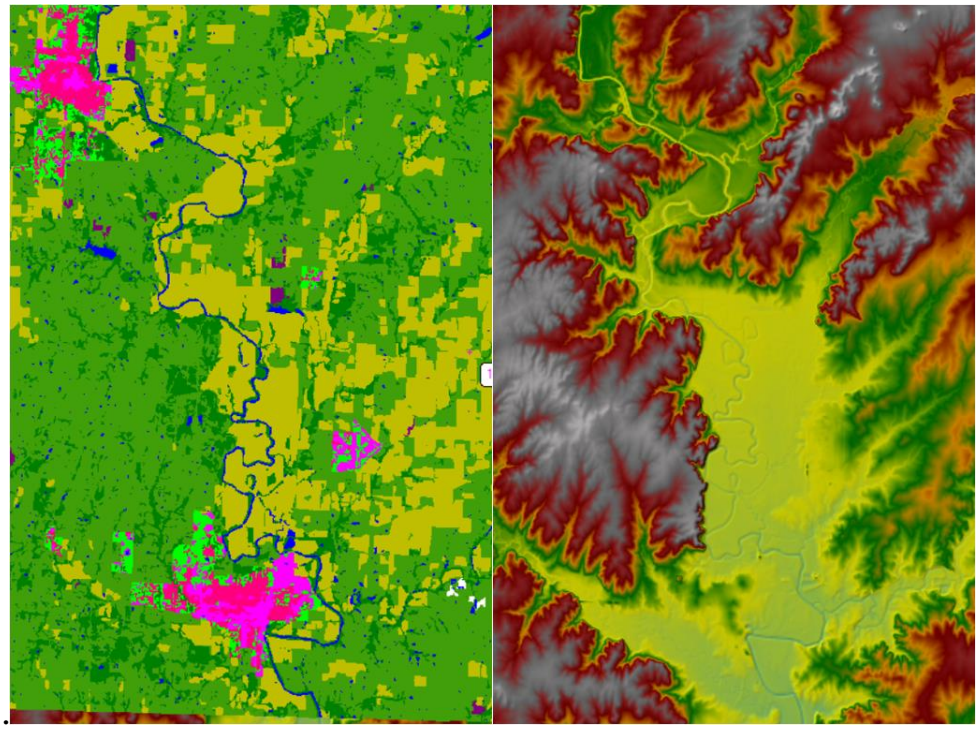

Figure 2-7: Study area. LULC and terrain data inputs to HEC-RAS model.

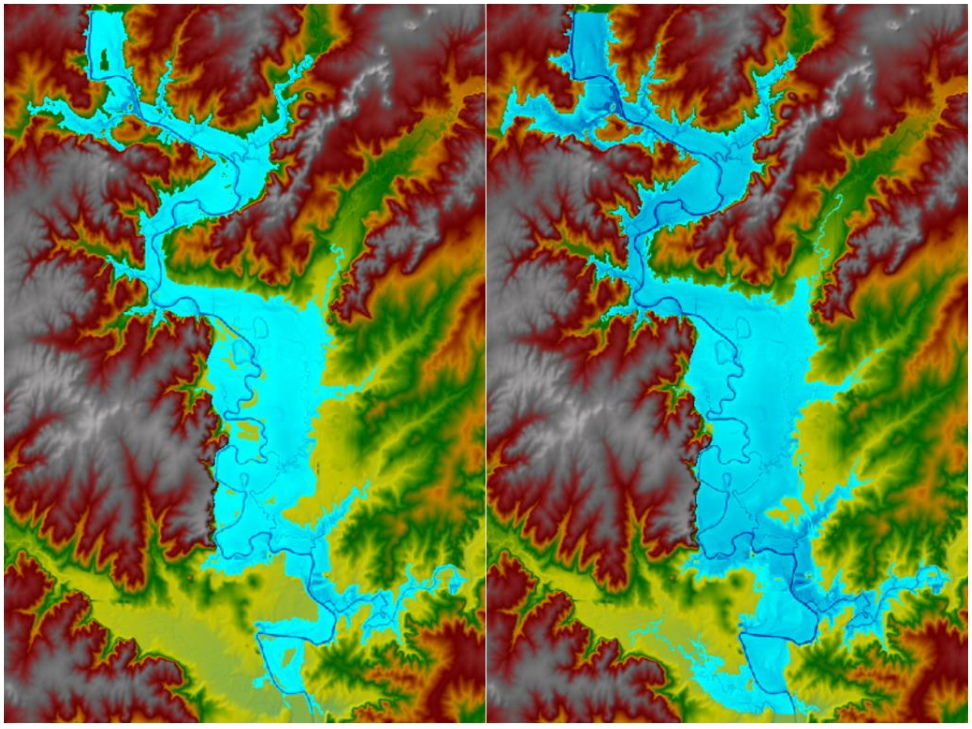

Figure 2-8: Flood depth map and flood extent of HRM 1K cms (left) and 4.8K cms (right) scenarios.

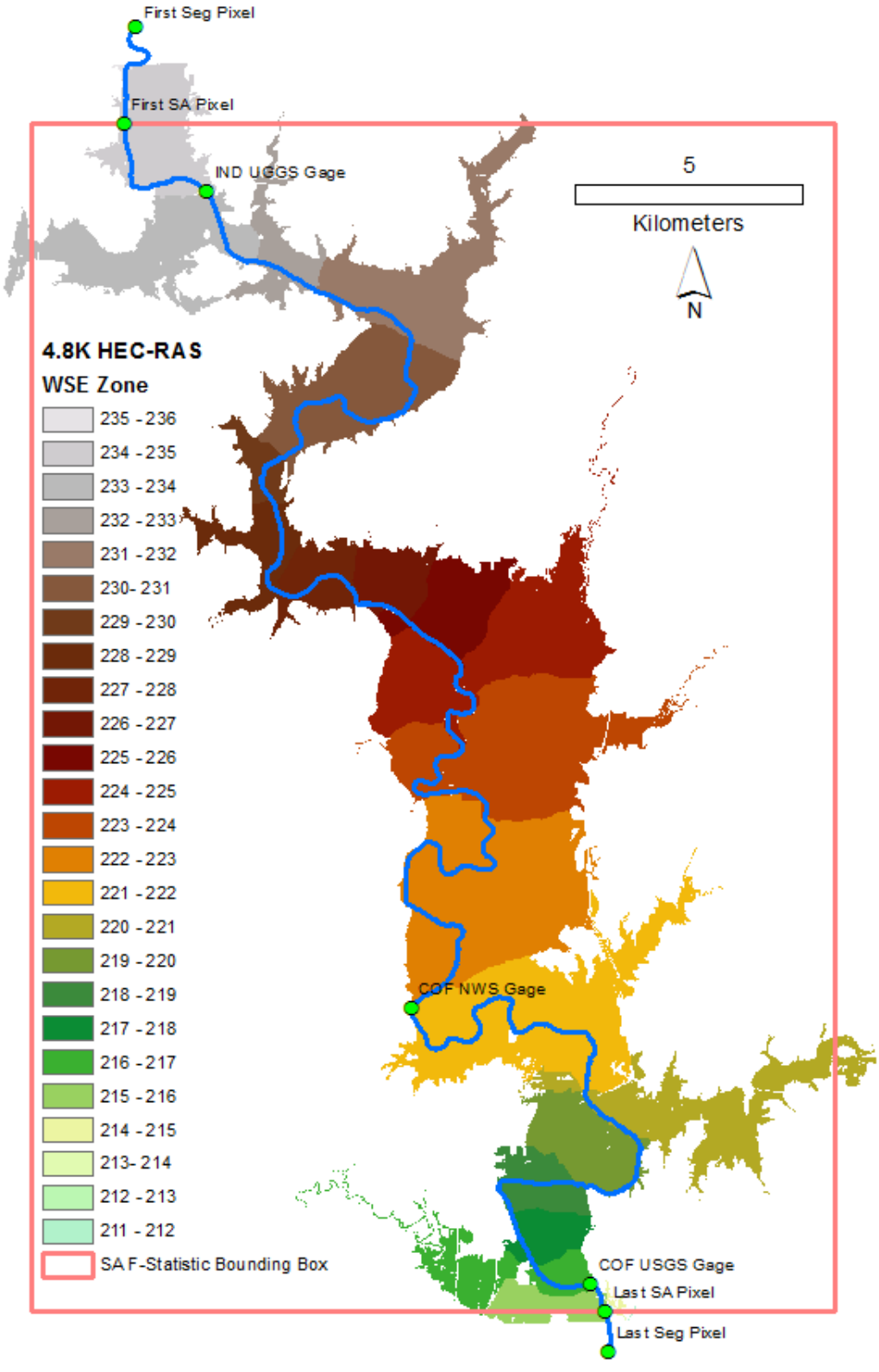

Figure 2-9: Map of HEC-RAS water surface elevations for 4.8K flood for the study area.

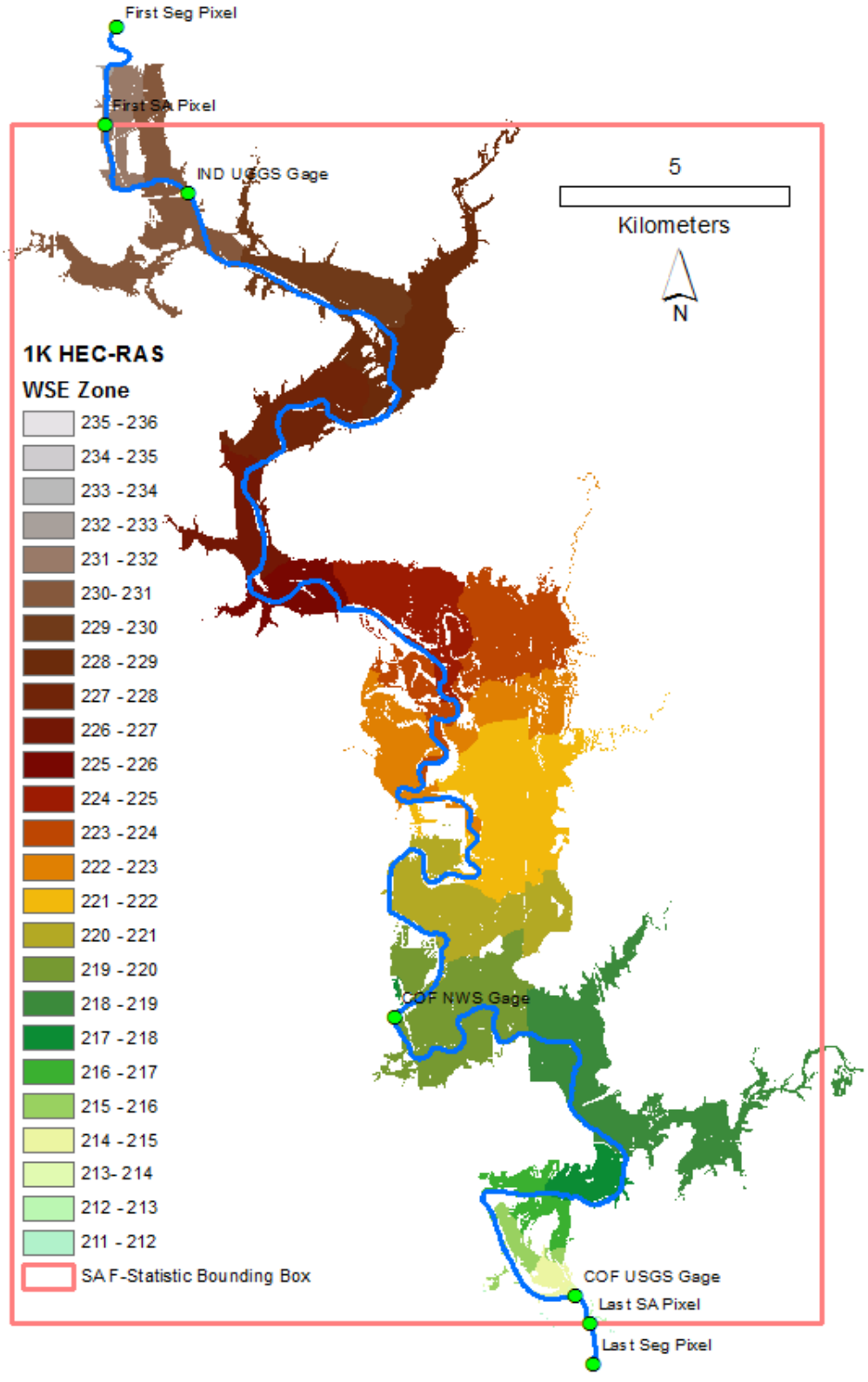

Figure 2- 10: Map of HEC-RAS waster surface elevations for 1K flood for the study area.

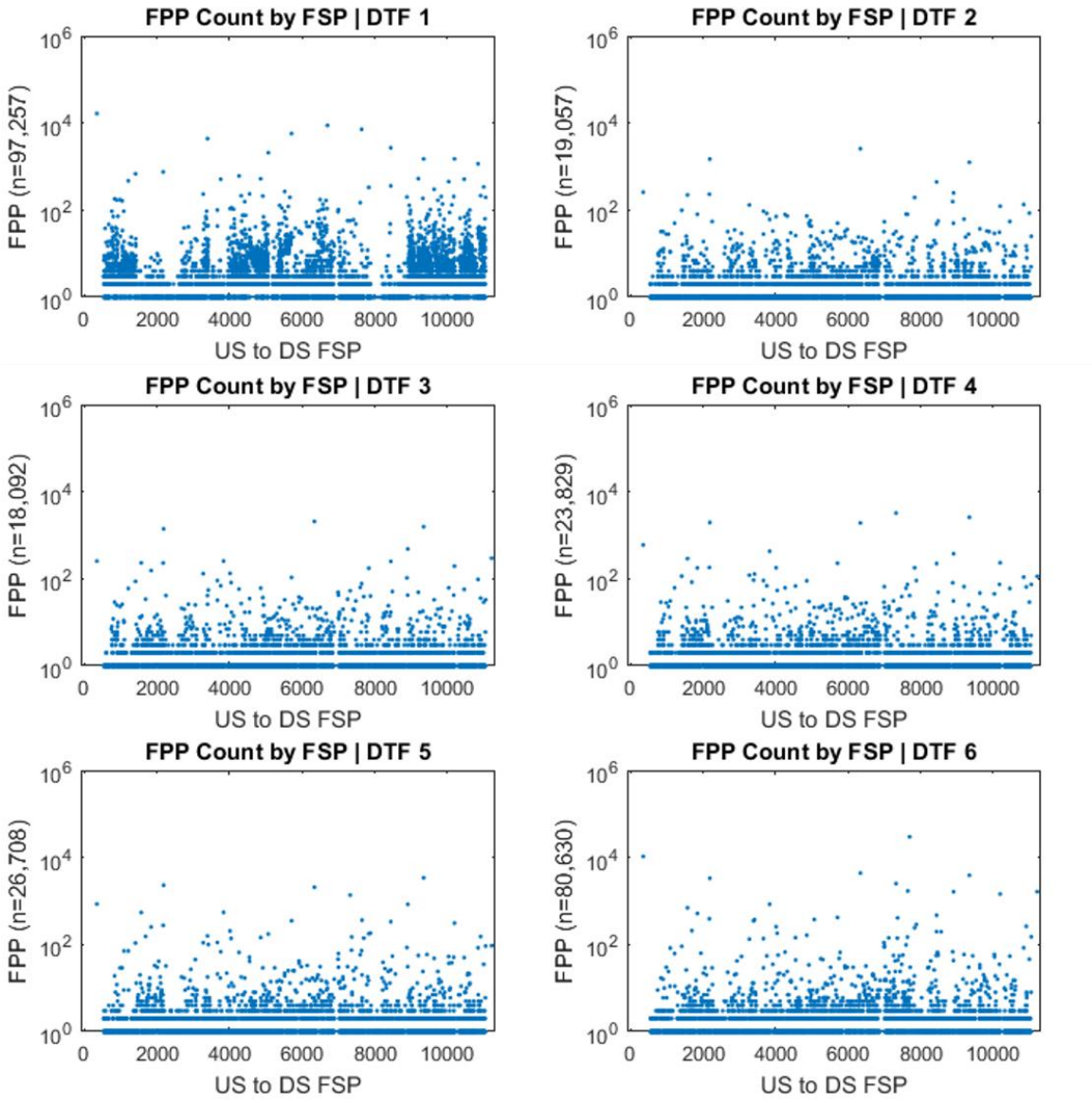

Figure 2-11: FPP links to FSP plots series 1 [Note that the y-axis is on a log scale] This series of three figures, with 18 graphics overall, illustrates the relationship of the FSP to the FPP and potential influence of the DTF profile at various stages. This series of graphics is closely related to Figures 2-15,16, a review of which is helpful when considering the interpretation that follows. The density of points in conjunction with the initial spikes seen in Figures 2-15,16 indicate the initial 'filling' of the stream surface by the FLDPLN model. The 2m to 6m DTF graphics represent the filling of the stream channel. Note that an even density of FSPs is represented across the length of the streamline, and at relatively low FPP levels compared to higher DTF plot shown in Figures 2-12 and 2-13.

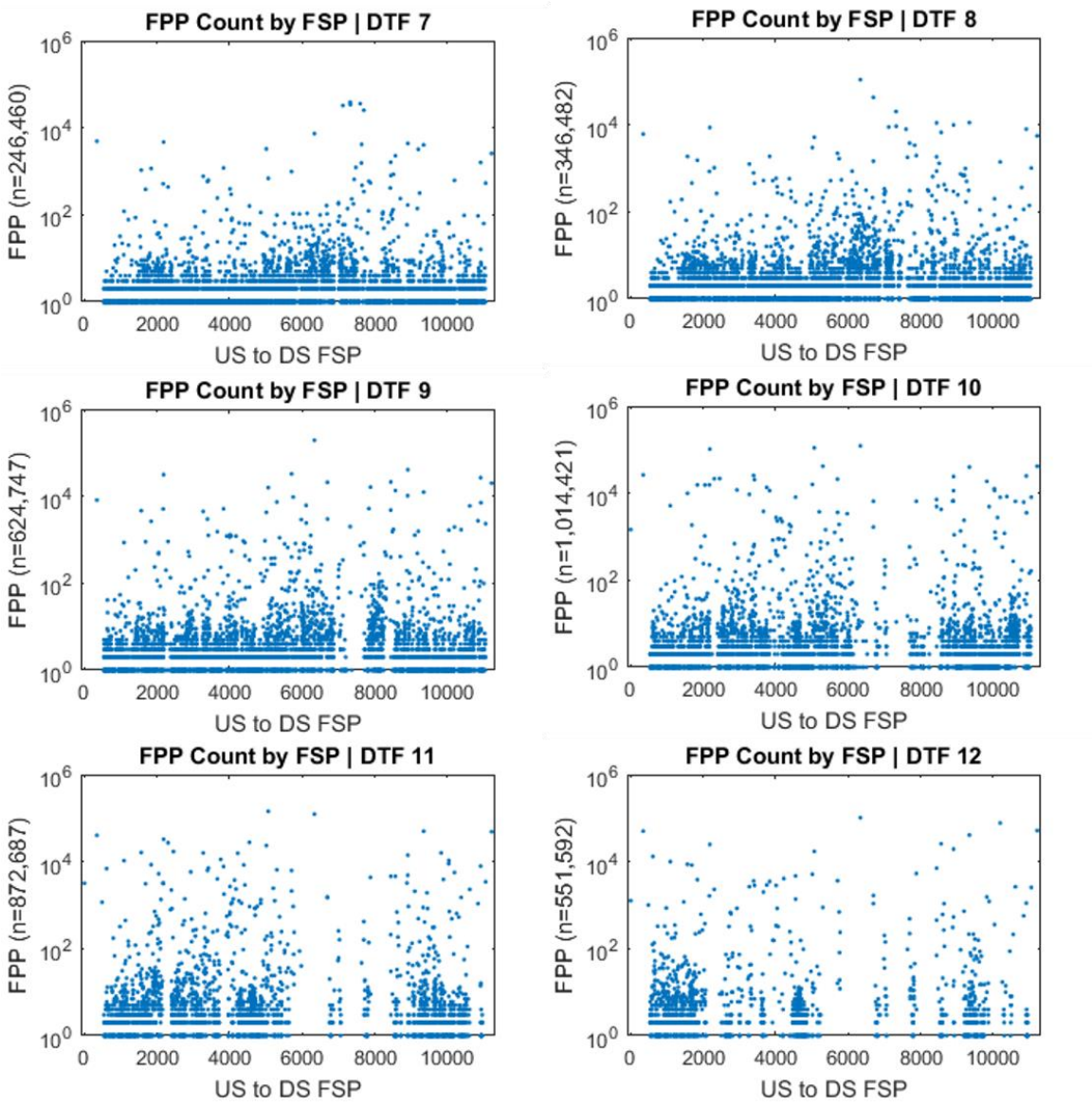

Figure 2-12: FPP links to FSP plots series 2 [Note that the y-axis is on a log scale] During the phase represented in the graphics above, the FSP density begins to thin out as key FSPs begin to dominate the influence over new FPPs, which is also seen in the increasing magnitudes on the y-axis. Refer to Figures 2-14 and 2-15 for supporting analysis.

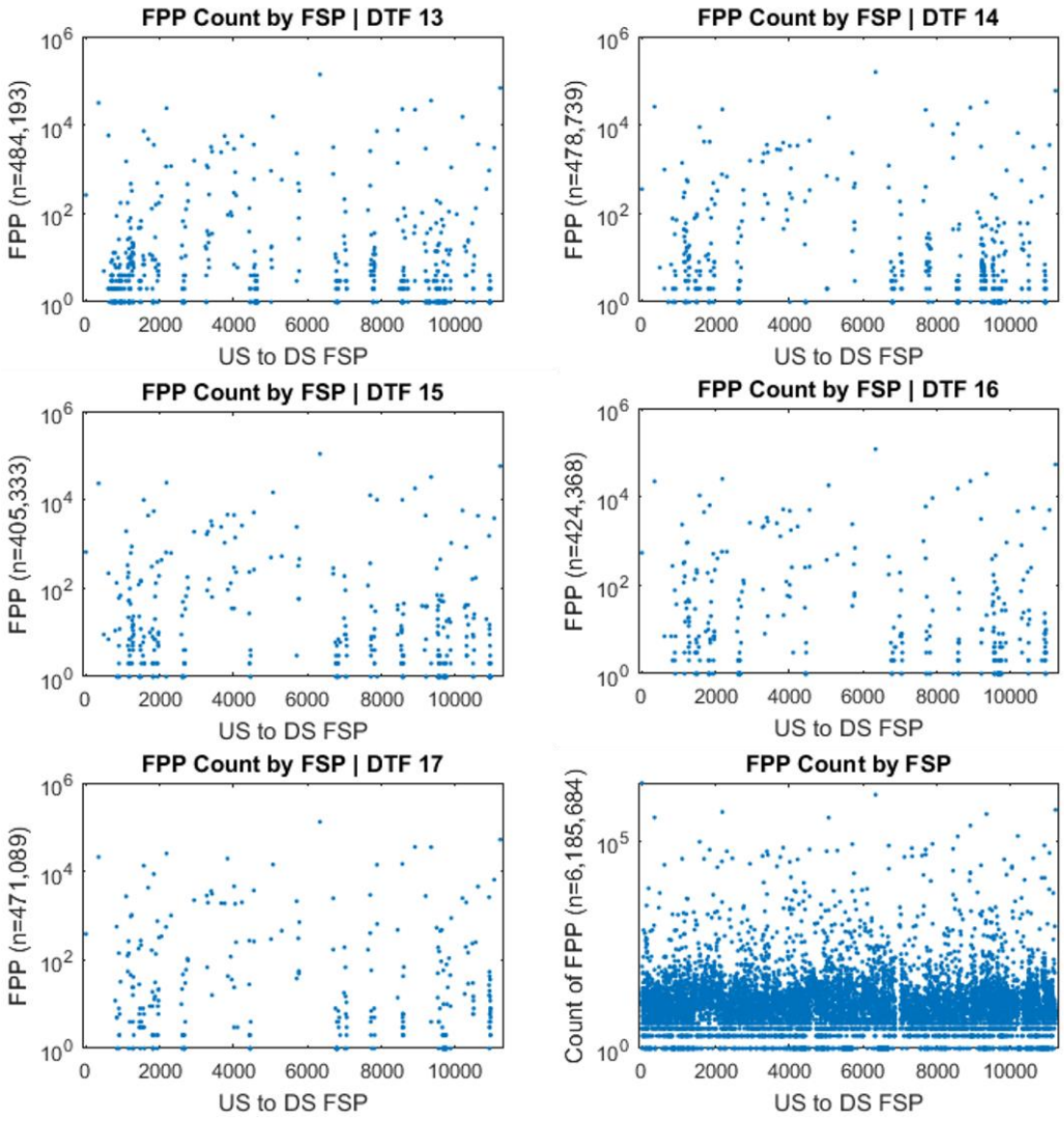

Figure 2-13: FPP links to FSP plots series 3 [Note that the y-axis is on a log scale] In this phase, clearly dominant FSPs emerge and continue to compete along the inundation front for 'control.' By the last few meters, very few FSPs have any connection to the inundation front and among those, several dominate. Figure 2-14 shows that the number of unique FSPs dwindles to fewer than 200, even while the incremental level of new FPP recruitment remains stable.

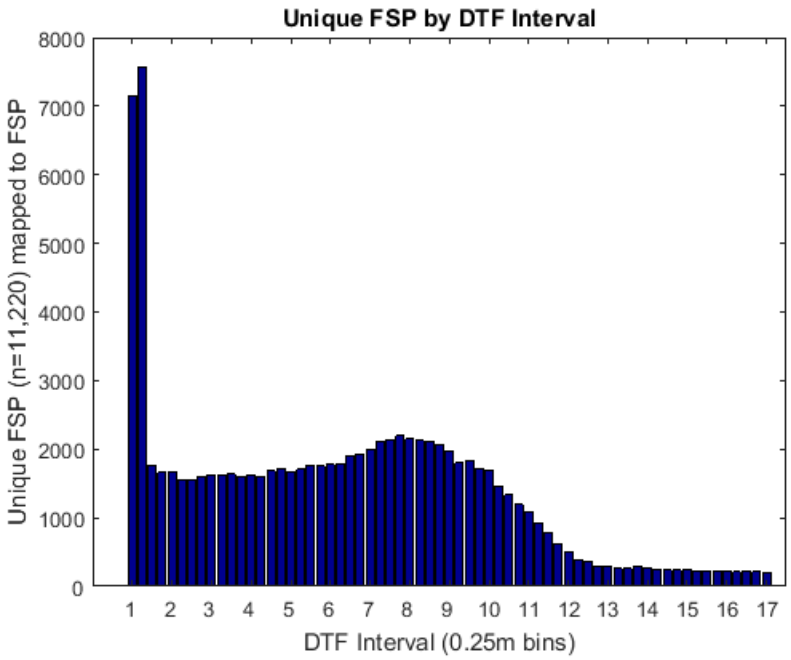

Figure 2-14: Unique FSP by DTF interval plot. This bar chart shows the number of unique FPP assigned to FSPs across the entire range of DTF values. With 11,220 FSPs, the initial spike reflects the initialization of the algorithm and the FPPs in the immediate vicinity of the FSPs within the river channel. Figure 2-12 confirms the relative magnitude of the initialization. After the initial recruitment of the river channel pixels, a majority of FSPs do not function as FSPs for any FPPs at higher DTF values. The number of unique FSPs remains stable, at just under 2000, through about 6m. This behavior also corresponds nicely with Figure 2-16, which shows relatively few new FPPs being recruited. This phase corresponds to the filling of the channel through the bankfull stage. After 6m the number of unique FSPs increases slightly and peaks at about 8m, after which there is a steady decline through 12m. In the final phase the number of unique FSPs falls below 300 (at 13m) and steadily declines to a low of 203 in the last 0.25m. [It is important to note that there is no distinction in the graph between a FSP that is represented one time or one that appears 100,000 times. Figures 2-11:13, however, illustrate the magnitude of each FSP overall and at 1m DTF increments.]

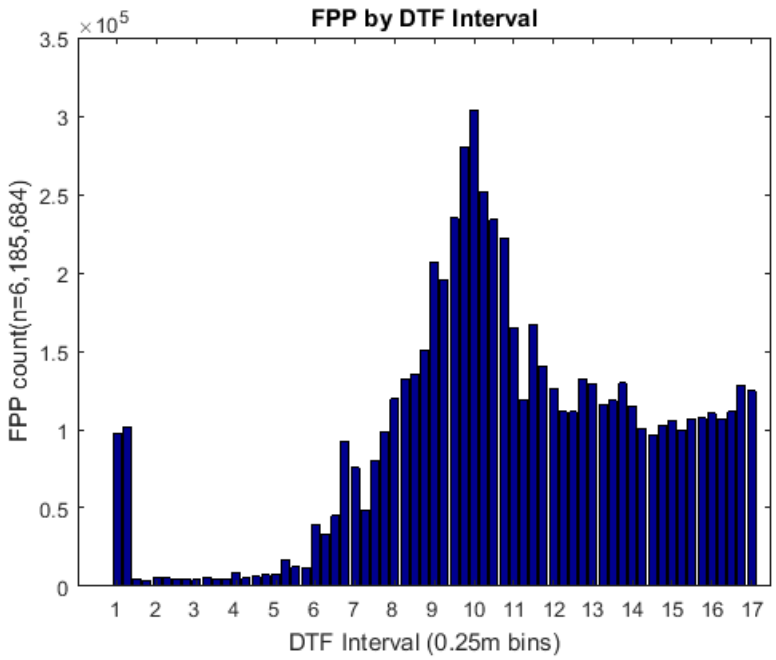

Figure 2-15: FPP by DTF interval plot. When considering all FPP identified by the FLDPLN model for this study area, this plot shows the number of pixels recruited at 0.25m DTF intervals. The initial spike at 1.25m and below is caused by the addition of stream pixels surrounding the FSP pixels. Once this occurs, few new pixels are recruited until the bankfull condition is exceeded at 6m (this value will vary by stream morphology, which is dependent on a range of factors). Once paths are established that give access to the floodplain, there is a sharp rise the incremental recruitment of FPPs that continues through a peak at around 10m. The floodplain valley morphology dictates that the rapid lateral spreading will diminish and give way to a more even spreading that stabilizes at about 12m. Examination of Figure 2-15 also gives a supporting view of these data.

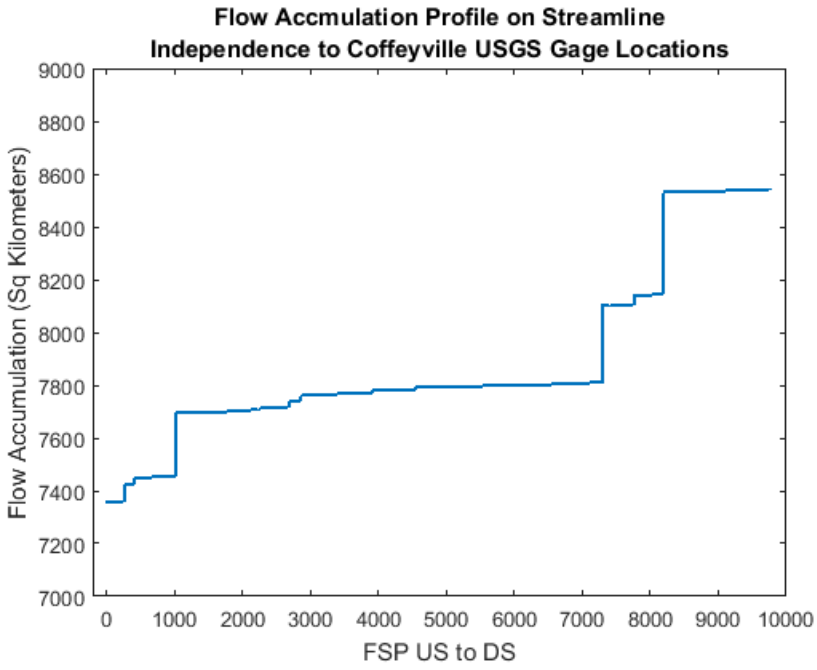

Figure 2-16 Flow accumulation profile from synthetic stream network. Although not modeled in this study, the influence of additional tributary discharge that can occur at locations of significant increases in flow accumulation could create additional WSE profile complexity that is not considered in this analysis.

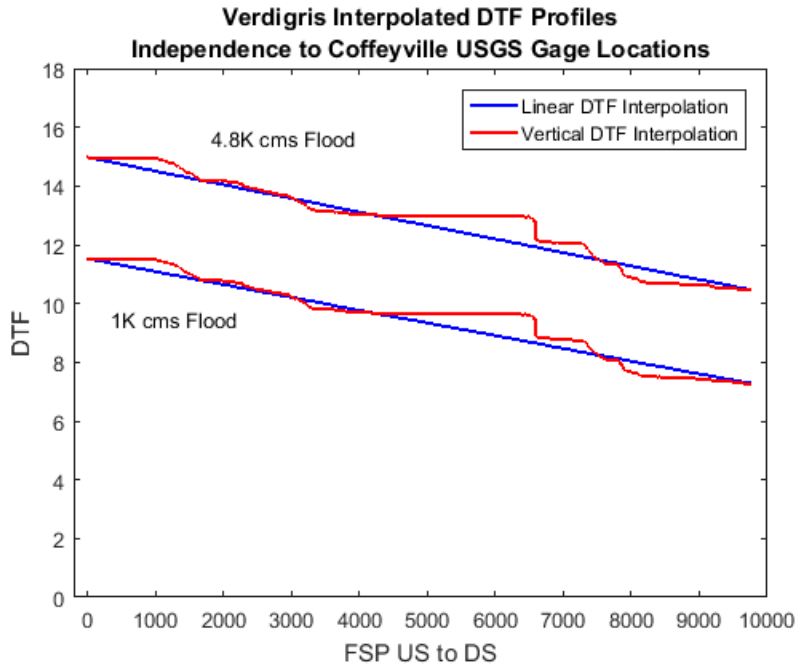

Figure 2-17: Horizontal and vertical DTF interpolation between Independence and Coffeyville USGS gage locations. The endpoint DTF values for the 4.8K cms flood were 14.97 and 10.47m, respectively. The endpoint DTF values for the 1K cms flood were 11.53 and 7.32m, respectively.

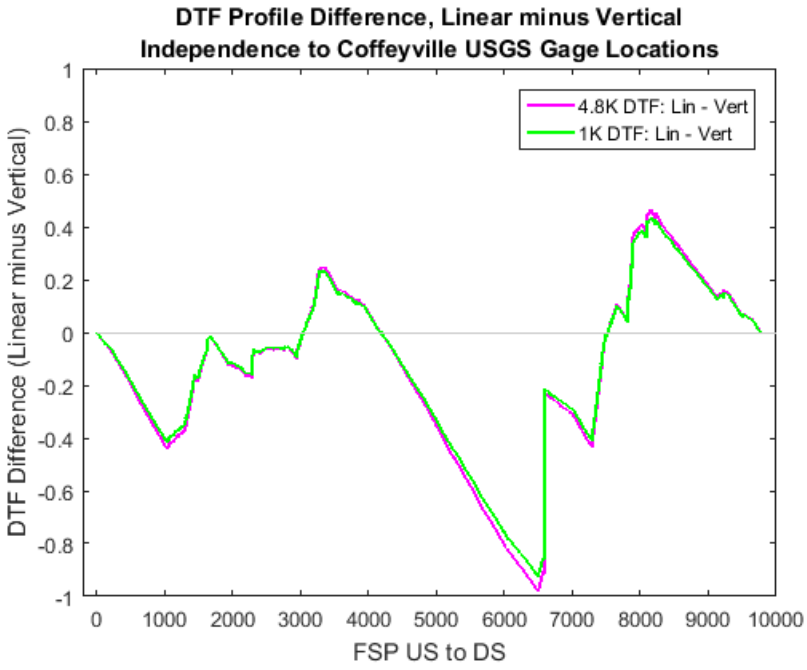

Figure 2-18 Difference between horizontal and vertical DTF interpolation profiles for both 4.8K and 1K cms flood simulations. Upstream (US) and downstream(DS) endpoint DTF values were derived from HEC-RAS 2D modeled floods.

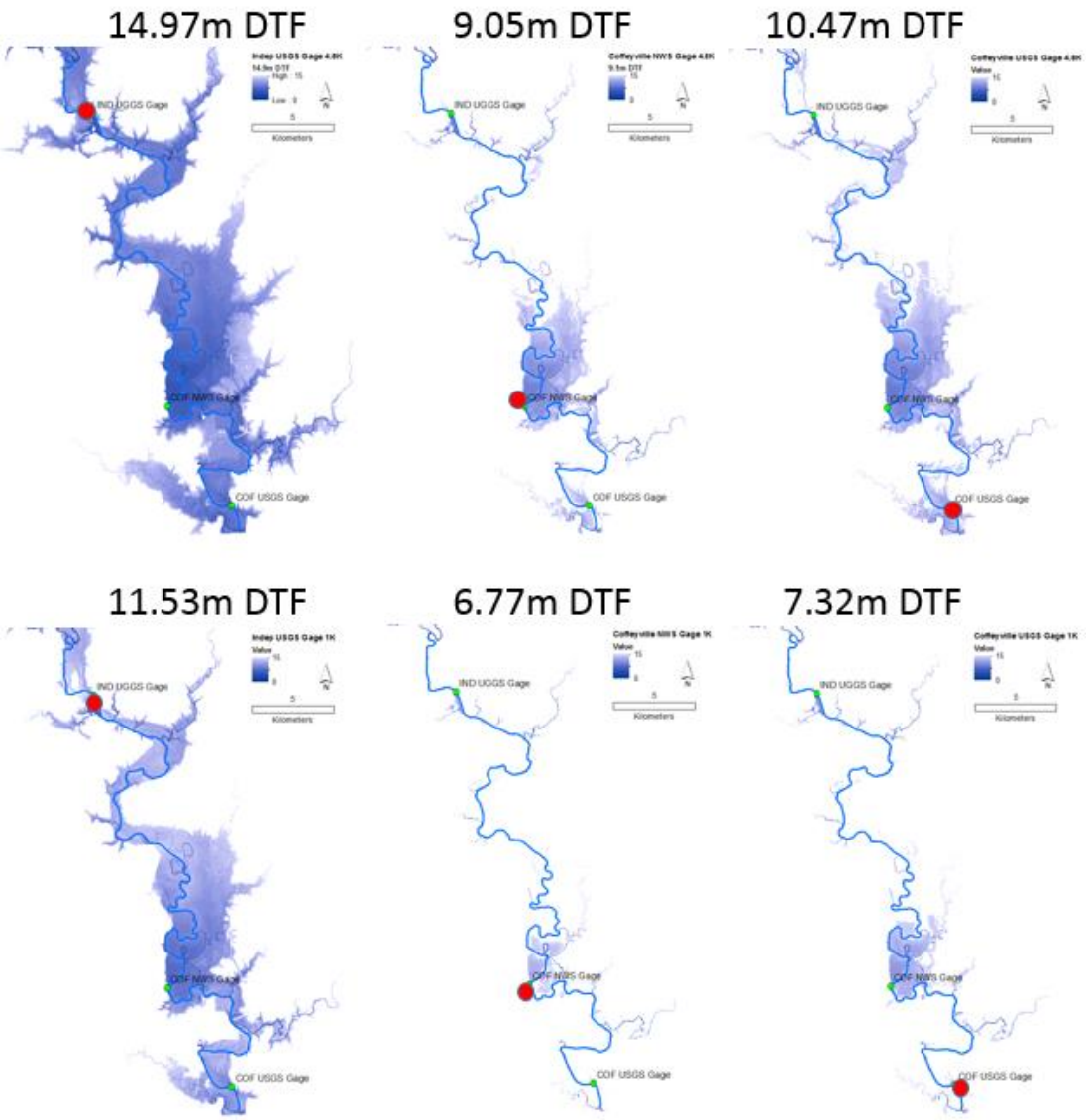

Figure 2-19: Range of single DTF input FLDPLN model inundation maps for the Verdigris River between Independence, KS and Coffeyville, KS. The top row shows DTF values of 14.97, 9.05, ,and 10.47m, which correspond to WSE values produced by a 4.8K cms HEC-RAS 2D model, and correspond to the USGS Independence, NWS Coffeyville, and USGS Coffeyville gage locations, respectively. The bottom row shows DTF values of 11.52, 6.77, and 7.32m, which correspond to WSE values produced by a 1K cms HEC-RAS 2D model, and correspond to the USGS Independence, NWS Coffeyville, and USGS Coffeyville gage locations, respectively. These inundation extents represent what output would be produced if only *one* DTF value were used from the entire stream segment, based on the WSE at only *on*e gage in each scenario.

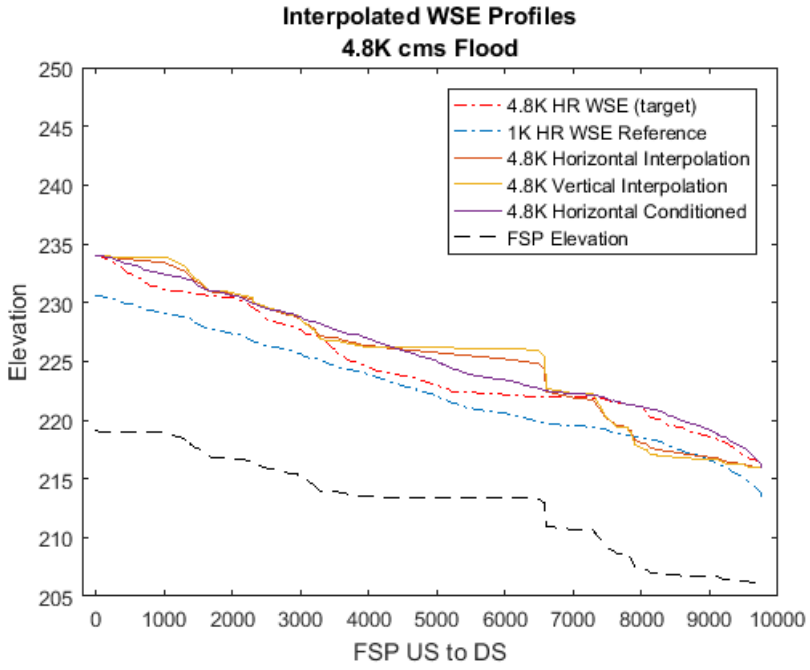

Figure 2-20: Comparison of interpolated 4.8K WSE profiles using the horizontal, vertical, and conditioned horizontal techniques. The stream surface, as represented in the FIL DEM, is shown with the black dashed FSP elation profile. The modeled HEC-RAS 4.8K cms profile (target) is shown in red dashed profile. The 1K cms conditioning reference is shown in the blue dashed line.

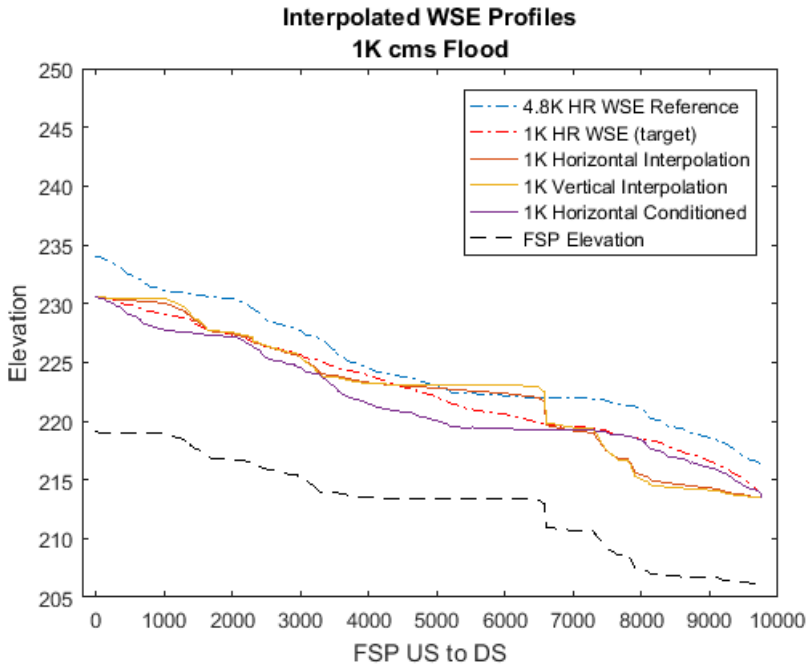

Figure 2-21: Comparison of interpolated 1K WSE profiles using the horizontal, vertical, and conditioned horizontal techniques. The stream surface, as represented in the FIL DEM, is shown with the black dashed FSP elation profile. The modeled HEC-RAS 1K cms profile

(target) is shown in red dashed profile. The 4.8K cms conditioning reference is shown in the blue dashed line.

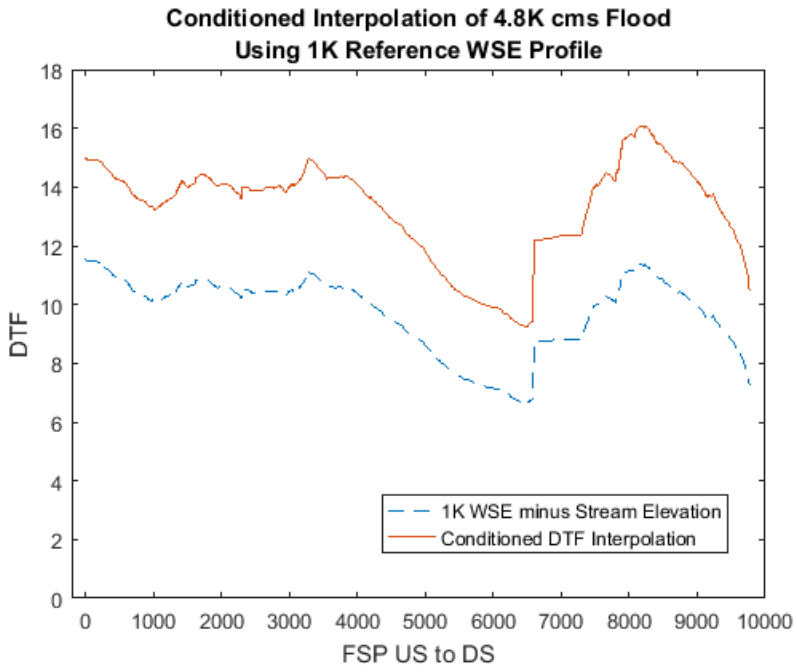

Figure 2-22: Conditioned DTF interpolation for the 4.8K cms flood. The 1K cms flood DTF profile was used to 'peg' each DTF to a known value, then extrapolate upward to derive the 4.8K profile.

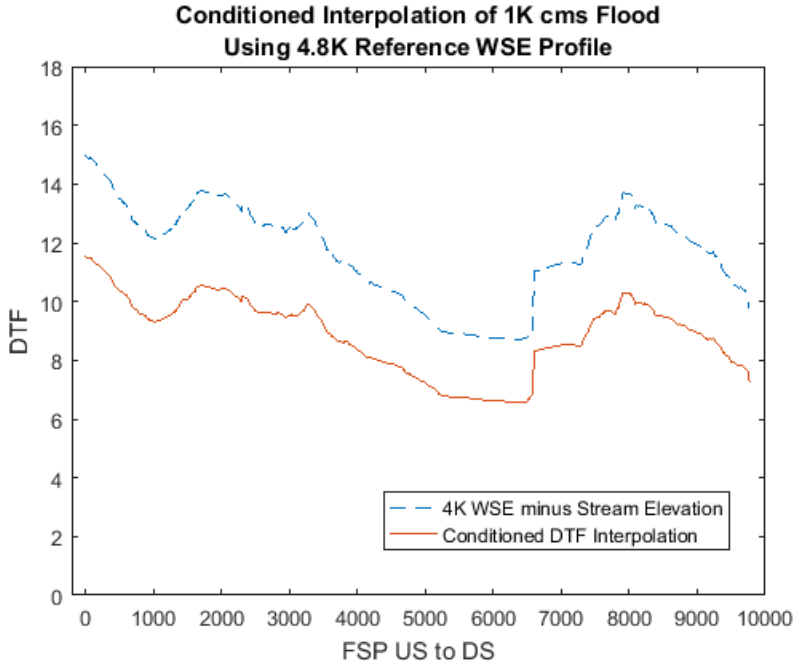

Figure 2- 23: Conditioned DTF interpolation for the 1K cms flood. The 4.8K cms flood DTF profile was used to 'peg' each DTF to a known value, then interpolate downward to derive the 1K profile.

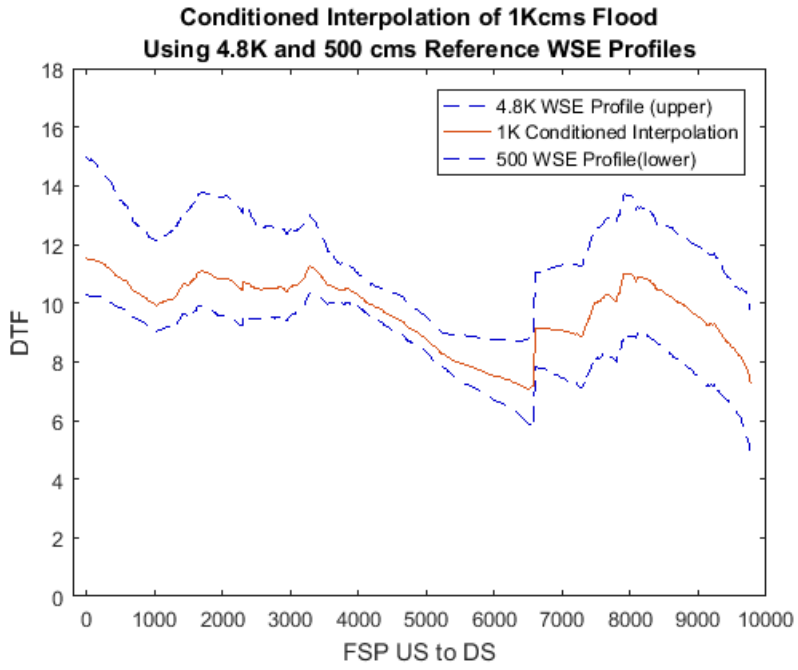

Figure 2-24: Bound-conditioned DTF interpolation. This more advanced interpolation utilizes the modeled 4.8K cms flood WSE profile and the 500 cms profile, which is an approximate bankfull discharge for the Verdigris within the study area. The 1K DTF profile is generated by interpolating between these modeled profiles. This method achieved the highest F-statistic for all interpolation methods, with a value of 76.6.

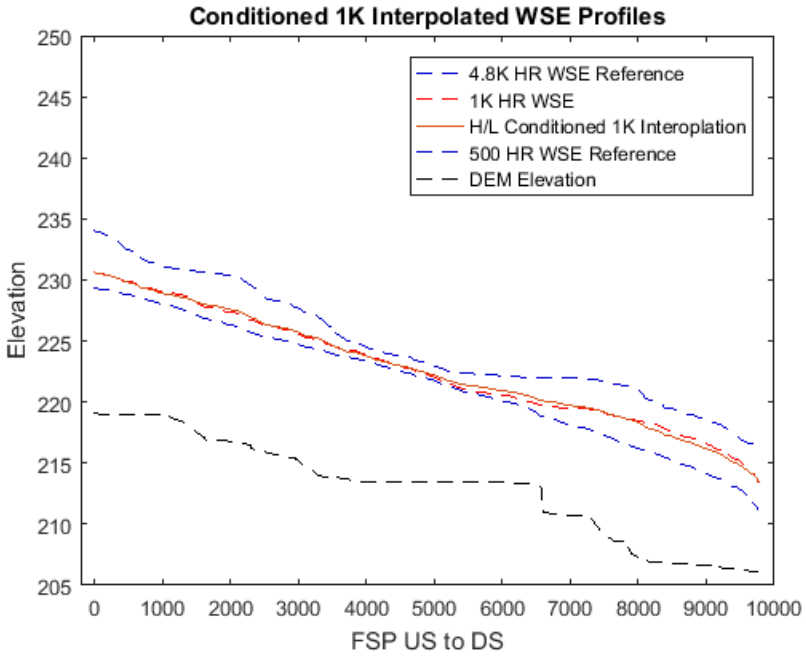

Figure 2-25: Bound-conditioned WSE. Conditioned interpolation that uses a high flow and a low flow (H/L), in this case the 4.8K and 500 cms HEC-RAS modeled flow, to interpolate and intermediate

flow, the 1K cms flow. In practice, once the high and low profiles are known, intermediate DTF profiles can be used to quickly generate custom flood extent estimate layers. For the 1K cms flood extent estimation, this technique yielded the highest F-statistic with a value of 76.6.

References Cited

Bates, P. D., & De Roo, A. P. J. (2000). A simple raster-based model for flood inundation simulation. *Journal of Hydrology, 236*(1-2), 54-77.

Bhatt, C. M., Rao, G. S., Diwakar, P. G., & Dadhwal, V. K. (2016). Development of flood inundation extent libraries over a range of potential flood levels: a practical framework for quick flood response. *Geomatics, Natural Hazards and Risk*, 1-18. doi:10.1080/19475705.2016.1220025

Cook, A., & Merwade, V. (2009a). Effect of topographic data, geometric configuration and modeling approach on flood inundation mapping. *Journal of Hydrology, 377*(1–2), 131-142. doi:http://dx.doi.org/10.1016/j.jhydrol.2009.08.015

Cook, A., & Merwade, V. (2009b). Effect of topographic data, geometric configuration and modeling approach on flood inundation mapping. *Journal of Hydrology, 377*(1/2), 131-142.

Dobbs, K. E. (2010). *Evaluation of the USGS national elevation dataset and the Kansas Biological Survey's FLDPLN ("floodplain") model for inundation extent estimation.* (1477630 M.A.), University of Kansas, Ann Arbor. Dissertations & Theses @ University of Kansas; ProQuest Dissertations & Theses Global database.

Horritt, M. S., & Bates, P. D. (2001). Effects of spatial resolution on a raster based model of flood flow. *Journal of Hydrology, 253*(1-4), 239-249.

Kastens, J. H. (2008). *Some New Devolopments On Two Separate Topoics: Statistical Cross Validation and Floodplain Mapping.* (Mathematics Dissertation), The University of Kansas, Lawrence.

Knebl, M. R., Yang, Z. L., Hutchison, K., & Maidment, D. R. (2005). Regional scale flood modeling using NEXRAD rainfall, GIS, and HEC-HMS/RAS: a case study for the San Antonio River Basin Summer 2002 storm event. *Journal of Environmental Management, 75*(4), 325-336. doi:http://dx.doi.org/10.1016/j.jenvman.2004.11.024

Leon, A. S., & Goodell, C. (2016). Controlling HEC-RAS using MATLAB. *Environmental Modelling & Software, 84*, 339-348. doi:http://dx.doi.org/10.1016/j.envsoft.2016.06.026

Mason, D. C., J-p. Schumann, G., & Bates, P. D. (2010). Data Utilization in Flood Inundation Modelling *Flood Risk Science and Management* (pp. 209-233): Wiley-Blackwell.

Mason, D. C., Schumann, G. J. P., Neal, J. C., Garcia-Pintado, J., & Bates, P. D. (2012). Automatic near real-time selection of flood water levels from high resolution Synthetic Aperture Radar images for assimilation into hydraulic models: A case study. *Remote Sensing of Environment, 124*, 705-716. doi:http://dx.doi.org/10.1016/j.rse.2012.06.017

Moya Quiroga, V., Kure, S., Udo, K., & Mano, A. (2016). Application of 2D numerical simulation for the analysis of the February 2014 Bolivian Amazonia flood: Application of the new HEC-RAS version 5. *RIBAGUA - Revista Iberoamericana del Agua, 3*(1), 25-33. doi:http://dx.doi.org/10.1016/j.riba.2015.12.001

Peterson, D. L., Whistler, J. L., Lomas, J. M., Dobbs, K. E., Jakubauskas, M. E., Egbert, S. E., & Martinko, E. A. (2008). *2005 Kansas Land Cover Patterns Phase I: Final Report*. Retrieved from

Sarhadi, A., Soltani, S., & Modarres, R. (2012). Probabilistic flood inundation mapping of ungauged rivers: Linking GIS techniques and frequency analysis. *Journal of Hydrology, 458–459*, 68-86. doi:http://dx.doi.org/10.1016/j.jhydrol.2012.06.039

Tayefi, V., Lane, S. N., Hardy, R. J., & Yu, D. (2007). A comparison of one- and two-dimensional approaches to modelling flood inundation over complex upland floodplains. *Hydrological Processes, 21*(23), 3190-3202.

Xue, X., Hong, Y., Limaye, A. S., Gourley, J. J., Huffman, G. J., Khan, S. I., . . . Chen, S. (2013). Statistical and hydrological evaluation of TRMM-based Multi-satellite Precipitation Analysis over the

Wangchu Basin of Bhutan: Are the latest satellite precipitation products 3B42V7 ready for use in ungauged basins? *Journal of Hydrology, 499*, 91-99. doi:http://dx.doi.org/10.1016/j.jhydrol.2013.06.042

Yan, K., Neal, J. C., Solomatine, D. P., & Di Baldassarre, G. (2015). Chapter 4 - Global and Low-Cost Topographic Data to Support Flood Studies *Hydro-Meteorological Hazards, Risks and Disasters* (pp. 105-123). Boston: Elsevier.

CHAPTER 3

RAPID FLOOD MAPPING APPLICATION OF THE FLDPLN MODEL: SENSITIVITY ANALYSIS USING SIMULATED GEOSPATIAL ANALYST INPUT

Abstract

Emergency managers need reliable information in near real-time to effectively respond to flood disasters. Hydrodynamic modeling of floods has largely focused on understanding and mapping risk, not on disaster response. Modeled scenarios, such as the FEMA 100-year flood zone, are of little value to emergency managers during a disaster because the crisis at hand is unlikely to match the magnitude of the modeled scenario. Satellite remote sensing has been used successfully to provide valuable information on the extent of flooding during the disaster response phase, yet new tools and techniques are needed to allow geospatial analysts to extract information about the flood extent from the imagery quickly and effectively. This research examines a new method to combine imagery and modeled flood extents that has the potential to improve the accuracy of flood extent estimates and to reduce the time required to derive them. The FLDPLN model, developed at the University of Kansas, is used in conjunction with simulated flood extent boundaries to explore methods that can be used with remotely sensed data to rapidly derive flood extent estimates for flood response efforts. The results show that flood inundation extents can be estimated with a limited number of simulated flood boundary points, indicating the potential that similar output could be derived rapidly by analysts from imagery acquired during flood events.

Terms and Abbreviations

[AMSR-E and AMSR-2] Advanced Microwave Scanning Radiometer: Japanese satellites that collect passive microwave radiation.

[DEM] Digital Elevation Model

[DTF] Depth to flood: the output of the FLDPLN model developed by Kastens (2008) relating the minimum flood depth required to inundate a non-stream pixel from a reference stream pixel. In some circumstances the DTF can be used as a proxy for stage.

[FAC]Flow Accumulation layer: raster data derivative of DEM data with catchment area calculated for every cell.

[**FLDPLN**] FLDPLN model used to derive a segmented library of inundation extents (SLIE).

[FPP] Floodplain pixel: pixels flooded from FSPs at a given flood depth (DTF).

[FSP] Flood source pixel: stream pixels derived from a DEM-derived synthetic stream network, utilized by the FLDPN model to determine relative height above the stream.

[GFDS] Global Flood Detection System: global, daily flood layer derived from passive microwave satellite remote sensing data.

[LISFLOOD-FP] "LISFLOOD-FP is a two-dimensional hydrodynamic model specifically designed to simulate floodplain inundation in a computationally efficient manner over complex topography."

[MODIS] Moderate Resolution Imaging Spectrometer: global moderate resolution multispectral instruments aboard the Terra and Aqua satellite platforms.

[NASA] National Aeronautics and Space Administration

[NED] National Elevation Dataset: US DEM dataset maintained by the USGS

[NIR] Near infrared: spectral band located between red and middle infrared wavelengths that is readily absorbed by water and is useful for identifying flooded are in remotely sensed imagery.

[SLIE] Segmented library of inundation extents: database of outputs from running of the University of Kansas FLDPLN model.

[UAS] Unmanned Aerial System: also known as unmanned aerial vehicles (UAV) or "drones."

[USGS] United States Geological Survey

Units and measures

Stream discharge (flow): given in cubic meters per second (cms) or cubic feet per second (cfs), discharge is a measure of the volume of water flowing through a vertical plane oriented perpendicular to the direction of stream flow. Often referred to as a measured quantity, it is actually a value estimated from a set of measured velocities along a stream channel cross

section. When calculated for a range of river levels and combined with an adequate historical baseline of stage data (see below), discharge can be plotted on a logarithmic scale to develop a flood frequency regression equation to estimate the return period of a given magnitude flood event.

River stage: a measured quantity that relates the water surface elevation at a monitored point on a stream (e.g. at a stream gage) to an arbitrary reference datum with a known elevation. The reference datum is usually chosen to be below the streambed to avoid negative stage values. With datum and stage information, the water surface elevation at the gage location can be determined.

Introduction

The fundamental justifications for the research outlined here can be summarized as: 1) the technologies that support the development of high quality elevation data are rapidly improving, which will lead to wide area coverage with unprecedented vertical accuracy; 2) the quantity of high resolution satellite remote sensing data is also rapidly increasing; and 3) when combined, these two data streams will support the methods that are outlined in this research with the potential to significantly improve the quality of flood extent mapping for disasters and reduce the time required to produce actionable information for disaster response. The overarching framework for achieving this advancement is outlined in Figure 3-1, which describes graphically the inputs, processing steps, and application implementation of the integration of satellite data and other inputs with inundation libraries developed with the FLDPLN model(Peterson et al., 2008). Previous research has shown that this approach can be utilized with limited input data over local scales to map floods with gage data as inputs (Figures 3-2 and 3-3) (Dobbs, 2010). Current trends in elevation data production and satellite imagery collection and distribution make this line of research increasingly relevant.

Current trends for elevation data

Rapid advances in sensor technology, data storage, computational capacity, and software development make this an exciting time for the advancement to high-resolution digital elevation model (DEM) production and

availability. Because the application areas are so diverse, only wide-area topographic data production will be reviewed.

Lidar systems are the most commonly used technology for high-resolution DEM generation today, and the cost per unit area has steadily declined. The primary type of lidar technology that is currently used to produce high-resolution DEMs is some version of a linear-mode scanning pulsed-laser system (Mallet & Bretar, 2009). While the pulsed-laser systems account for most of the commercial hardware used for high-resolution DEM production today, advances in Geiger-mode systems are also important for future directions of wide-area topographic mapping (Abdullah, 2016).

Lidar systems are classified as active systems because they emit pulses of coherent laser light, usually in the NIR or green portion of the electromagnetic spectrum. As such, they can be flown at any time of day or night if weather conditions permit. For topographic mapping, generally campaigns are scheduled to occur during leaf-off conditions when there is minimal or no snow cover. Dense foliage impedes the emitted laser pulse signal from reaching the ground surface, which, for bare-earth DEM production, is the desired surface from which to collect a detectable return. Snow cover also causes the ground surface to be misrepresented. For certain regions, this can leave a narrow window within which to schedule collection campaigns, or limit altogether the utility of lidar data potentially collected from perpetually vegetated surfaces.

For most linear pulse-laser systems, the full-waveform return is not recorded. Depending on the requirement specifications, the return signal is

discretized at its major peaks, yielding a point-cloud of returns, typically with a maximum of between four and six returns per pulse for most collection. The first return typically represents a point near the top of canopy, and the last return represents the ground or other impenetrable surface (e.g. rooftops), or possibly the deepest foliage penetration for which the point thresholding algorithm detects a signal peak. For low vegetation or bare ground, there may be only one return recorded.

HARRIS Corp has recently made available a commercial Geiger-mode lidar instrument (Abdullah, 2016). However, it is not yet widely available, and to date has been used primarily for government and US Department of Defense applications. Geiger-mode systems use a fundamentally different approach than linear-mode systems. They use an avalanche photo diode array with a photon counting device. So, instead of a single pulse and single measurement of the linear-mode sensor, the Geiger-mode sensing has as many sensors as the array, 4096 in the case of the HARRIS Intelliearth system. Overall this means that the Geiger-mode system can fly at a much higher altitude, and at a greater speed, to collect the same point density. This translates into decreased cost and higher production capacity. In order to achieve this, however, new techniques for data processing and storage will have to be developed to handle the much higher volumes and rates of data that are produced.

Synthetic aperture radar (SAR) is an active system that emits a radar signal in the microwave part of the electromagnetic spectrum and records the timing and orientation of the reflected signal. Simplistically described, a

combination of interferometric geometry, phase difference, and interferometric phase from two SAR signals yields a 3D location of the return signal (Schumann et al., 2007). Thus, these data also can be used to map terrain. Like imagery-based photogrammetry, dense vegetation can be problematic. There are techniques, however, that use landcover information and per-pixel height uncertainty to conduct vegetation removal. Automated and manual techniques are used to remove manmade structures. One main advantage of SAR systems is that the radar signal penetrates clouds, making it an all-weather system (Di Baldassarre, Schumann, & Bates, 2009).

The primary airborne interferometric synthetic aperture radar (IFSAR) data provider in the US is InterMAP (Coveney, 2013). InterMAP offers airborne system data at 5m resolution with three different product lines: a digital surface model (DSM), which represents buildings and vegetation in the modeled surface, a digital terrain model (DTM) where vegetation and buildings have been "digitally removed," and an ortho-ready image (ORI) that can be used for orthorectification of optical images (InterMap, 2017). The stated vertical accuracy of the DSM and DTM datasets is 1m RMSE, which is consistent with assessment work that I have done with these data when compared to lidar data. Although this is also a commercially licensed product, large parts of Alaska are currently available through the USGS NED, with more data expected to be produced soon (USGS, 2017). It should be noted that the vertical error for the Alaska data is greater due to the complexity of the Alaskan terrain. For the Alaska data, there are no restrictions on use.

Two significant datasets are currently being produced from the twin TanDEM-X/TerraSAR-X satellite-based system, which is operated by the German Aerospace Center (DLR). The first is its commercial WorldDEM product. It has pole-to-pole coverage and boasts a DEM resolution of 12.5m and a 2m relative vertical accuracy (Becek & Becek). There are several DEM product lines available for these data that include the basic core product (which contains artifacts), a hydro-flattened product that enforces representation of lakes as flat and rivers as monotonically decreasing in elevation, and a terrain product that has vegetation and buildings removed. This product line has become widely available in the last year and marks a significant advance in, what is by global DEM data standards, a high-resolution DEM (Riegler & Riegler, 2015). By contrast, until 2015, the only widely utilized global DEM was the SRTM 90m dataset. That changed when, in October of 2014, President Obama announced that the SRTM 30m data would be made openly available. Neither of these datasets are of comparable data quality to the WorldDEM product, particularly in terms of vertical accuracy. For many potential users, though, the WorldDEM data are cost prohibitive to acquire.

The TanDEM-X High Resolution Elevation Data Exchange (TREx) program, led by the US and Germany, is in early stages of production and will essentially replicate the WorldDEM data through a coproduction and data sharing agreement (NGA, 2015). This effort is being coordinated at the NGA offices in St Louis and will take several years to complete. This may offer opportunities for federal agencies and their partners to utilize these data for a variety of projects.

However, the extent to which this is leveraged will depend on the willingness of NGA to take a proactive stance on communicating that opportunity.

Computational photogrammetric techniques for derivation of DEMs from imagery have been an active area of research and commercial integration since the middle of the 20th century (R. Graham & Koh, 2002). Though lidar technologies dominate certain markets where there is sufficient funding to support widespread data acquisition and DEM production, automated DEM production from stereo and multi-look imagery still is a very active area of research and commercial production. Key drivers for this are the rapidly expanding number of electro-optical sensors and platforms, including inexpensive UAV systems, and a corresponding increase in computational and data storage capacity at decreasing cost.

Stereo photogrammetry has enjoyed a long history as the basis for producing high resolution elevation data. Many of the elevation datasets in use today have been developed with hardcopy or softcopy photogrammetric techniques. High-resolution DEM production from commercial imagery is becoming an important source of data where aerial collection of lidar is not cost effective. The most notable ongoing efforts are at the Polar Geospatial Center at the University of Minnesota, being done in cooperation with NGA, the Byrd Polar and Climate Research Center at Ohio State University, and the Ohio Supercomputer Center. The current effort aims to use stereo Digital Globe data collected over the Arctic, Antarctic, and all of Alaska, to produce 2 to 8 m DEM data over the entire region. Though there are a variety of algorithms available for

derivation of DEMs from stereo imagery, this effort is focusing on the use of the Ames Stereo Pipeline Algorithm (ASP) (Capitol, 2016) and the Stereo-Photogrammetric Digital Elevation/Surface Models (SETSM) algorithm developed at Ohio State University (Noh, 2015). While the ASP algorithm has been in use for several years, it uses a pixel-matching approach that can leave voids in the derived DEM . The SETSM algorithm, on the other hand, uses an object-matching approach that yields a DEM with no voids. It should be noted that the absolute horizontal and vertical accuracy of these data are approximately 4m RMSE. With appropriate ground controls this could be improved. Of key importance for this project is that the derived DEMs will be made publicly available.

The multi-look approach uses dense image matching photogrammetric techniques that are based on the same principles as the stereo photogrammetry described above. Multi-look imagery solutions are becoming increasingly utilized for producing high-resolution DEMs on two important fronts: 1) imagery acquired from unmanned aerial systems (UAS) platforms, and 2) high resolution satellite imagery. One major commercial venture that has surfaced in the last 12 month is the company Vricon, which is a partnership between Digital Globe and Saab. Digital Globe brings the largest global high-resolution dataset available to the relationship with its massive archive of GeoEye-1, QuickBird, and WorldView 1-3, and WorldView 4, which is scheduled to be launched later this year. Saab brings a commercial GPU processing solution that can produce high resolution DEMs from the commercial data. Vricon offers commercial data products that

include a surface model, DSM, point cloud, and orthorectified imagery, all at 0.5m resolution with a 3m RMSE positional accuracy. Currently, these products are created on-demand for most areas, but the company has a stated goal of having a global 2m product available within 5 years.

Current trends in remote sensing for disaster response

Current trends in remotely sensed imagery acquisition is a topic that is an order of magnitude greater in scope than the DEM frontier. The number of sensors that are being inserted into low earth orbit has increased greatly over the past few year, and shows no sign of slowing (Grimaldi et al., 2016) A thorough review of the sensors is not possible within the scope for this study, but an overview of them is informative. Historically, space-based remote sensing capabilities have been either national assets or commercial ventures (Coxon et al., 2015). Increasingly though, nations have begun to rely on commercial remote sensing products to support a wide range of information needs, both for electro-optical and radar remote sensing data. A more thorough review of RS data is provided by Grimaldi et al (Grimaldi et al., 2016). In general, this analysis is broken into to the categories of SAR, electro-optical, passive microwave, and radar altimeters. The number of sensors covered is greater than 30, and doesn't even explore many of the newer commercial sensors. There is a veritable explosion of RS data that is becoming available for disaster response, and other applications. The degree to which the geographic registration of these data is sufficient to support the needs of disaster response remains to be seen, but the

upper bound of the registration of imagery with DEM data is largely driven by consumer demand.

The original motivation for considering integration of FLDPLN model with imagery was simply to utilize as a mask for image classification. Subsequent work with gage data has shown that sparse water surface elevation information can be used to create custom flood maps with FLDPLN model output. The goal with this study is to explore the feasibility of using sparse flood boundary points derived from imagery to rapidly create flood inundation estimates. Collectively, there is more than sufficient opportunity with the current availability of high-quality DEMs and imagery to operational this approach if the data quality will support it. For this study, to minimize the variability inherent in "real' data, simulated "imagery" is used to establish a baseline for what is possible. By pursing the objective outlined below, it is hoped that this work can support development of techniques that can be operationalized with satellite imagery to support flood disaster response.

Objective

Develop and test techniques for utilizing point locations derived from modeled flood boundaries that simulate manually interpreted imagery flood boundary points. These point locations will be translated into a set of linearly interpolated depth-to-flood (DTF) values, which will be used to extract custom flood extents from an inundation library developed using the FLDPLN model.

Study Area and Data

Southeast Montgomery County, Kansas, serves at the study area (Figure 3-4). The primary requirement for this analysis is the availability of high quality DEM data. Lidar data were acquired for Montgomery county in the fall of 2012 (published in 2013) as part of a multi-year elevation enhancement campaign supported by the State of Kansas and other local and federal partners (www.kansasgis.org) The data are available as bare earth DEMs with a ground sample distance of 1m, and a stated vertical accuracy of 24cm or better at the 95% confidence level These data are considered to be the most accurate elevation data available for the study area and conform to industry standards for high quality elevation data.

The study area is rectangular in shape and covers an area of approximately 458.6 km^2 (177.1 square miles), with dimensions of 17.62 x 26.03 kilometers (10.95 mi x 16.18 mi) that stretches from the city of Independence, Kansas, on the northern end to past the city of Coffeyville on the southern end. The study area serves as a bounding box that contains the urban areas of Independence and Coffeyville that have been impacted by major floods, covers the floodplain of the Verdigris River that stretches between the two towns, and covers the areas surrounding two USGS stream gages that would be used to generate near real time (NRT) flood maps if the approach outlined in the study were operationalized. There is also one NWS stream gage situated to the north of Coffeyville that is a staff gage, read manually during extreme flood events.

Methods

The primary focus of this part of the study is to present a process that was developed for manually selecting flood boundary points from imagery sources to produce DTF profiles that correspond with a given flood event in the imagery. Operationally, this would be accomplished by developing a GIS-based tool that an analyst would use to select a limited number of visually interpreted flood extent boundary locations from moderate to high-resolution satellite or aerial imagery. The tool would then reference the underlying DTF values and associated flood source pixels (FSPs) to produce a custom flood extent based on the identified points. This objective has two parts: 1) a sensitivity analysis for this approach, and 2) a qualitative evaluation of the resulting flood extent maps. For this study, simulated boundary points (SBPs) will be used to accomplish both objectives.

A) For the sensitivity analysis, two HEC-RAS 2D models were developed for generating simulated flood boundary points. The SBPs were used to evaluate a range of sampling densities within the study area. A random sampling routine was utilized to test 100 simulations at each point density. FLDPLN model FSP DTF profiles were generated for each sample set, which were then used to create custom flood extent estimates that were compared to the modeled HEC-RAS flood extent.

B) Correspondence of modeled flood extents were calculated using the F statistic (Bates & De Roo, 2000; Cook & Merwade, 2009b; Horritt & Bates, 2001; Kastens, 2008; Tayefi et al., 2007)

$$F = 100 * (A_{op}/(A_o+A_p-A_{op})) \quad (1)$$

where A_o: observed area of inundation (model A)

A_p: predicted area of inundation (model B)

A_{op}: area that is both observed and predicted as inundated.

An F-statistic of 100 would indicate perfect correspondence between two flood extents. Areas of non-correspondence will lower the F-statistic score in proportion to the size (area) of non-correspondence. The correspondence statistics were summarized, analyzed, and reported herein.

FLDPLN Model

The fundamental inputs to the FLDPLN model are the sink-filled DEM (FIL), flow direction layer (FDR), and flow accumulation layer (FAC). Some manual editing of the FIL layer was performed to breach flow obstructions such as culverts and dams, and to burn in detailed levee information to ensure accurate representation of flood control structures in the DEM. The FLDPLN model algorithm was applied to sink-filled DEM and FDR data for the study area to generate the DTF and FSP information that serves as the basis for the analysis. The DEM data, described above, were resampled to 5m resolution to balance the computational time required to run the FLDPLN model with maintaining sufficient resolution for flood mapping. The ArcGIS Spatial Analyst tools were used to derive the FIL, FDR, and FAC layers.

Stream segments were derived from the FAC layer using FLDPLN model code that allows the specification of minimum flow accumulation and maximum segment length, which were set to 70 square miles and 5 miles, respectively,

which are the same parameters used for the Kansas SLIE developed at KARS. The minimum flow accumulation thresholding were used to define the minimum contributing land surface area needed before stream pixels are identified as part of the stream network. The segment length maximum was used to divide the stream into smaller segments for processing with the FLDPLN model. This process yielded 14 stream segments on the Verdigris River from just north of Independence to south of Coffeyville. The FLDPLN model also requires that a vertical flood step size and maximum flood height be specified. These were set to 1m and 17m respectively. The FLDPLN model code was then applied using the DEM and FDR data for the study area to produce a library of inundation extents for each stream segment. This initial output is in the form of a MATLAB ".mat" file that contains a list of all pixels inundated at or below 17m, the flood height at which the pixel was inundated, and the FSPs that are linked to FPPs being inundated at that height (Kastens, 2008). The FSPs that comprise the 14 stream segments were consolidated to one segment, as were the FPPs to facilitate the further analysis. The consolidation of segments represents a simplified case of the application of a DTF profile across multiple segments. A detailed comparative analysis of multi-segment profile implementations is left for future studies.

HEC-RAS modeling

A HEC-RAS version 5.0.1 2-D model was constructed with the purpose of generating a large quantity of SBPs for a major flood to approximate imagery-derived flood boundary points. A 2m DEM was used for the HEC-RAS model

terrain input (Figure 3-5). The 2m DEM used for this purpose was the same source data from which the 5M DEM used in the FLDPLN model was derived. The decision to use the higher resolution DEM for the HEC-RAS model and a lower DEM for the FLDPLN model was driven by two considerations. In practice, the 5m DEM is the resolution typically used for wide area, flood response FLPLN model processing, when available. This is done for reasons of computational efficiency, as noted above. The HEC-RAS model, on the other hand, was intended to be the closest representation of reality that was practicable, so the 2m DEM was used. Land use and land cover (LULC) data were used to assign Manning's roughness coefficient values (Manning's n) required for HEC-RAS. The Manning's n values assigned are given in Table1. LULC data were produced by the Kansas Applied Remote Sensing Program in the 2005 timeframe using Landsat data (Figure 3-5)(Peterson et al., 2008).

The HEC-RAS model grid was changed from the 20m default setting to 10m, which was chosen to be small enough to model the hydraulic behavior of the flood while offering reasonable computational time (Figures 3-6 and 3-7). Additional breaklines were added to the model to densify the cells surrounding key landscape features, which included river channels, levees, railroad and road embankments, and other features that might significantly alter flood flow dynamics (Figures 3-8 and 3-9). The time step of 10 minutes was used, which produced a stable model. For the 4.8K flood simulation, a hydrograph was constructed with a base flow of 200 cms, which was interpolated to the maximum discharge of 4785 cms (4.8K-HRM) corresponding to the peak discharge for the

Coffeyville USGS gage from the 2007 flood event. This discharge was selected because it represents a known approximate discharge for a recent major event so the results could be compared to remote sensing imagery acquired shortly after the peak flooding (Figure 3-4). To test the SBP sensitivity, a second flood with a peak discharge of 1000 cms was modeled using the same methods. Detailed flow velocity maps are presented in Figures 3-10 and 3-11 for the area of the Coffeyville refinery, which was severely impacted by the 2007 floods. Figure 3-12 shows the HEC-RAS depth layers for both scenarios across the entire study area.

A raster layer of the flood water surface elevation (WSE) was exported from HEC-RAS for both flood scenarios. These data were resampled from the 2m resolution that corresponded to the HEC-RAS terrain data to the 5m raster grid used by the FLDPLN model. Because the HEC-RAS modeled water surface is a smooth, continuous surface at this scale, no appreciable degradation of the data occurred during the resampling process. The WSE layers were used to determine point location WSEs at FSP locations and other key locations in the study area and to derive DTF values for use in conjunction with the FLDPLN model.

ArcGIS data manipulation

To facilitate the comparison between the FLDPLN and HEC-RAS modeled flood extents, the modeled maximum flood extents for both flows were exported from HEC-RAS to polygon shapefiles that were utilized in the ArcGIS environment. The flood extent was then converted to a raster file sampled to the

same 5m grid that was used for all FLDPLN processing. This ensured a clean comparison between all modeled flood extents, which was performed within the MATLAB environment. A small amount of the modeled data, 1.3 km from the northernmost and 0.25 km from the southernmost extents of the study area, were cut from the data layers to minimize the effects of model boundary conditions and to ensure complete overlap between the HEC-RAS and the FLDPLN modeling areas (Figure 3-13).

To support data visualization and analysis, both the 4.8K-HRM and 1K-HRM maximum flood extent polygon boundary layers were converted to a polyline layer using the ArcGIS "Polygon to Line" tool, after which all vertices in the polyline layer were exported to a point layer using the "Feature Vertices to Points" tool. Manual editing was performed on the resulting point layer to eliminate the points along the HEC-RAS study area boundary that did not correspond to zero-depth boundary points. At this stage the modeled flood inundation extent had been converted to 159,143 and 297,589 candidate flood boundary points for the 4.8K and 1K scenarios, respectively.

Other than the latitude and longitude of the points, there are four other values that that are important for the analysis that were attached to the SBP attributes within the ArcGIS environment. The DTF, DEM elevation, and both the 2m and 5m DEM derived slopes for each point were extracted from the corresponding raster layers using the "Extract Values to Points" tool. At this stage the candidate SBPs were filtered to eliminate ineligible and undesirable points based on DTF and slope values. SBPs that did not possess a DTF value

were eliminated, which was an indication they were on a part of the landscape that was above the 17m maximum DTF output of the FLDPLN model. There were only 14 and 114 such points for the 4.8K-HRM and 1K-HRM scenarios, respectively. Points with slope values of less than 2-degrees were also eliminated (Figure 3-14). This was done to eliminate points that are more likely to have potentially noisy (less certain) DTF values, for reasons highlighted in earlier work using HWM points (Dobbs, 2010). More on this will be discussed in the results section.

Import into MATLAB

The point shapefiles were read into MATLAB. The latitude and longitude values were converted to pixel index values that corresponded to the input DEM. Once each valid SBP was associated with its corresponding raster file coordinate, the FLDPLN output file was used to determine the associated FSP. The ability to make this association is a key functionality that can be leveraged for many of the innovative application of the FLDPLN model, along with the ability to return all floodplain pixels associated with a given DTF value, and to do so for values that can vary on a per pixel basis for all stream FSPs.

Stream profile

The stream profile is a key tool in all the analyses outlined below. Stream pixel locations along the merged segment, described above, are assembled into an ordered list of locations, from upstream (US) to downstream (DS). Because these pixels are derived from a sink-filled DEM, the corresponding stream surface (as

represented in the DEM) is guaranteed to have corresponding elevation values that decrease from US to DS, or in some cases are unchanged between successive pixels. Small level areas occur naturally in pools between stream riffles. Larger flat areas can occur in reservoirs or in-line dams. In this study the overall stream segment comprises 11,220 5m pixels. There are 10,516 stream pixels in the subset of the study areas that is used for F-statistic calculations (Figure 3-13).

Randomized sampling

To test the sensitivity of the boundary point-informed DTF profile approach, a randomized sampling routine was developed in MATLAB that samples from equally sized elevation zones from the SBPs. For instance, if 10 SBPs are desired, the elevation range of SBPs is divided into 10 equal parts and one point is selected from each. This process was repeated 100 times for each SBP sampling size. Three sets of sampling size ranges were tested. From 5 to 100 points at intervals of 5 points (20 sets of 5), from 100 to 1000 at intervals of 100 points (10 sets of 100), and 1000 to 10,000 at intervals of 1000 (10 sets of 1000). This was done for both the 4.8K and 1K flood levels. In all, 8000 simulations were performed across the two flood levels.

Interpolation

For each sample set (all 8000) a custom DTF profile was generated. For each set, the FSP associated with the FPP that corresponded to the SBP was determined. If multiple points mapped back to the same FSP, which may not occur for small samples, but is certainly the case for larger samples (Figures 3-

18,19,20), the mean value for that FSP was determined and used for interpolation purposes. Additional analysis and interpretation of this topic is provided in the results section.

Once the DTF and FSP values for all the SBPs have been determined, a linear interpolation is applied to define the DTF value associated with the stream pixels between SBP FSPs. For each sequential (based on stream-ordered occurrence) FSP pair, the DTF for stream pixels between SBP FSP_a and SBP FSP_b is determined using the following formula:

$$DTF_i = DTF_a + (DTF_b - DTF_a) * (D_{ai} / D_{ab}) \quad (1)$$

where D_{ab} is the raster distance between upstream FSP_a and FSP_b, D_{ai} is the raster distance between upstream FSP_a and FSP_i along the stream pixel path between FSP_a and downstream FSP_b, and DTF_a and DTF_b are the DTF values for the FSP_a and FSP_b, respectively. Distance along the raster flow path is determined by assigning a value of distance = 1 to FSPs with a corresponding FDR value of 1,4,16, or 64 (cardinal directions) and distance=1.4142 for those with a corresponding FDR value of 2, 8, 32, and 128 (diagonals). Each calculated segment is written back to a FSP DTF profile for later use. DTF values from the upstream-most and downstream-most SBP FSP were assigned to all remaining upstream and downstream FSPs, respectively. The fewer the number of SBP samples, the longer these end sections will be. This was to provide DTF values where it was not possible to interpolate because there is no ‘next’ SBP mapped to a FSP.

F-statistic calculation

First, a list of all raster pixel indices is generated that corresponds with the refined study area. This is used to mask the pixels in the HRM scenarios to limit the area of analysis to the refined study area. Once all stream pixels have DTF values assigned based on the linear interpolation technique outlined above, calculation of the corresponding F-statistic is performed by querying the FPP data file for the set of floodplain pixels linked to FSP_i that correspond to the condition $DTF_{FPPi} <= DTF_i$. This list is first intersected (masked) with the list of pixels in the refined study area as outlined above. After identifying the flooded pixels for all FSPs and merging the results, the flooded pixel set is intersected with the corresponding masked HRM flooded pixel list. The count of pixels in the resulting intersection is tallied and used to calculate the F-statistic correspondence (1). The correspondence statistics are summarized, analyzed, and reported below.

Results

Although the original intent of this research was to utilize boundary points that were derived by an analyst from imagery acquired during or shortly after a flood, it was decided that the focus should first be on establishing a baseline against which to measure future studies, and to understand the advantages and limitations of the approach. So, by design, this current study minimizes the effects that imagery registration error would have on results, and the effect that imagery resolution might have. Due to the high number of SBPs that result from

transforming the modeled inundation boundaries into points, there is a rich source of data to explore for a baseline analysis.

HEC-RAS model

The HEC-RAS 2D model was an effective tool for the generation of SBPs. Because the goal of this study was to produce the most accurate representation of floods corresponding to the two discharges modeled, care was taken to accurately represent significant features in the landscape that would affect flow dynamics. This was particularly the case for levees, roads, railways, and containment structures (Figures 3-8 and 3-9). These features also represent locations where an analyst might identify flood boundary locations during operational implementation of the technique, so it important to represent them accurately. These features, however, will often have relatively high slopes, so also may need to be avoided in the operational case. Inspection of the HEC-RAS model output velocity and extent output shows that the terrain features are represented in the model and that the flow paths behave as expected in the vicinity of such abrupt terrain features (3-10 and 3-11). Several iterations of the HEC-RAS modeling were performed to achieve the expected behavior. The primary changes between iterations involved the addition of breaklines.

Another important feature of note is the low velocities at the water-land interface. This is a desirable quality that closely mimics the ideal inundation boundary. High velocity areas can have water surface elevations that respond to local conditions and flow restrictions, which may not be representative of nearby, low velocity flood boundaries. This may be one advantage that the flood

boundary approach has over gage-based DTF interpolation techniques. Gages are often located at bridges, which, aside from the convenience of access to supporting infrastructure, offer a well-managed and consistent flow restriction that makes rating curve determination reliable. The drawback for the FLPLN model utilization of gage stage information is that this restriction will also tend to raise the water surface elevation at that point over what it would be naturally. For instance, high water marks at obstructions subjected to local high velocities can be considerably higher than the representative WSE in that area due to stagnation effects that convert the velocity head to a local rise in the water surface at the obstruction. Because imagery-based flood boundary pixels offer thousands of potential indicators of WSE, this approach has the potential to be less sensitive to singular, channel-positioned inputs, and has many opportunities for point selection across a variety of landscape positions, most of which are far from flow restrictions.

The quantity of SBPs generated by both flood levels was more than sufficient for analysis. For the 4.8K HRM, 159,257 points were generated, of which 114 did not intersect with the FLDPLN model results at <= 17m DTF and hence were eliminated. For the 1K flood, 14 points of 297,603 fell outside the FLDPLN modeled area and were also eliminated. These points fell in high slope areas that would be sensitive to horizontal positioning misalignment. Figure 3-15 which plots the elevations extracted for all SBPs from the 2m FIL DEM and the 5m FIL DEM, shows that there is scatter around some features of the landscape. This is expected to be predominantly associated with high slope features, though

this was not investigated here. This does have implications for operational use of the boundary point technique because these same points could cause undesirable variation in the DTF profile, particularly for the low sample cases. These effects might be minimized for higher sample cases if an averaging or median value strategy were imposed.

Another interesting, if not unexpected, consequence of downsampling from 2m DEMs to 5m DEMs is shown in Figure 3-16. Higher slope values present in the 2m DEM are suppressed in the 5M DEM. This is another factor to keep in mind in future studies as boundary point selection guidelines are developed, for both manual interpretation and automated procedures. In practice, land cover would also be an important factor for determining boundary point selection. High vegetation, such as trees and tall crops, can obscure the land-water interface. One other consideration is illustrated in Figure 3-17, which shows a scatter plot for right bank and left bank point DTF values vs. elevation (note that left and right bank are defined relative to the direction of stream flow). This plot suggests that in the wide section of the floodplain, the right bank points have DTF values that are about 1m lower than left bank points at the same elevation. This is likely due to the fact that the approximated WSE of the FLDPLN model is not planar is some cases. The reason for this is a subtle difference between the way that the FLDPLN model identifies the FPP DTF value relative to the FSP. Though a thorough review of these considerations is beyond the scope of this study, future work should consider these factors for both simulated scenarios and operational application development.

FLDPLN Model SBP F-statistic

The F-statistic results are presented in three graphs that represent low, medium, and high number ranges of SBPs. The results in Figure 3-18 show the F-statistic for 5 to 100 SBPs simulation, at increments of 5 points. For each simulated SBP quantity, 100 sets of randomly sampled points were analyzed. This figure, then, summarizes the results of 4000 separate simulations. For both the 4.8K and 1K scenarios, the average F-statistic is plotted, along with the maximum, minimum, and inner quartiles. Figures 3-19 and 3-20 go on to add the results of simulation for 100 to 1000 SBPs and 1000 to 10,000 SBPs, respectively. These simulations were conducted at 100 and 1000 SBP intervals, respectively. Figure 3-17 summarizes a total of 8000 SBP simulations.

5 – 100 SBP

Understanding the behavior of the sparse, imagery-derived flood boundary points is important to determining the utility of the approach and to help guide research and application development directions. Stream length for the study area is 62km, so the range is a good representation of what roughly one SBP per 10km to one SBP per 1km would behave like. This is a reasonable target range that, if practicable, could be developed into a valuable application for flood mapping.

The 4.8K case saw very good results with even 5 points (Figure 3-18). The average for 100 simulations was 90.7, with a range of 80.0 to about 94.6. By 100 SBPs the average for 100 simulations increased to 96.0, with a range of 93.8 to 96.6. Not only do these results show that the approach can be highly accurate,

the approach is quite stable. Another interesting result is shown in Figure 3-18, which plots the number of unique FSPs that the SBPs map to. At low sample numbers the relationship is nearly one to one, with an average of 4.6 unique FSPs for every 5 SBPs selected. But, for selections with 100 SBPs, the average number of unique FSPs falls to 27.9. This exposes some interesting characteristics of the many-to-one relationship of FPPs to FSPs. A query of all 44,363 and 158,357 SBPs for the 4.8K and 1K scenarios shows that there were only 169 and 690 unique FSPs for all SBP points, respectively. In this study, multiple points were averaged when determining the DTF that would be used in the FSP DTF profile. In practice a median value approach might be more favorable to mitigate the impact of outliers, or perhaps some other direct strategy to filter outliers.

The 1K case showed results similar behavior, but with a lower average F-statistic at all corresponding sample levels, with an average F-statistic of 67.1 for 5 points and 83.5 for 100 points (Figure 3-18). The data also show a greater variability at all levels, with an F-statistic range from 48.2 to 79.1 for 5 points and 80.9 to 85.4 for 100 points. The average number of unique FSPs also varied from 4.9 to 40.7, respectively. The trend and magnitude of unique FSPs is, as expected, relative to the corresponding number of unique FSPs overall. What is not explained by the data itself is why there is a clear difference between achievable accuracy between the two different flood levels, but this trend has been observed previously when comparing the FLDPLN model to the HEC-RAS and HAZUS models at a range of flood levels (Figure 3-2 and 3-3) (Dobbs, 2010).

100 -1000 SBP

For the mid-range of SBP point selection, 100 to 1000, all the trends continue for both the 4.8K and 1K scenarios (Figures 3-19 and 3-24). F-statistics exhibit strong asymptotic behavior in this range, converging to an average F-statisticvalues of 96.8 and 85.2, respectively. The range of values tightens for both as the number of SBPs increases, though the 1K scenario does so more slowly. The inner quartiles for both, however, are very narrow relative to the min-max spread in this range. This range of SBP selection density is interesting for two reasons. For lower flood levels, this is the range within which additional points might help improve map accuracy for manual image interpretation, and this is also the range where automated techniques might start to be employed that incorporate automated image classification boundary points to define FSP profile development. This approach is part of the conceptual framework in Figure 3-1.

1000 – 10,000 SBP

The results for the high range for SBP point selection clearly establish an upper bound for the correspondence that is possible with the given inputs. The average F-statistic is 96.9 and 86.7 for the 4.8K and 1K scenarios with 10,000 SBPs selected, and corresponding 118.5 and 279.8 unique FSPs. One interesting attribute of the distribution characteristics exhibited in Figures 3-21:23 is that the max-min and inner quartiles for unique FSP counts do not converge as they do in the F-statistic data. The cause for this is distribution of FPPs mapped to FSP. A close examination of the data indicates that, of the unique FSPs for a given flood level, a handful are linked to a majority of the FPPs, while a larger proportion of

the FSPs are linked to a smaller number of FPPs. Hence, as more samples are taken, the more minor contributors are likely to be chosen. Collectively, this set of simulations meets the goal of characterizing the response of the modeling approach with these inputs.

Conclusions

Enabling technologies for future solutions that integrate satellite and aerial imagery-derived information with supporting datasets are emerging at an increasing rate. This research shows that integration of non-traditional, terrain-based datasets can yield new methods for rapid flood inundation mapping for disaster response. Using the inputs and methods in this study, the data show that higher magnitude floods require fewer boundary point inputs than lower magnitude floods in terms of accuracy and stability. The data also show that there is an upper bound to the accuracy that is achievable in this study setting, regardless of the number of boundary point inputs, which is an important finding. This can help guide protocols for image point inputs that limit the effort expended by analysts for manual point extraction. It also can be used to communicate uncertainty of mapped flood estimates. Examination of and characterization of FLPLN model behavior for this application, and the preparation of graphical representation of the data from new perspectives has led to a greater understanding of the capabilities and limitations of this approach.

In general, if similar levels of accuracy can be extended to satellite-derived boundary points, this method shows promise for achieving the goal of improving mapped flood extent estimation and expedited delivery of useful information for disaster managers. The logical next step in this line of research is the application of the techniques established in this paper to satellite imagery that is collected coincident with major floods. The most straightforward of these applications would be to test the use of analyst-derived flood boundary points to produce flood inundation estimates in the same manner that was used for the SBPs in this study. Coupled with FLDPLN model outputs, this would be a valuable contribution toward the development of tools that an analyst could use to decrease the time needed to produce flood inundation extent estimates from imagery. The computer code and data developed for this study can be leveraged to a wide range of follow-on research.

Although only slope filtering was performed for this study, future work could take advantage of these data in combination with landcover data to provide more refined simulation that would eliminate forested areas, for instance, or other areas of tall vegetation that would not likely obscure or obfuscate useful flood boundaries identifiable in imagery. In addition, locational inaccuracies in image registration or analyst point selection could be simulated using point location bias or random offsets of different magnitudes.

Beyond interactive applications that would require user input, exploration of applications that would use automated techniques to fit a DTF-informed flood extent envelope around classified or quantitatively characterized flooded pixel

values is also a line of research in need of exploration. This approach presents several interesting challenges that would require a particularly close examination of errors of omission and commission in the classified imagery. Because the nature and magnitude of flood classification errors vary by factors that include spatial, spectral, temporal, and radiometric resolution, as well as weather, timing, and classification technique, it would be useful to lay out a research plan that introduces and tests the effects of these sources of error independently of others. Previous work by (Bates & De Roo, 2000) has shown that the upper bound to reference flood inundation estimates is approximately 90%, so the methods presented here are near the observational limit. If an analyst is only going to be able derive 90% of the inundation extent via tedious manual interpretation of the data using thousands of points, and if similar results can be reached with only tens, or even hundreds of points, there is value in the methods presented here.

Tables

Table 3-1: HEC-RAS Manning's n coefficients used for HEC-RAS 2D modeling.

Land Cover	Base Manning's n
Cropland	0.035
CRP	0.040
Grassland	0.030
Other	0.040
Urban industrial / commercial	0.050
Urban open land	0.030
Urban residential	0.045
Urban water	0.025
Urban woodland	0.100
Water	0.035
Woodland	0.100

Figures

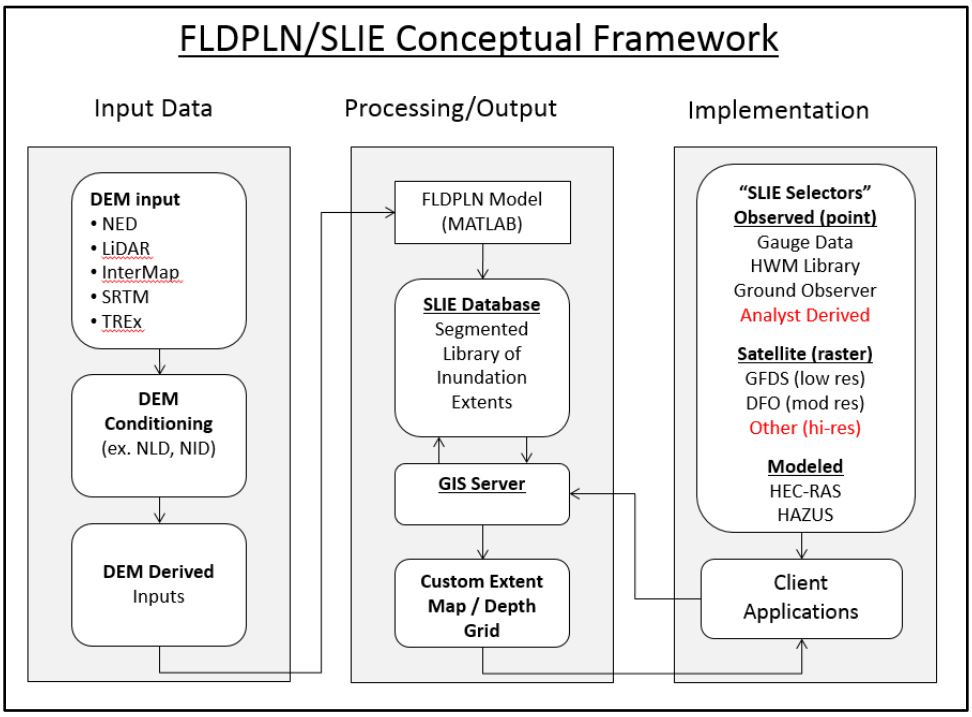

Figure 3-1: Conceptual Framework. Workflow and conceptual implementation of the FLDPLN model. Red text indicates the focus of the current work.

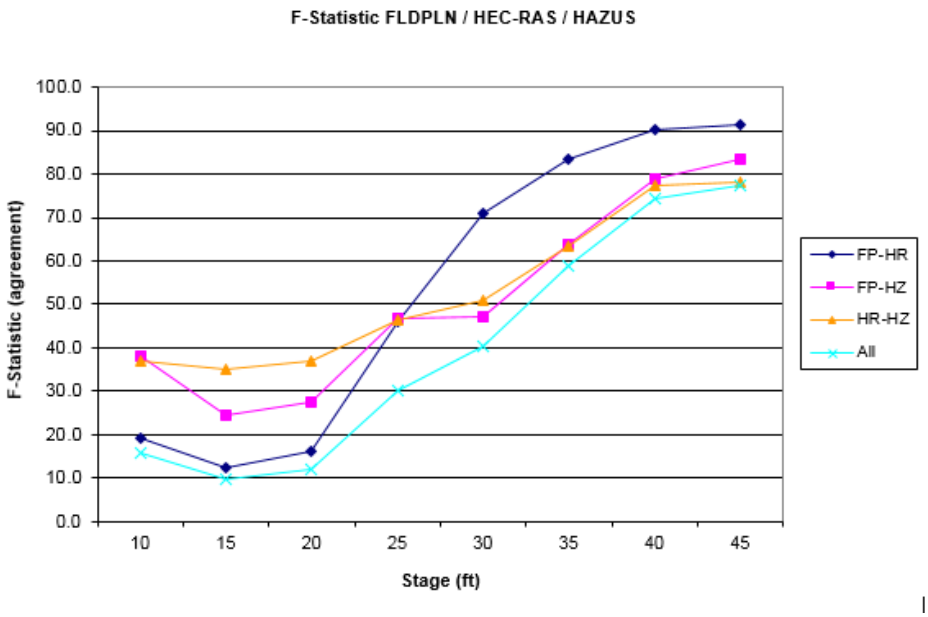

Figure 3-2: F-statistic vs. stage for all model pairings and between all models (HEC-RAS, HAZUS-HM, and FLDPLN) (Dobbs, 2010).

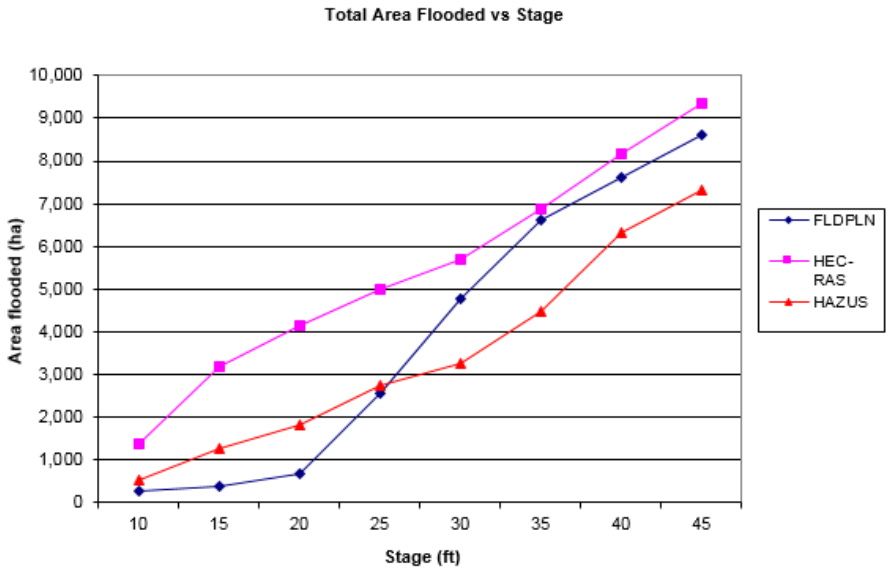

Figure 3-3: Total area flooded with each model vs. stage (HEC-RAS, HAZUS-HM, and FLDPLN) (Dobbs, 2010).

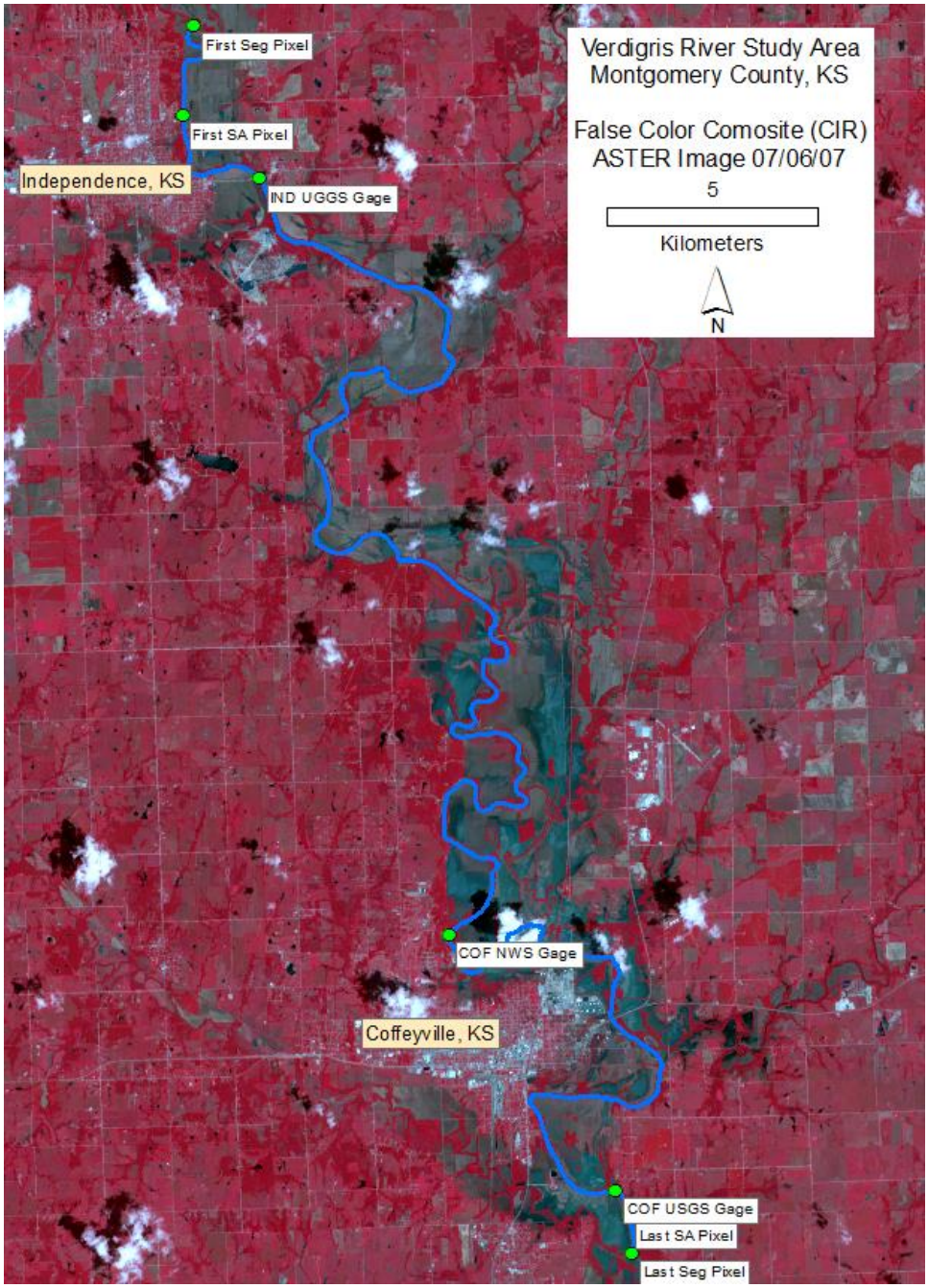

Figure 3-4: ASTER flood image. The base image is a color infrared, 15m resolution ASTER image acquired on July 6th, 2007, four days after flood crest. Dark areas along the Verdigris River are either standing water still pooled in the floodplain, or areas denuded of vegetation by flood waters. Brighter red areas within the flood zone are woodland canopies that are minimally impacted by flood waters.

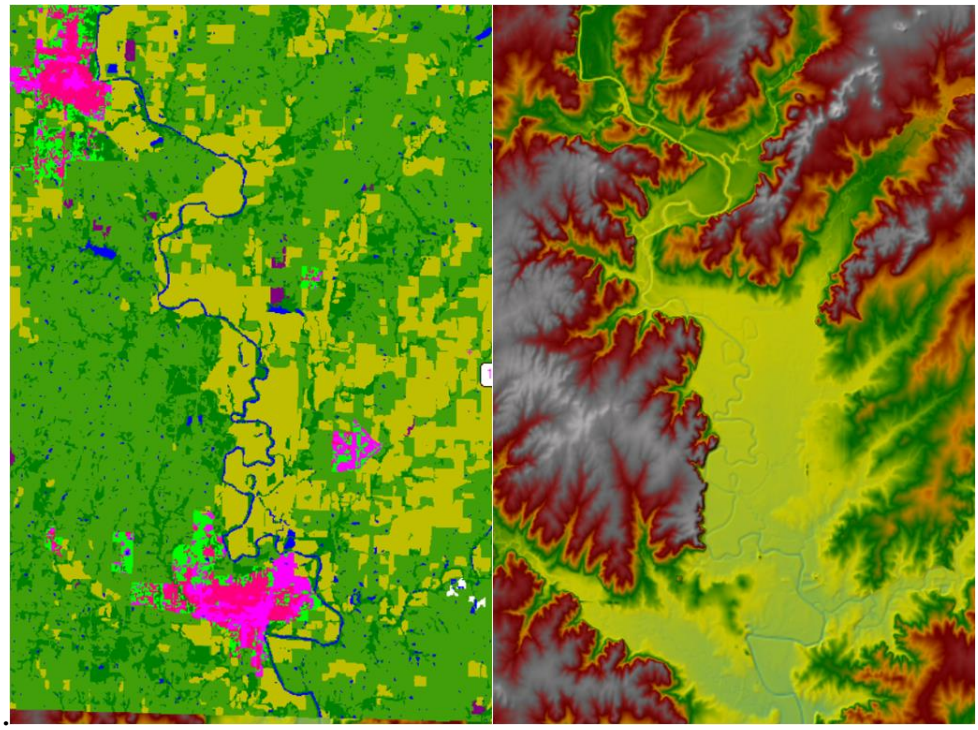

Figure 3-5: Study area. LULC and terrain data inputs to HEC-RAS model.

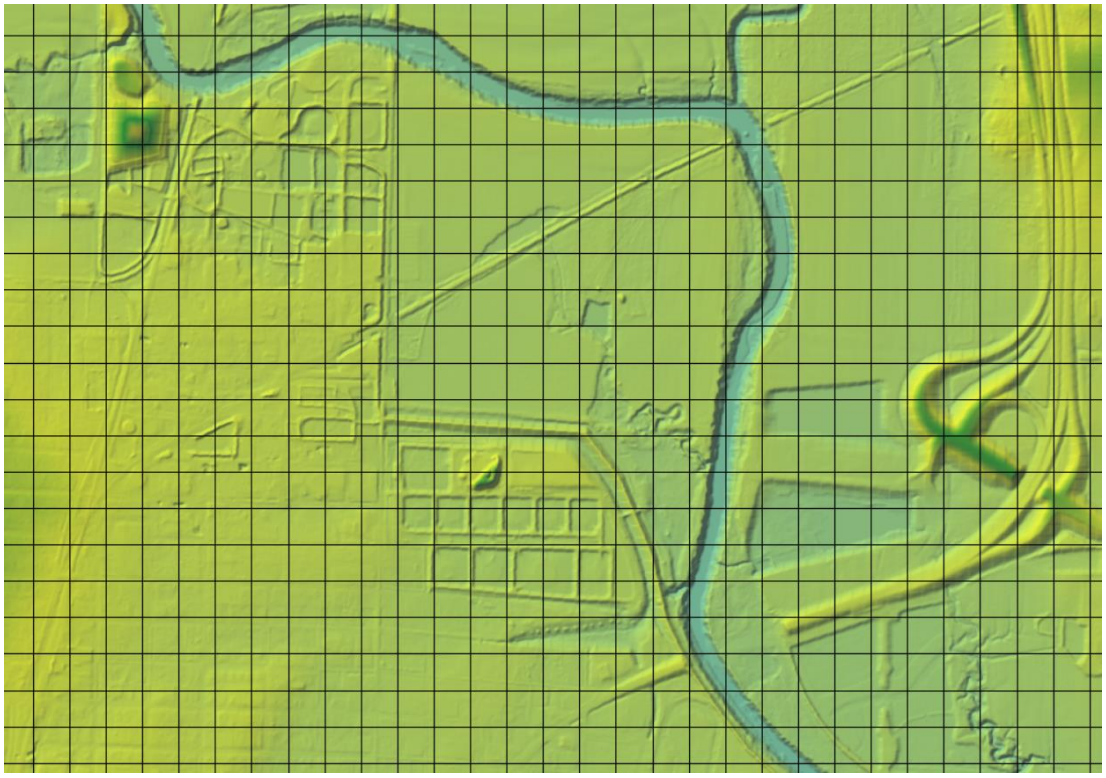

Figure 3-6: HEC-RAS terrain with 20m grid and no breaklines

Figure 3-7: HEC-RAS with 10m grid, breaklines, and densified cells.

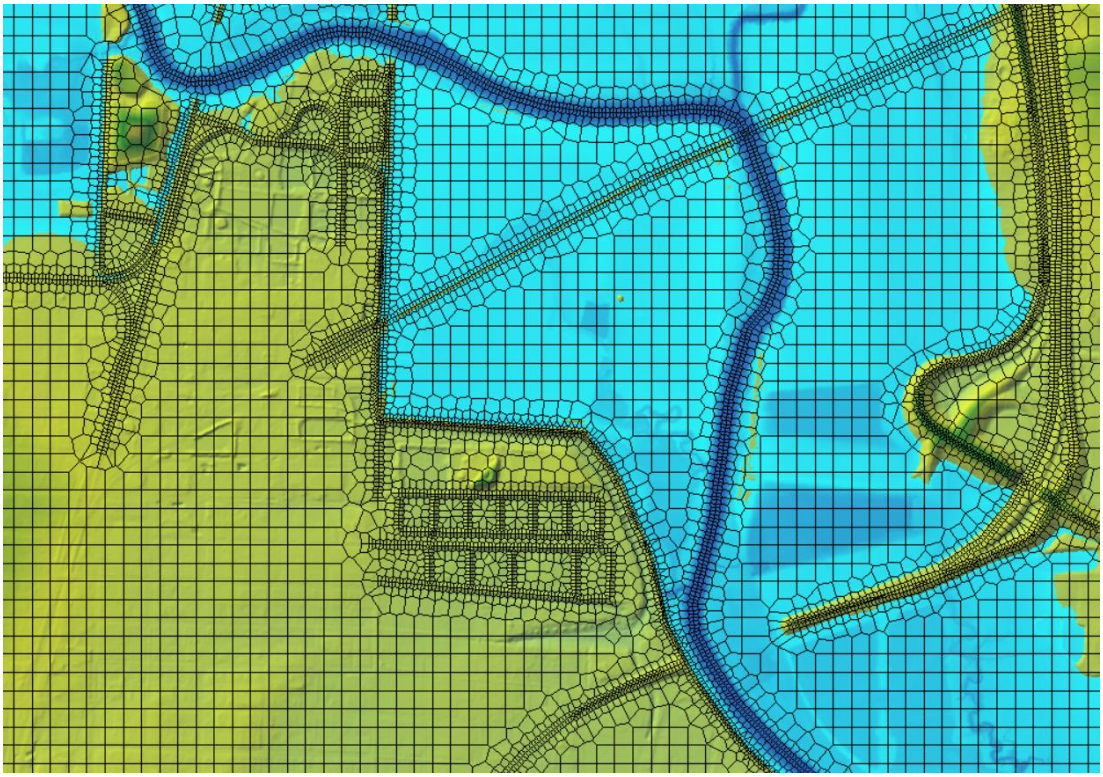

Figure 3-8: 1K cms flood at the Coffeyville Resources Refinery along the Verdigris River.

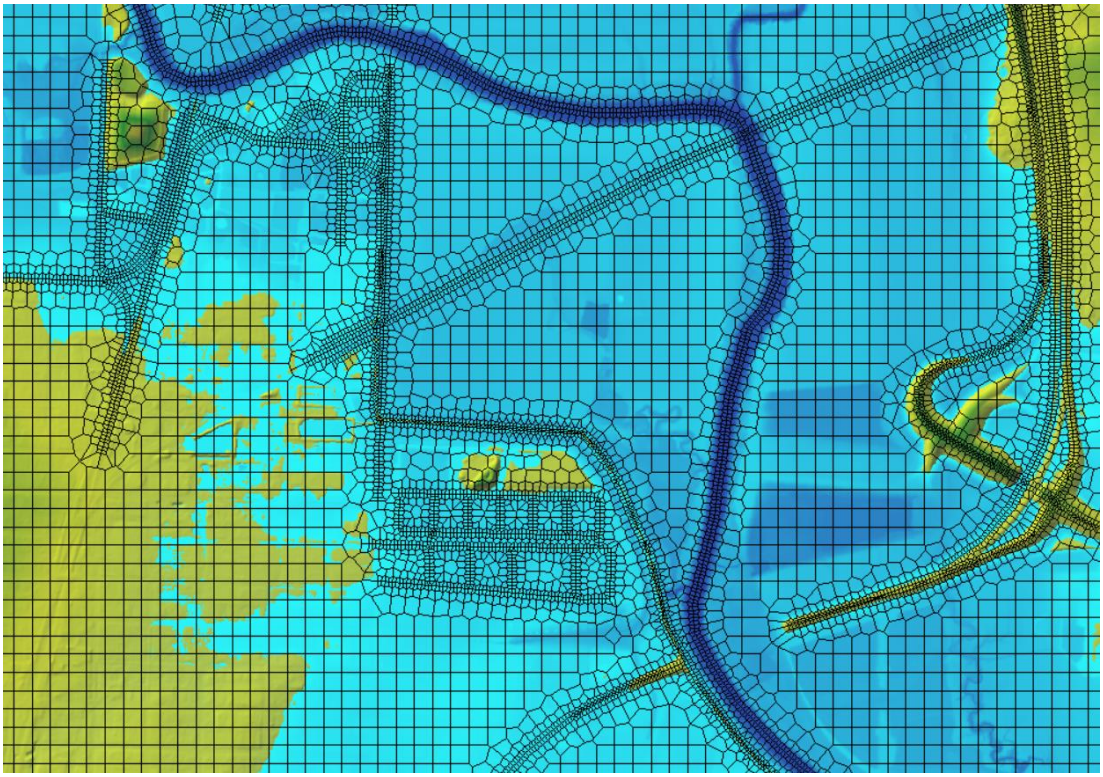

Figure 3-9: 4.8K cms flood at the Coffeyville Refinery along the Verdigris River.

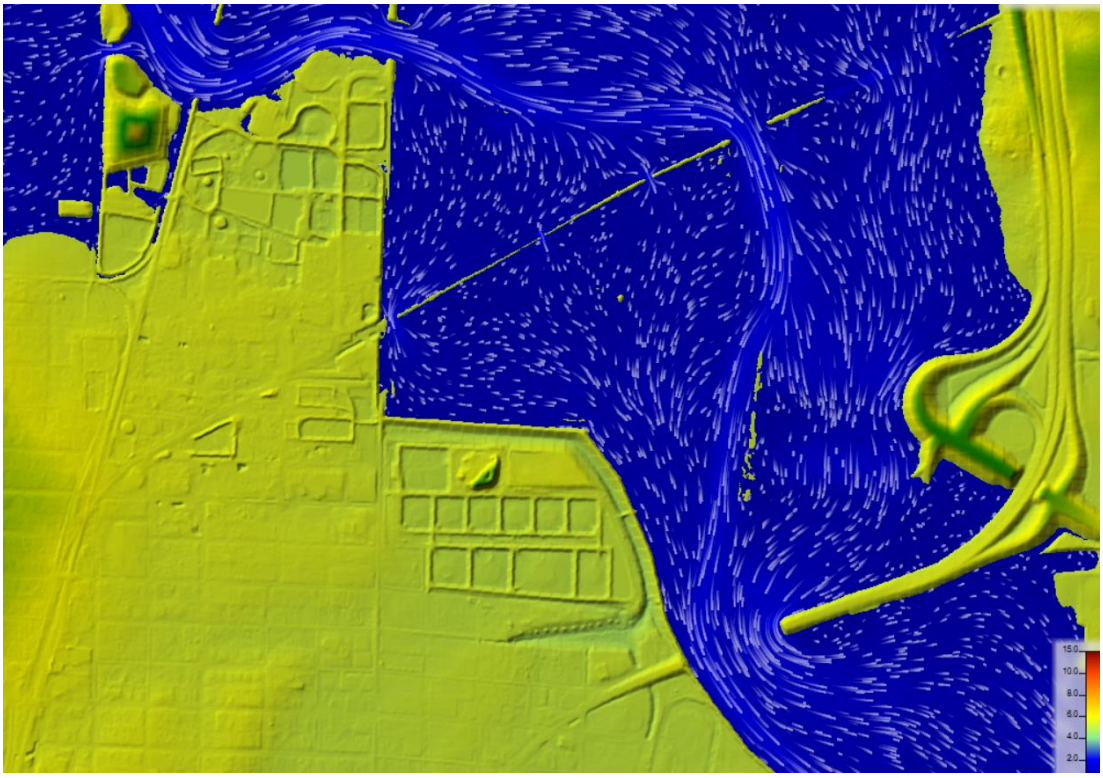

Figure 3-10: HEC-RAS velocity map for 1K cms flood.

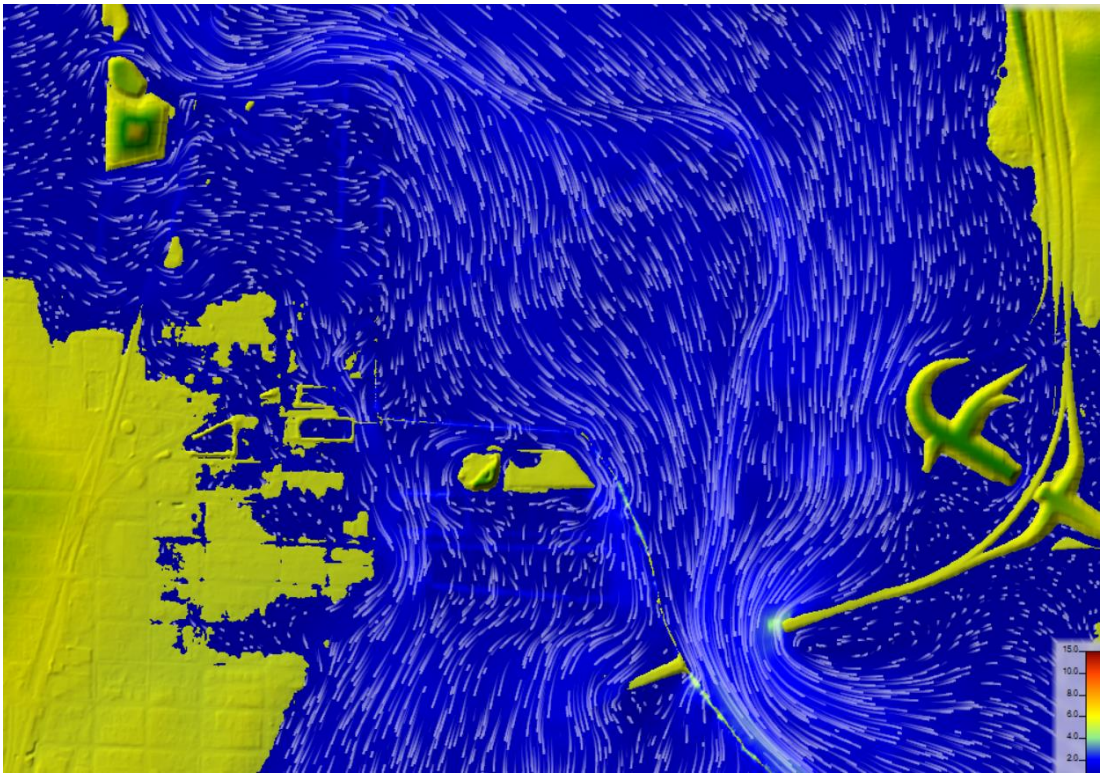

Figure 3-11: HEC-RAS velocity map for 4.8K cms flood.

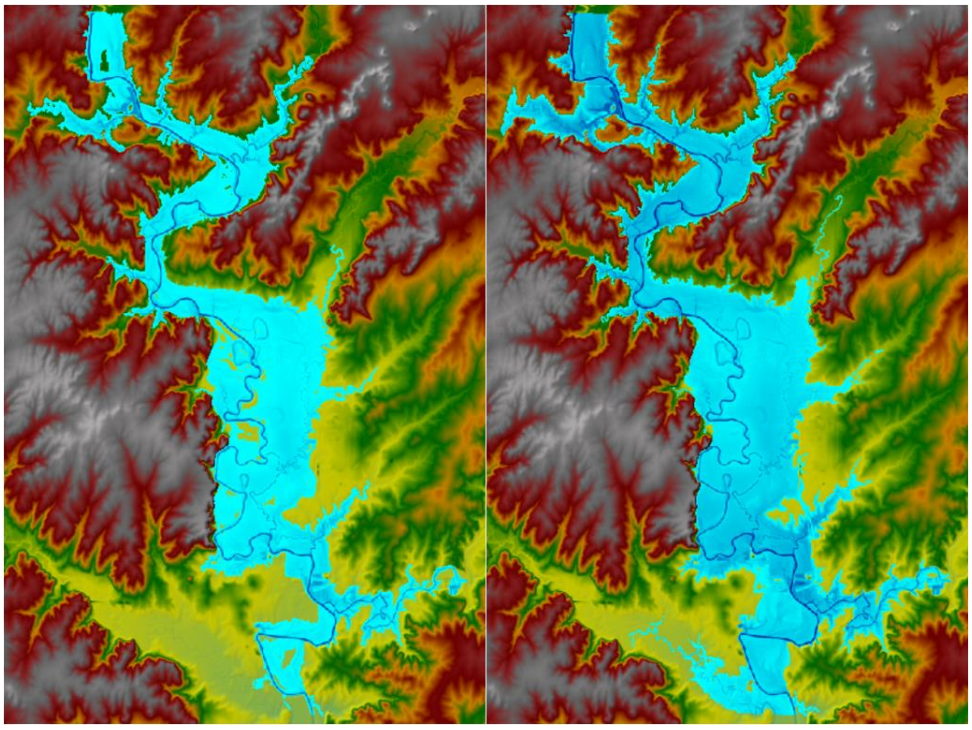

Figure 3-12: HRM Depth Maps Flood depth maps from the 1K and 4.8K flood scenarios.

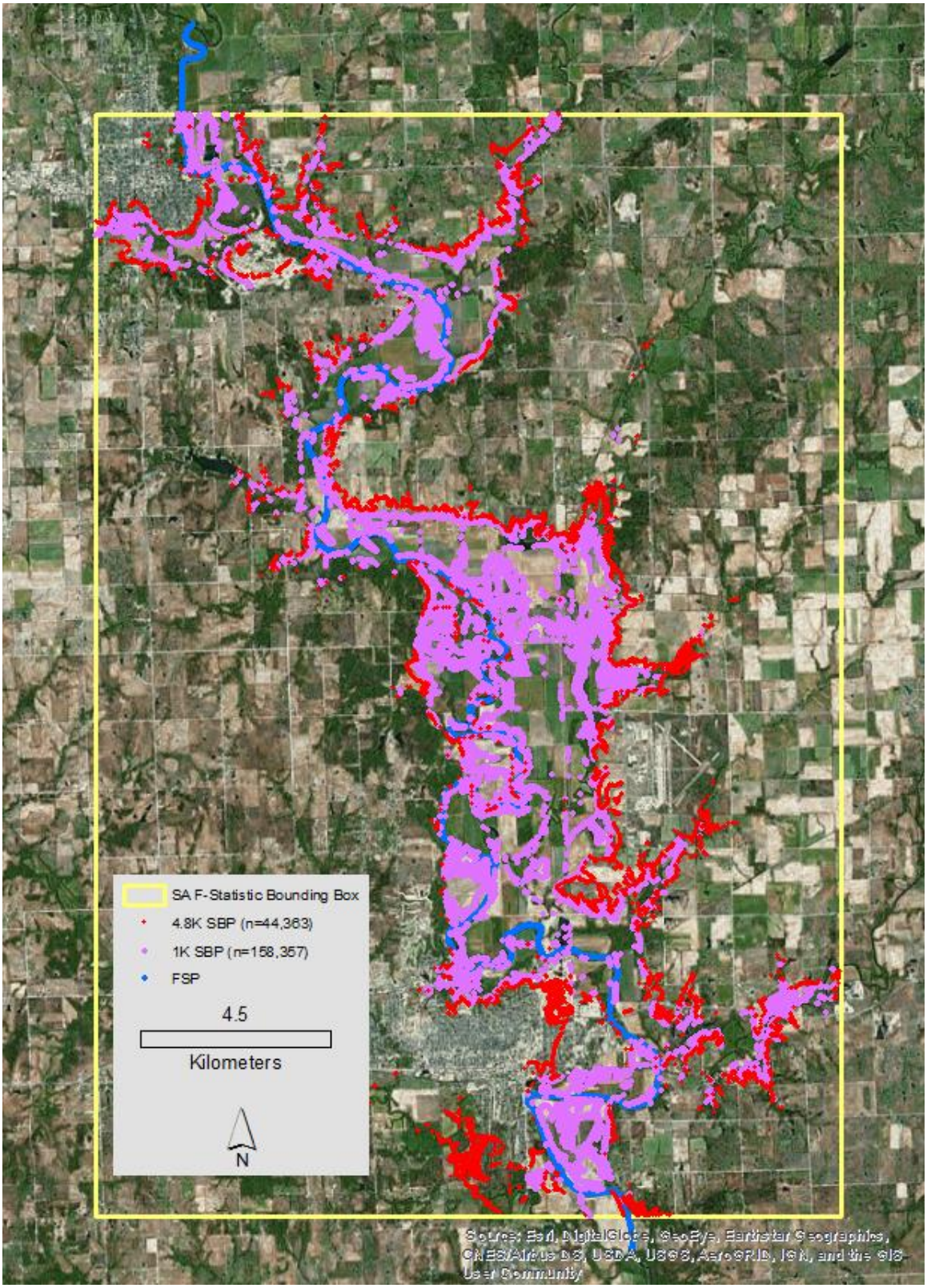

Figure 3-13: Map of all SBPs for the 4.8K and 1K scenarios. FSPs are also shown in blue. Background is recent, non-flood imagery from ERSI World Imagery server.

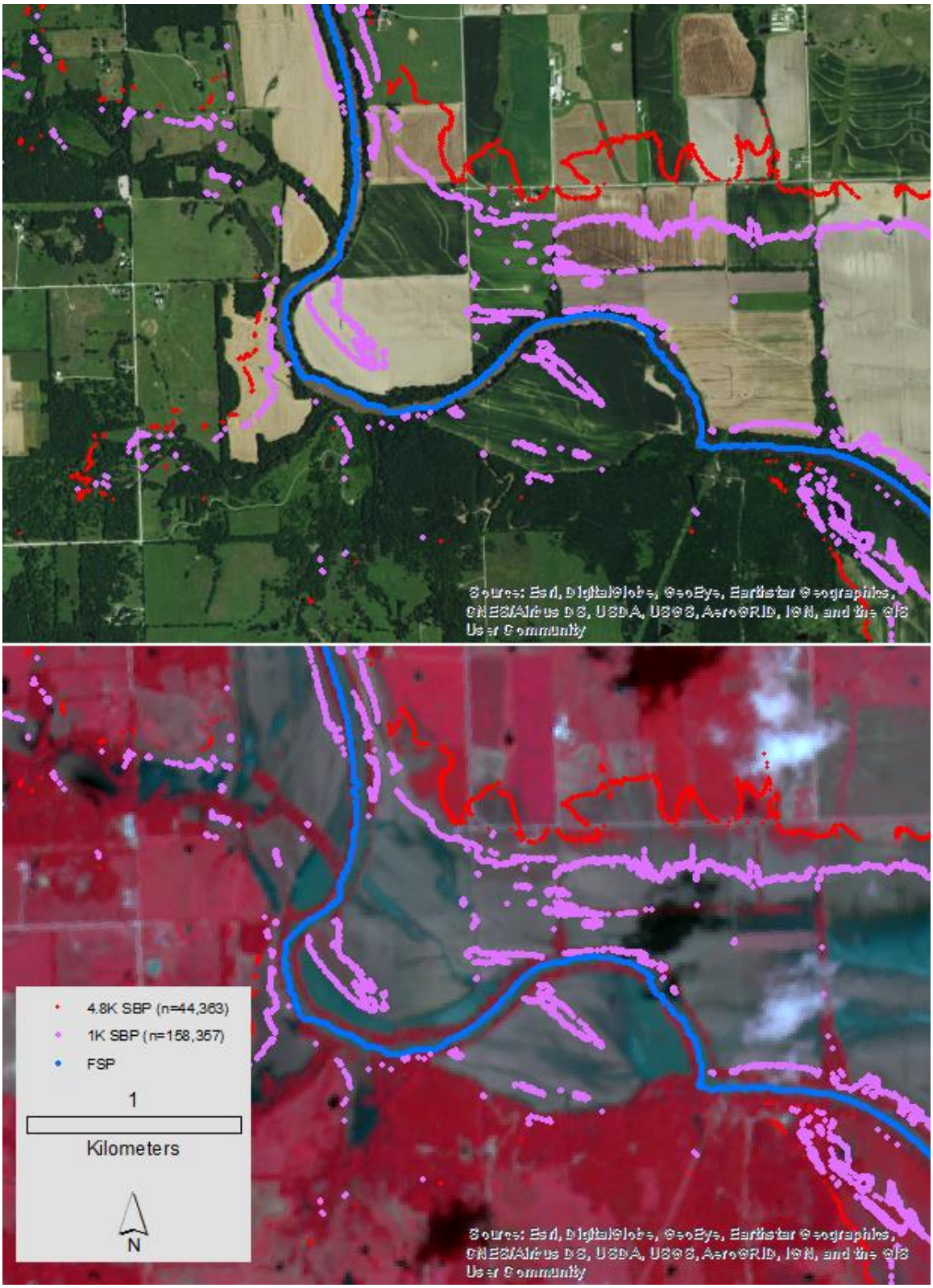

Figure 3-14: (Top): 4.8K and 1K and FSPs over recent, non-flood, high resolution imagery. (Bottom) The same points over ASTER 15m CIR imagery from July 6, 2007. Some standing water can be seen in the imagery along with flood-damaged vegetation.

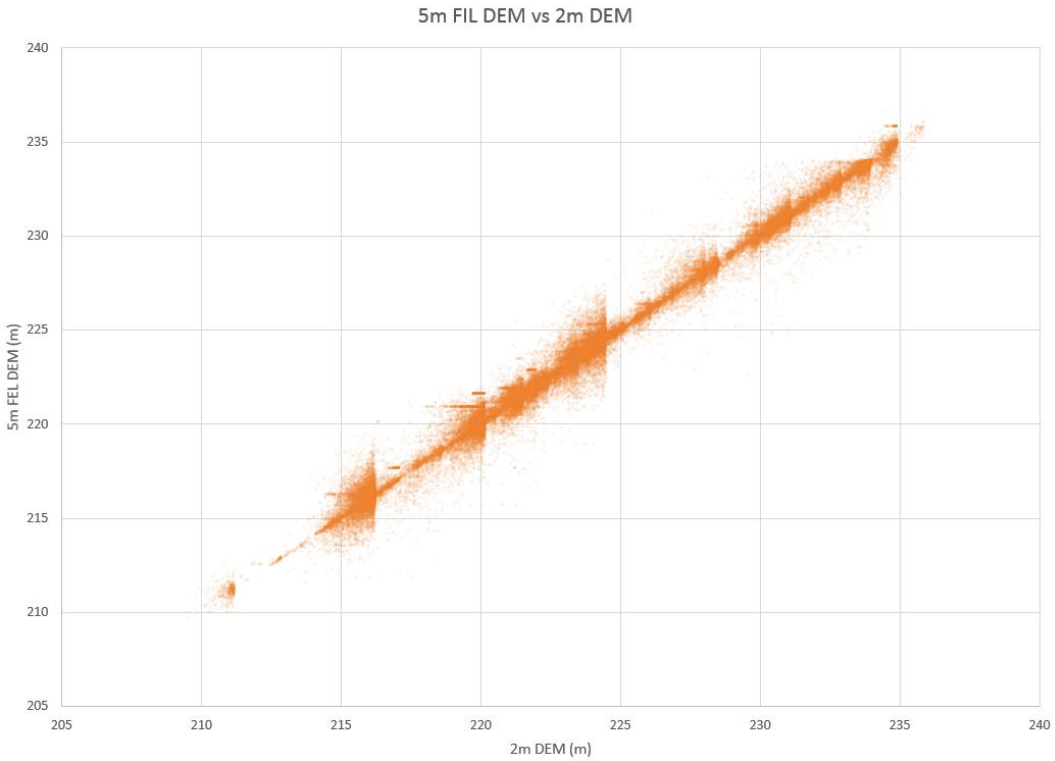

Figure 3-15: The effect of downsampling the resolution of DEM data from 2m to 5m is shown in this graphic. Understanding these subtle factors is important when relying on the errors and uncertainty that will be present when relying on image boundary points as the source of information the constructing DTF profiles for custom flood map generation.

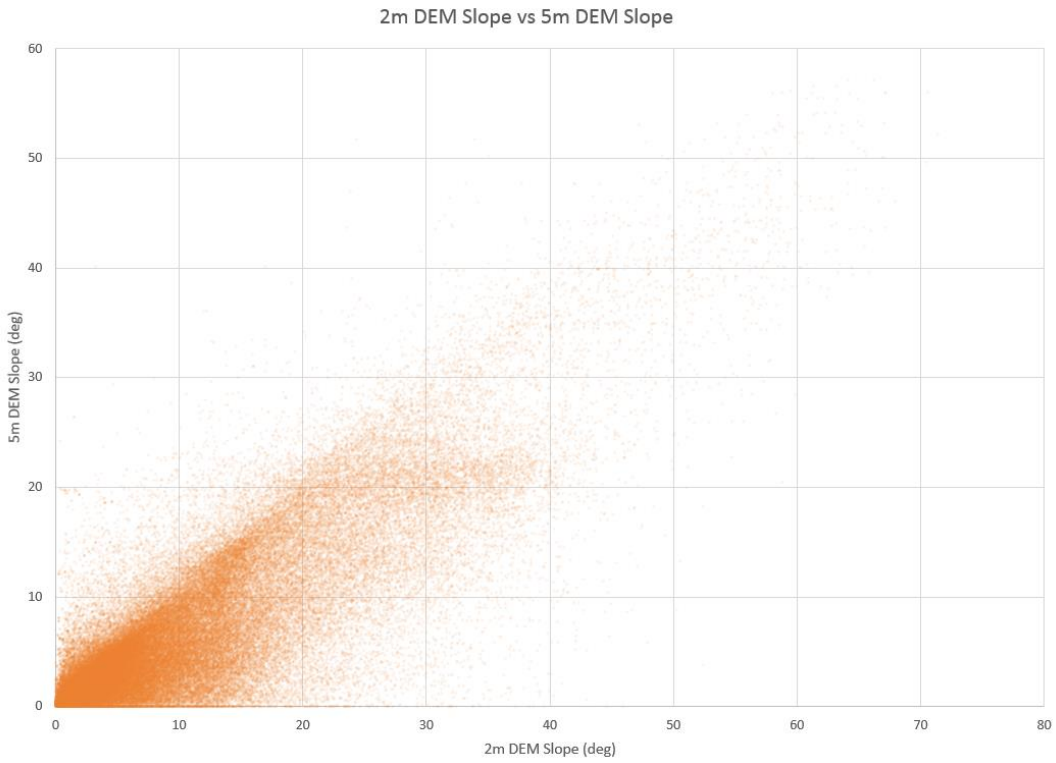

Figure 3-16: This scatter plot of 2m slope values vs. 5m slope values shows that, for this sample of modeled flood boundary points, there is a noticeable suppression of slope values that occurs for many points during the resampling process. Horizontal position errors could arise during the flood boundary point selection process, through registration errors between terrain data and imagery, or due to imagery or DEM resolution factors. In practice, it will be important to avoid high slope area to minimize the

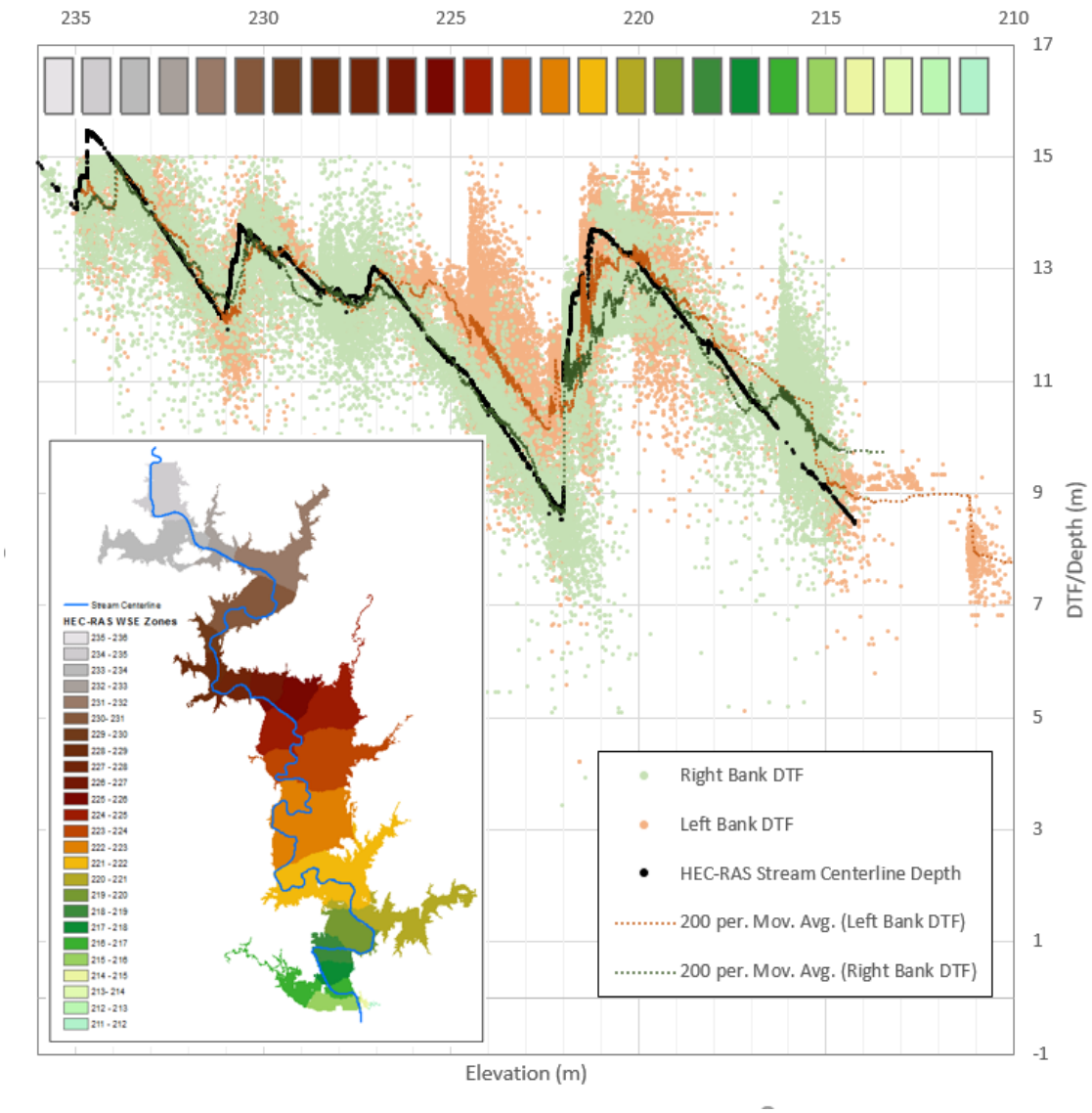

Figure 3-17: Scatter plot for right bank and left bank point DTF values vs. elevation (note that left and right bank are defined relative to the direction of stream flow). This plot suggests that in the wide section of the floodplain, the right bank points have DTF values that are about 1m lower than left bank points at the same elevation. This is likely because the approximated WSE of the FLDPLN model is not planar is some cases.

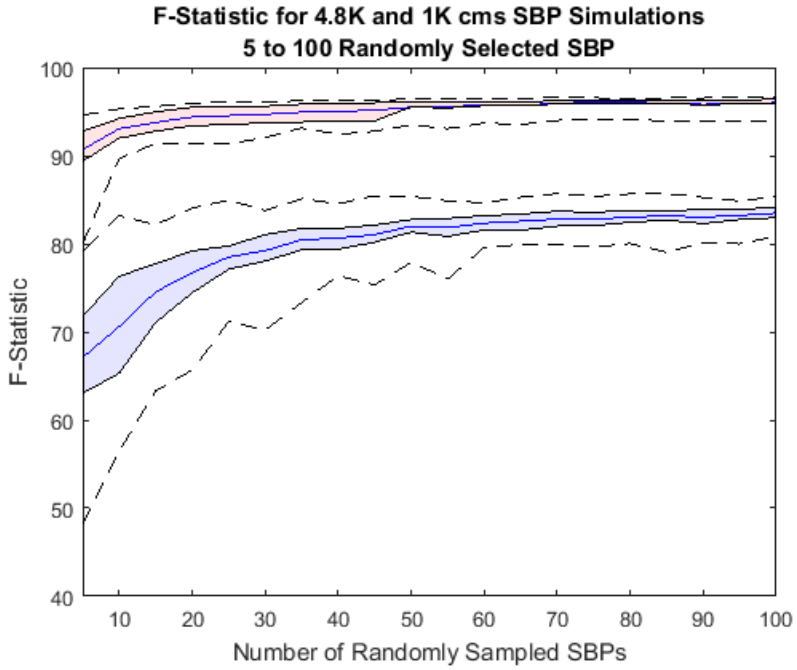

Figure 3-18: Average F-statistic for 5 to 100 simulated flood boundary points for the 4.8k and 1K cms flood scenarios. [4.8K is red, 1K is blue] The dashed lines show the upper and lower bounds for the minimum and maximum F-Statistic from 100 simulations for each point set, and the interior colored regions show the inner quartiles. These results show that for even a small number of boundary points, a reasonable inundation extent estimate can be derived. This range in inputs corresponds to an analyst input of one point per stream kilometer or less.

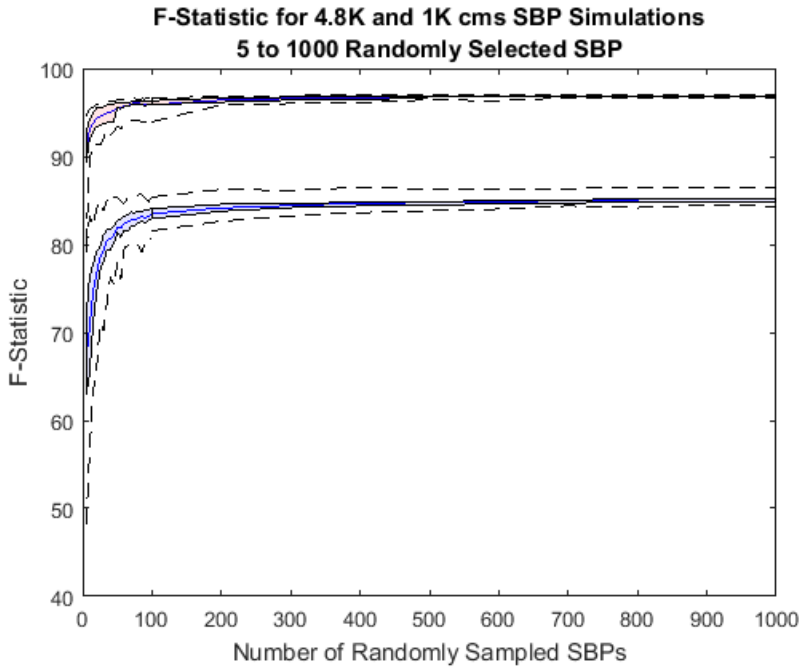

Figure 3-19: [4.8K is red, 1K is blue] Average F-statistic for 5 to 1000 simulated flood boundary points for the 4.8k and 1K cms flood scenarios. The data a above show rapid diminishing improvement in flood extent estimation as points are added. [4.8K is red, 1K is blue]- The 4.8K flood exhibits less sensitivity to inputs than the 1K flood. This property can be explained examine the number of unique FSPs for each scenario. For the 4.8K, there are 169 unique FSPs that are linked to the FPPs, and 690 unique FSPs for the 1K. Figures 3-18 though 3-20 show that as more SBPs are added, an increasing number of points refine the mean DTF value of the FSP they are linked to rather than map to new points along the FSP profile. These data show that, for the manual imagery boundary point input, there would be little benefit to adding more than approximately 100 boundary points in these scenarios. It is interesting to note that for the larger flood, better results can be achieved overall, and fewer points are required to approach the accuracy limit.

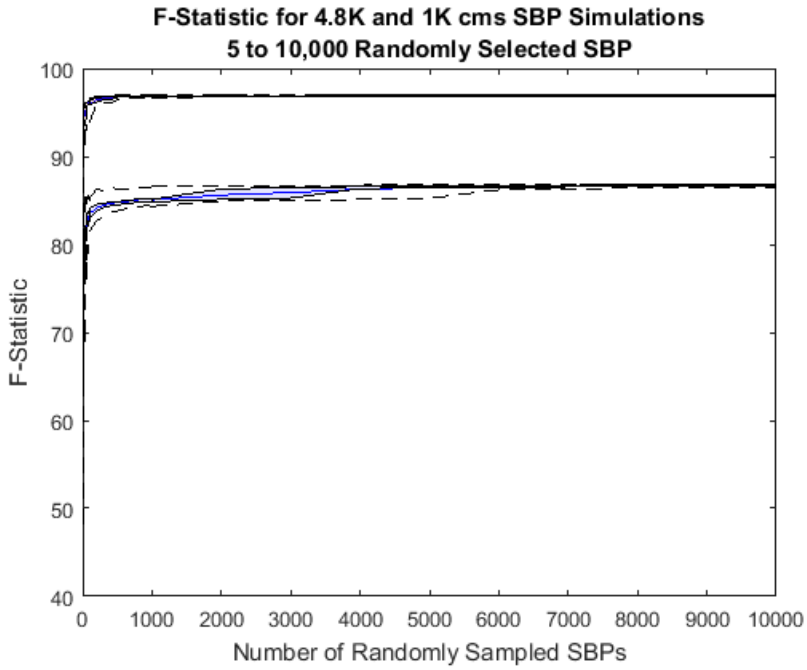

Figure 3-20: [4.8K is red, 1K is blue] Average F-statistic for 5 to 10,000 simulated flood boundary points for the 4.8k and 1K cms flood scenarios. Both the 4.8K and 1K curves exhibit clear asymptotic behavior. The 4.8K flood converges to and F-statistic of 96.9 and the 1K to 86.7. Understanding this baseline behavior for simulated boundary point is important to design of future research. These data will also be a valuable tool for interpretation of results where positional accuracy, resolution, and other variable factors will be important to understand.

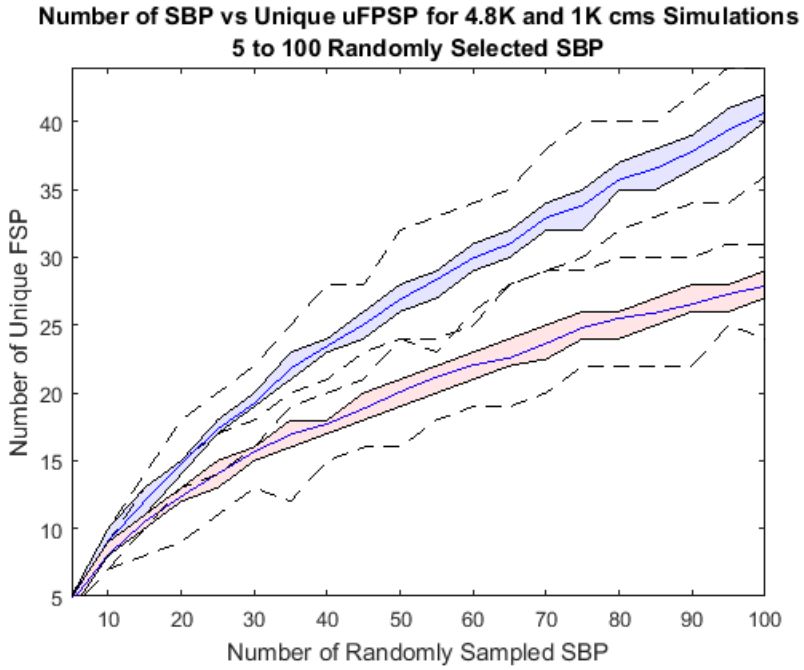

Figure 3-21: Number of unique FSP vs the number random SBPs selected. [4.8K is red, 1K is blue] This illustrates that multiple SBPs relate back to the same FSP.

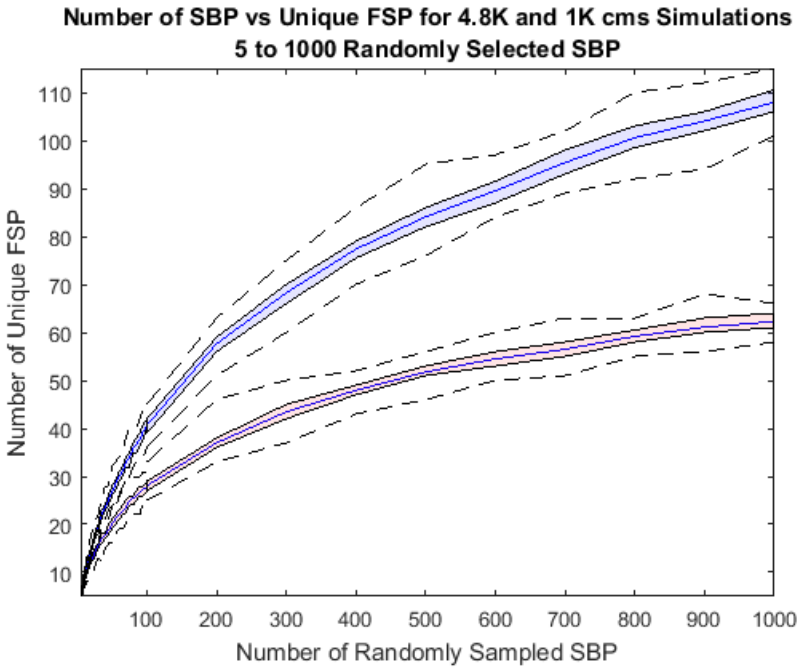

Figure 3-22: [4.8K is red, 1K is blue] The trend in shown in Figure 3-18 continues above.

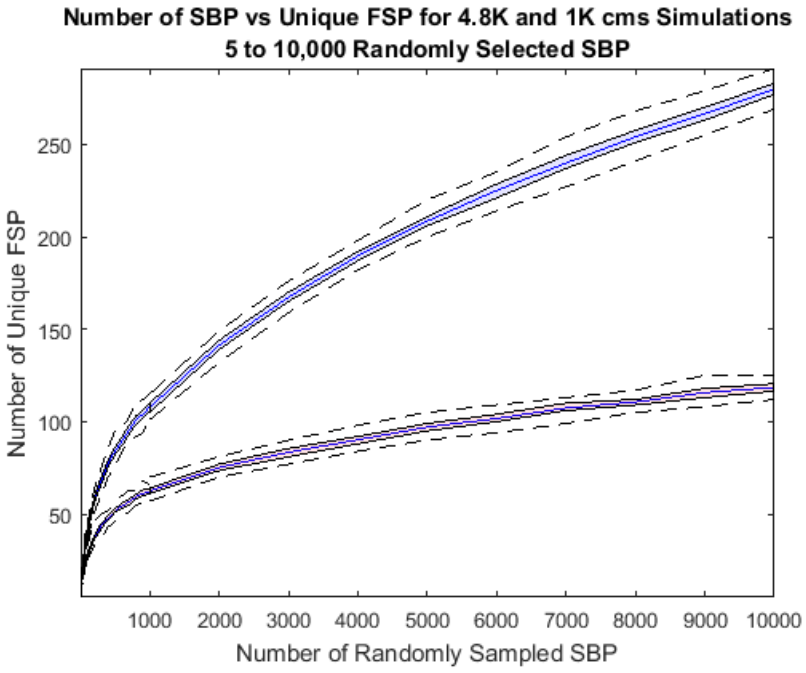

Figure 3-23: [4.8K is red, 1K is blue] There are 44,363 and 158,357 SBPs for the 4.8K and 1K scenarios, respectively. The curves above are trending toward the upper bound of 169 and 690 unique FSPs that exist for the respective flood scenarios. The distribution of the number of FPPs that map to FSPs is not even, which is also reflected in these data.

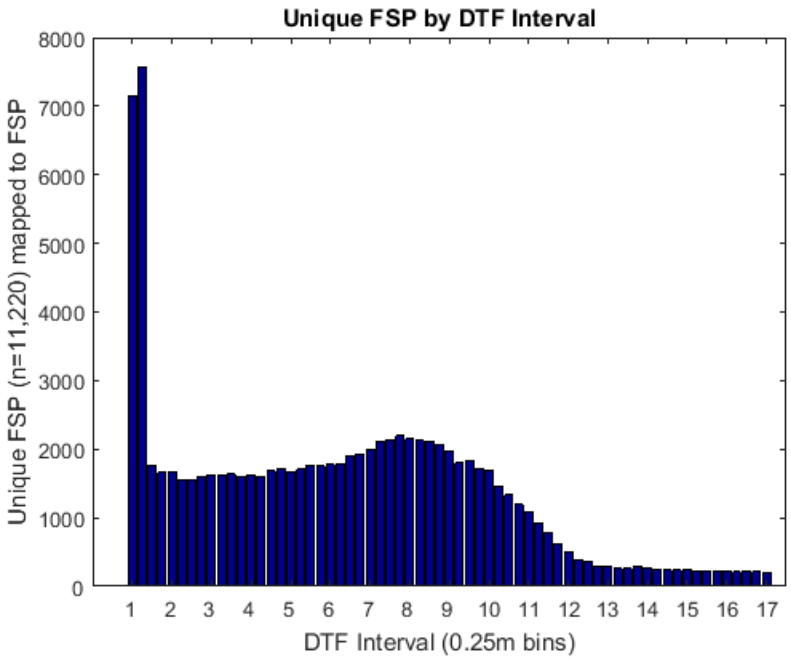

Figure 3-24: This chart shows the distribution of unique FSPs associated with FPP pixels at 0.25m intervals for all FPPs in the Verdigris refined study area. For the 4.8K and 1K SBP sets, there were 169 and 690 unique FSPs among the 44,363 and 158,357 SBP, respectively. Figure 3-22 shows the distribution of their respective DTF values.

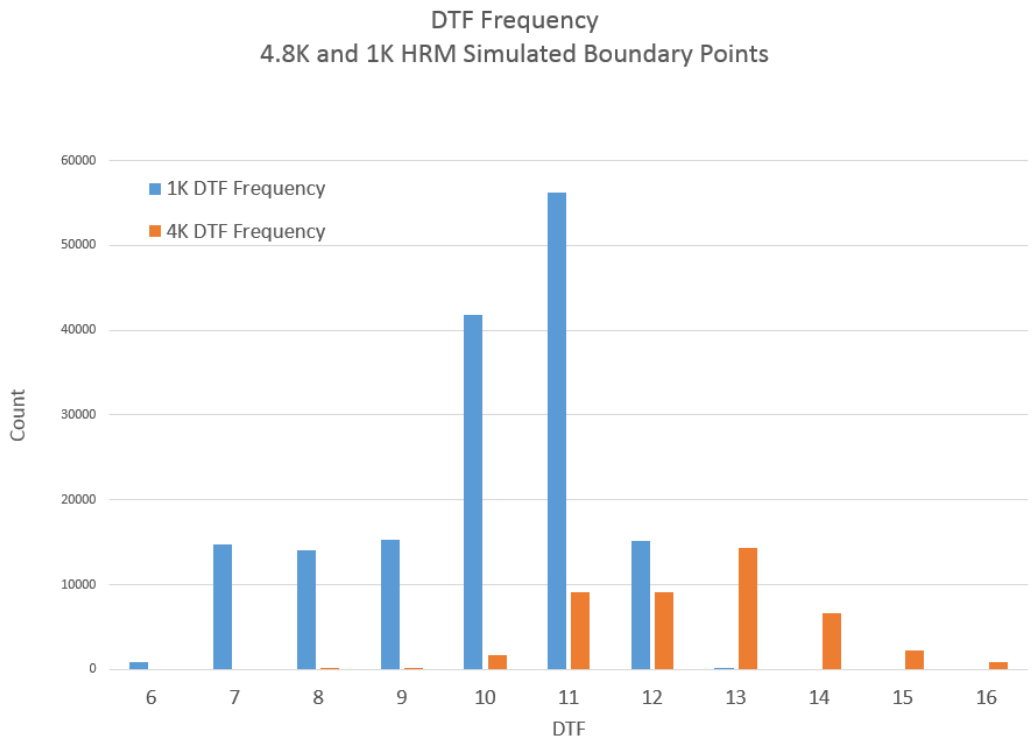

Figure 3-25: For the 4.8K and 1K SBP sets, there were 44,363 and 158,357 SBPs, respectively. The 4.8K points exhibit a normal distribution. The point distribution of the 1K DTF values does not exhibit normal distribution characteristics. The sharp cutoff below 7m occurs because, for this stretch of the Verdigris river, overbank flow does not generally occur below approximately 6m. Finer binning of the data reveals additional characterization and anomalies, but investigation of these is beyond the scope of the present study.

References Cited

Abdullah, Q. A. (2016). A Star is Born: The State of New Lidar Technologies. *Photogrammetric Engineering & Remote Sensing, 82*(5), 307-312. doi:10.14358/PERS.82.5.307

Bates, P. D., & De Roo, A. P. J. (2000). A simple raster-based model for flood inundation simulation. *Journal of Hydrology, 236*(1-2), 54-77.

Becek, K., & Becek, K. Evaluation of Vertical Accuracy of the WorldDEM™ Using the Runway Method. *Remote sensing (Basel, Switzerland), 8*(11), 934. doi:10.3390/rs8110934

Capitol, S. t. (2016, 2016/06/03/). New Remote Sensing Findings from University of Minnesota Described [An automated, open-source pipeline for mass production of digital elevation models (DEMs) from very-high-resolution commercial stereo satellite imagery], Article. *Skirting the Capitol,* p. 1904. Retrieved from http://go.galegroup.com.www2.lib.ku.edu/ps/i.do?p=EAIM&sw=w&u=ksstate_ukans&v=2.1&it=r&id=GALE%7CA453716187&asid=ec95f9bd9f5b2944d72b0d3d503ecc84

Cook, A., & Merwade, V. (2009b). Effect of topographic data, geometric configuration and modeling approach on flood inundation mapping. *Journal of Hydrology, 377*(1/2), 131-142.

Coveney, S. (2013). Land Cover Dependent Error in Intermap IFSAR DTM. *Photogrammetric Engineering & Remote Sensing, 79*(3), 277-286. doi:10.14358/PERS.79.3.277

Coxon, G., Freer, J., Westerberg, I. K., Wagener, T., Woods, R., & Smith, P. J. (2015). A novel framework for discharge uncertainty quantification applied to 500 UK gauging stations. *Water Resources Research, 51*(7), 5531-5546. doi:10.1002/2014WR016532

Di Baldassarre, G., Schumann, G., & Bates, P. (2009). Near real time satellite imagery to support and verify timely flood modelling. *Hydrological Processes, 23*(5), 799-803. doi:10.1002/hyp.7229

Graham, R., & Koh, A. (2002). Digital Aerial Survey - Theory and Practice: Whittles Publishing.

Grimaldi, S., Li, Y., Pauwels, V. R. N., & Walker, J. P. (2016). Remote Sensing-Derived Water Extent and Level to Constrain Hydraulic Flood Forecasting Models: Opportunities and Challenges. *Surveys in Geophysics, 37*(5), 977-1034. doi:10.1007/s10712-016-9378-y

Horritt, M. S., & Bates, P. D. (2001). Effects of spatial resolution on a raster based model of flood flow. *Journal of Hydrology, 253*(1-4), 239-249.

InterMap. (2017). InterMap Data. Retrieved from http://www.intermap.com/data

Kastens, J. H. (2008). *Some New Devolopments On Two Separate Topoics: Statistical Cross Validation and Floodplain Mapping.* (Mathematics Dissertation), The University of Kansas, Lawrence.

Mallet, C., & Bretar, F. (2009). Full-waveform topographic lidar: State-of-the-art. *ISPRS Journal of Photogrammetry and Remote Sensing, 64*(1), 1-16. doi:http://dx.doi.org/10.1016/j.isprsjprs.2008.09.007

NGA. (2015). NGA, Germany's Bundeswehr Geoinformation Centre sign geospatial data sharing agreement. Retrieved from https://www.nga.mil/MediaRoom/News/Pages/NGA,-Germany%E2%80%99s-Bundeswehr-Geoinformation-Centre-sign-geospatial-data-sharing-agreement-.aspx

Noh, M.-J. (2015). Automated stereo-photogrammetric DEM generation at high latitudes: Surface Extraction with TIN-based Search-space Minimization (SETSM) validation and demonstration over glaciated regions. *GIScience and remote sensing, 52*(2), 198-217. doi:10.1080/15481603.2015.1008621

Peterson, D. L., Whistler, J. L., Lomas, J. M., Dobbs, K. E., Jakubauskas, M. E., Egbert, S. E., & Martinko, E. A. (2008). *2005 Kansas Land Cover Patterns Phase I: Final Report*. Retrieved from

Riegler, G., & Riegler, G. (2015). WORLDDEM – A NOVEL GLOBAL FOUNDATION LAYER. *ISPRS - International Archives of the Photogrammetry, Remote Sensing and Spatial Information Sciences, XL-3/W2*, 183-187. doi:10.5194/isprsarchives-XL-3-W2-183-2015

Schumann, G., Hostache, R., Puech, C., Hoffmann, L., Matgen, P., Pappenberger, F., & Pfister, L. (2007). High-Resolution 3-D Flood Information From Radar Imagery for Flood Hazard Management. *IEEE Transactions on Geoscience and Remote Sensing, 45*(6), 1715-1725. doi:10.1109/TGRS.2006.888103

Tayefi, V., Lane, S. N., Hardy, R. J., & Yu, D. (2007). A comparison of one- and two-dimensional approaches to modelling flood inundation over complex upland floodplains. *Hydrological Processes, 21*(23), 3190-3202.

USGS. (2017). Interferometric Synthetic Aperture Radar (IFSAR) Alaska. Retrieved from https://lta.cr.usgs.gov/IFSAR_Alaska

CHAPTER 4

PROFILING FLDPLN MODEL CODE FOR INSIGHTS INTO COMPUTATIONAL PERFORMANCE

Abstract

For small geographic areas, geocomputation processing time and computational efficiency are often not the focus of research efforts when the development and testing of new applied research methods is the driving motivation. When scaling to larger geographic areas, there may arise a need to evaluate the computational performance of workflows and software that has been developed to determine if it can be utilized efficiently, or at least practically, in a way that supports application to larger datasets and more complex problems. The FPLPLN model, developed at Kansas Applied Remote Sensing Program, has been used for the creation of flood inundation libraries for disaster response and ecological applications at local and regional scales. To establish time and computation resource requirements for wider area flood library production, this paper profiles the computational cost of the FLDPLN model when applied to typical sets of input terrain data in Kansas. Results show that for sets of 195 and 945 stream segments, with maximum segments lengths of 5 miles and 1 mile, respectively, there was considerable variability in processing times over a range of flood depth iterations. Explanatory insights related to landscape level morphology of the floodplain are examined. Ideas for potential strategies for improved performance and considerations for scalability in a distributed computational environment (high performance computing) are also explored.

Terms and Abbreviations

[ACF] Advanced Computing Facility: a high-performance computing cluster at the University of Kansas.

[AMSR-E and AMSR-2] Advanced Microwave Scanning Radiometer: Japanese satellites that collect passive microwave radiation.

[CREST] Coupled Routing Excess Storage: hydrologic model developed at the University of Oklahoma.

[DDP] Distributed Desktop Production: used in the paper to describe a multi-machine, non-HPC (High-performance computing) environment for the production of SLIE data.

[DEM] Digital Elevation Model

[DMC] Disaster Monitoring Constellation: Algerian, Nigerian, Turkish, British and Chinese government sponsored collection of remote sensing satellites for disaster readiness, response, and recovery.

[DTF] Depth to flood: the output of the FLDPLN model developed by Kastens (2008) relating the minimum flood depth required to inundate a non-stream pixel from a reference stream pixel. In some circumstances the DTF can be used as a proxy for stage.

[FAC]Flow Accumulation layer: raster data derivative of DEM data with catchment area calculated for every cell.

[**FLDPLN**] FLDPLN model used to derive a segmented library of inundation extents (SLIE).

[FPP] Floodplain pixel: pixels flooded from FSPs at a given flood depth (DTF).

[FSP] Flood source pixel: stream pixels derived from a DEM-derived synthetic stream network, utilized by the FLDPN model to determine relative height above the stream.

[GFDS] Global Flood Detection System: global, daily flood layer derived from passive microwave satellite remote sensing data.

[HPC] High-performance computing

[LISFLOOD-FP] "LISFLOOD-FP is a two-dimensional hydrodynamic model specifically designed to simulate floodplain inundation in a computationally efficient manner over complex topography."

[LTP] Longest Processing Time: job scheduling approach used for optimization of job sets that are run on multiple machines simultaneously. With LPT, longest running jobs are submitted for processing in descending order of expected runtime.

[MODIS] Moderate Resolution Imaging Spectrometer: global moderate resolution multispectral instruments aboard the Terra and Aqua satellite platforms.

[MrGeo] "MrGeo is a geospatial toolkit designed to provide raster-based geospatial capabilities that can be performed at scale. MrGeo is built upon

Apache Spark and the Hadoop ecosystem to leverage the storage and processing of hundreds of commodity computers."

[NASA] National Aeronautics and Space Administration

[NED] National Elevation Dataset: US DEM dataset maintained by the USGS

[NIR] Near infrared: spectral band located between red and middle infrared wavelengths that is readily absorbed by water and is useful for identifying flooded are in remotely sensed imagery.

[PARFEVAL] Parallel for-loop function in MATLAB

[PARFOR] Parallel for-loop function in MATLAB

[PBS] Portable Batch Scripts: script used to submit parallel jobs to an HPC cluster.

[SLIE] Segmented library of inundation extents: database of outputs from running of the University of Kansas FLDPLN model.

[SWOT] Surface Water Ocean Topography: Joint US, French, and Canadian satellite mission slated for Launch in 2021.

[TRMM] Tropical Rainfall Measuring Mission: Joint US and Japanese satellite mission to estimate global rainfall, which operated from 1997-2015.

[UAS] Unmanned Aerial System: also known as unmanned aerial vehicles (UAV) or "drones."

[USGS] United States Geological Survey

[Walltime] Wallclock time: used in PBS batch scripts to request allocation of compute resources on an HPC cluster.

[Workers] MATLAB terminology for an available CPU cores. A dual quad core machine, for example, has the potential for 8 workers.

Introduction

New methods are needed to provide timely information to disaster managers. As advances in production of high quality digital elevation models (DEM) are rapidly evolving, and satellite and aerial remote imagery for disaster response is becoming more widely available at increased temporal frequency, development of new approaches to flood mapping are possible. One approach that is in development at the University of Kansas uses segmented libraries of inundation extents (SLIE) generated with the FLDPLN model (Kastens, 2008). Gage-based applications for rapid flood inundation mapping have been developed using this approach (Dobbs, 2010), and other applications are under active development. Figure 4-1 gives an overview of the conceptual framework for FLDPLN model inputs, execution, and applications. One key finding of the application development to date has been the need to develop SLIE libraries over wide areas well in advance of the occurrence of the disasters for which they will be utilized. Ideally, to better enable the development of the applications outlined in the conceptual framework, some of which are described below, an optimized workflow for wide-area SLIE production, at continental to global scales, is needed.

Applications, for example, would include integration with flood maps derived from MODIS satellite imagery that are produced by the Dartmouth Flood Observatory (Brakenridge & Anderson, 2006), and the MODIS NRT (near real-time) product produced by NASA (Davies et al., 2015; Murphy et al., 2015; Policelli et al., 2017). These datasets could be linked with SLIE data to refine the

250m MODIS flood information. The coarse resolution of the MODIS data gives a valuable overview of major floods for much of the planet. It may be possible to take these data for a given river reach and overlay them on a continuous SLIE representation for the same reach. By examining the distribution of DTF values that are flooded along the floodplain, an "envelope" of maximum DTF values might be identified that could be used to develop a more accurate DTF profile. This profile could be used to construct a custom flood extent map that would better represent the flood than the MODIS data alone, and that accurately reflects the terrain that is represented in the DEM.

The Global Flood Detection System (GFDS) generates daily flood monitoring data for the entire planet (De Groeve, 2010). This information is derived from passive microwave remote sensing data such as TRMM, AMSR-E, and AMSR-2 (Awadallah & Tabet, 2015). These data, however, are relatively coarse resolution compared to other remote sensing data, with roughly 10km pixel resolution. Because the GFDS also produces a water surface area estimate for the set of pixels that it monitors, it should be possible to link these water surface area estimates with an appropriate SLIE derived flood map for the same area. In theory, if the elements from the SLIE database are chosen that match the flooded area estimate, the SLIE maps should give a much more spatially explicit representation of the flood. This could be used to produce better population impact estimates, affected infrastructure estimates, and improved situational awareness, particularly in areas that do not have dense stream gage networks.

The NASA/CNES/CSA/UKSA surface water and ocean topography mission (SWOT) is scheduled to be operational in 2020. The mission is defined as follows: "SWOT aims to provide water level records for any flooding events that underlay a given satellite overpass. SWOT scientists will also be able to look at synergistic combinations of SWOT and other satellite datasets, modeling, and in situ observations to improve capabilities (NASA, 2017)." SWOT will use K_a-band SAR interferometry to determine water surface elevations on rivers greater than 100 m in width to a vertical accuracy of better than 10cm (Prigent, Lettenmaier, Aires, & Papa, 2016). Although it will have a 22 day repeat cycle, in theory this it an ideal input dataset for linking with prebuilt SLIE data because no discharge information is required to translate these data into accurate flood extent maps. The data contained within the 120-km swath should be sufficient to translate into a DTF profile that can extend the water surface height information to flood inundation.

One of the biggest revolutions in satellite imaging is occurring with the increased number of small satellites with visible and NIR data at resolutions of 3-5m. Planet Labs, with the goal of imaging the entire planet every day at 3-5m resolution, is leading this charge along with a number of other companies. OmniEarth, BlackSky, Skybox, DMC, and others are providing high resolution, multispectral data with temporal frequencies that are continually improving (Dyer & McClelland, 2017; Young, 2015). This will soon yield imagery that is collected on a daily basis, thus capturing unprecedented information about flooding and other disasters (Witjes, Olbrich, & Rebasso, 2017). It may soon be

possible to implement daily updates to SLIE- based inundation extents based of these data.

Unmanned Aerial Systems (UAS) are rapidly evolving, including platforms, sensors mounted on those platforms, applications, and the legal framework for operation. I envision that in the near future a UAS could be programmed to follow a river course and collect imagery or other data that could be used to derive the water surface elevation at various points along the stream. This might be done by collecting nadir-looking imagery that includes flood boundary points. Precise registration of the imagery would be key, but there are relatively straightforward methods to quickly and accurately do this. Flood boundary points could then be extracted to inform the creation of custom flood extents maps. This approach has the advantage that the UAS could fly under clouds (Gomez & Purdie, 2016) (Yuan, Liu, & Zhang, 2017).

Also, as Bates and De Roo have done with the development of the LISFLOOD-FP model, it may be possible to couple the output of other models in a cascaded modeling framework to serve as an input for SLIE flood mapping (Grimaldi et al., 2016). LISFLOOD-FP uses a coupled 1D kinematic wave propagation component along with a 2D diffusive wave propagation component to map floods, with discharge at a known location as the primary input (Bates & De Roo, 2000). Applications of the SLIE could also be developed using similar techniques, with the SLIE serving as the diffusive wave propagation component, as long as reasonable water surface elevations could be drawn from the kinematic wave component. It might also be possible to couple with a hydrologic model

like CREST (Coupled Routing and Excess STorage) to achieve similar results (Xue et al., 2013). These types of approaches would be useful where gage data and imagery are not available, or for near-term forecasting.

Collectively, these application areas offer great potential for avenues of research for the FLDPLN model. One of the key benefits of the FLDPLN model's utility also presents a challenge. For disaster response and near real-time flood inundation mapping, the output of the model needs to have been derived well in advance. Because the model does not require complex, upfront parameterization, this means that nothing needs to be known *a-priori* about the scenarios for which it will be applied. What this means is that the model needs to be run in advance for every location it might be needed, and it also means that it can be run in advance for every location it might be needed. Scaling the production of the model output, then, becomes an important factor of application development and implementation. The focus of this study is to understand the computational cost and computational characteristics of the FLDPLN model as it is currently implemented in order to better position future research pathways that can leverage the emerging opportunities outlined above.

FLDPLN model research and development efforts

Since its inception over ten years ago, the FLDPLN model has been used for a wide variety of applications, including flood disaster response, historic flood reconstruction, ecological applications, and more (Bhatt et al., 2016; Dobbs, 2010; Kastens, 2008; Williams et al., 2013). Gage datasets have formed the foundation of many of the SLIE applications to date. It was used at for the Little

Osage pilot study, for several other studies, my master's thesis work(Dobbs, 2010), and for current implementations of the SLIE data in collaboration with Riverside Technology Inc. High water mark (HWM) data, often surveyed and recorded after major floods, are another application, particularly for historic flood reconstructions like the one that was performed for the 1938 flood reconstruction along Brady Creek and the San Saba River in Texas using the FLDPLN model (Kastens, Dobbs, & Luna, 2010). The advantage to this approach is that it fits a DTF profile to observed data with no need to estimate discharge. Preliminary examination of the HWM data from a flood event in Montgomery County, KS in 2007 indicates that there may be some outliers in HWM data that are caused by local effects from obstruction, but these data need to be examined more closely (Dobbs, 2010). Indications from Texas water authorities are that there is a very large HWM database that could be exploited to provide historic context for flood vulnerability in communities across that state. It is likely that these data are also available (or at least in existence) more widely.

While much ancillary code has been developed to support these applications, the core of the FLDPLN model, as described by Kastens in 2008, has remained largely unchanged. The basis for the disaster response applications for the FLDPLN model depend on preprocessing all potentially affected areas. Even modeling of the gaged stream network in the US covers over 150,000 stream miles (Figure 4-2), while the full National Hydrography Dataset covers over 7.5 million miles of streams. While improvements in computational capacity and memory may not require that improvements in the computational efficiency

of the model code be made, being able to effectively estimate the computational time, computing and storage resources, and financial cost of developing the SLIE databases at continental or global scales is necessary to support applications research and SLIE development. With these goals in mind the following objective will be addressed in this study.

Objective

This study profiles the FLDPLN model code to characterize computational performance. The model code performance is profiled by measuring computation time and key variable size over the range of flood depth iterations for each stream segment in several test datasets.

Study Area and Data

The study area covers 11,455 km^2 of the Verdigris and Caney River watersheds in southeast Kansas (Figure 4-3), or about 5.4% of the land area of Kansas. This area covers all or most of Montgomery, Wilson, Chautauqua, Elk, and Greenwood counties, and smaller portions of Cowley, Butler, Chase, Lyon Woodson, Neosho, and Labette counties. This area of Kansas receives from 32 to 39 inches of precipitation annually, with moderate seasonal flooding in the spring and summer months. In 2007, all the counties in the study area experienced major flooding in late June and early July. It was this event that spurred the development of flood mapping applications using the FLDPLN model. In 2008, with support from the Kansas Water Office, the FLDPLN model was used to develop a

segmented inundation library (SLIE) for this 20-county area using the USGS 10m National Elevation Dataset (NED) that was available at the time.

By 2015, the SLIE for the study area (along with much more of the state) was updated using lidar-derived 5m elevation data. A collaborative effort between federal, state, and local partners over the past decade has yielded high-quality lidar-based terrain data covering the vast majority of Kansas, including the entire Verdigris-Caney study area. The coarsest lidar DEMs have 2m resolution, with a stated vertical accuracy of better than 24cm ce90 across land use classes, though most of the area is covered by 1m lidar DEMs with about twice the vertical accuracy. These data serve as the basis for the FLPLN model analysis for this study.

This study area was chosen for both practical reasons that leverage the DEM pre-processing that has been done for the State of Kansas sponsored SLIE development, and because it is covers a relatively representative sample of the floodplain sizes that occur in the region. Wider floodplains, such as those that occur along major rivers such as the Kansas, Missouri, and Mississippi, to name only a few, present computation challenges that are not addressed in this study, but which will be discussed briefly in later sections.

(Note: metric units are used except where legacy standard FLDPLN processing units are in imperial units, namely miles)

Methods

It may be useful to cast the objective of this study within the context of an automotive analogy as a preface to the methods employed. If the FLDPLN model can be thought of as a vehicle, the intent if this study is to test the performance of the vehicle in a variety of road conditions to characterize its overall performance. It is not the objective to redesign the engine. Hence, the analysis of the underlying algorithm and code of the FLDPLN model is not the focus of this study. That is not to say that there are not performance gains to be made, and it is hoped that the results presented here can lend support to such efforts. In order to evaluate the performance of the FLDPLN model, as written, the following processing and analyses were performed.

FLDPLN Model Performance Profiling

Several different variations, or scenarios, of FLDPLN model parameters are evaluated. The rational for each will be addressed later in the section, but for clarity they are introduced here. These include parallel processing runs of the FLDPLN model using the PARFOR function on stream segment sets with the following parameters:

S1 - 195 segments, 5-mile maximum segment length with 1m DTF increments

S2 - 195 segments, 5-mile maximum segment length with 0.5m DTF increments

S3 - 195 segments, 5-mile maximum segment length with 1m DTF, backfill only

S4 - 945 segments, 1-mile maximum segment length with 1m DTF.

Two additional runs of the S1 scenario were evaluated using the PARFEVAL function, which is also described in more detail below.

All computational cost data described below were collected using a 24-core node (specifically, node #494) on the University of Kansas Advanced Computing Facility (ACF) high performance computing cluster (Figure 4-4). The operating system on the machine is Linux 2.6.32, with twenty-four 2.49 GHz CPUs and 256 GB of RAM. MATLAB version 2016b was used for running the FLDPLN model code. Twenty-four MATLAB workers (available cores) were used for all processing, with no other jobs running on the node while the model code was running. The basic FLDPLN model code, version V3HD, was used for all processing. This version stores and reads temporary files and input files on disk. While faster versions of the model code that utilize more RAM storage have been developed, the V3HD version is not RAM limited, and therefore is the version that is the least hardware limited. This analysis will also serve as a baseline against which to evaluate the RAM versions of the model code to accurately document performance gains, but that is left to future studies.

For all FPDPLN model runs, lidar-derived DEMs for the study area were downsampled from their native 1m resolution to 5m. This was done to reduce the size of the input DEM while maintaining the vertical accuracy of the lidar data.

The 5m datasets is 4% the size as the 1m dataset, which proportionately reduces the computational cost while maintaining important landscape features and vertical accuracy. The DEMs were processed with the standard fill, flow direction, and flow accumulation DEM hydrologic operations using ArcGIS spatial analyst hydrology tools. Additional DEM conditioning best practices, including breaching of dams and culverts, was performed prior to hydrologic processing to improve hydrologic connectivity accuracy.

For S1, S2, and S3, synthetic streamlines were extracted at the 70 mi^2 flow accumulation threshold, which roughly corresponds with the gaged portion of the stream network in Kansas. Stream segment breaks were installed at all confluences, as well as at other major inflows (25 mi^2), and finally at lesser inflows as needed to impose a maximum segment length of 5 miles. This process yielded 200 stream segments, five of which crossed large reservoirs. Previous work has shown that stream segments that cross reservoirs have exceptionally long processing times, and they also are not useful for riverine flood modeling. These stream segments were removed from the processing list, yielding 195 segments. It should also be noted that these parameters are the same as those used for the Kansas SLIE production mentioned above.

For the S1 scenario, the FLDPLN model was run at 1m DTF height iterations from 1m to 15m. In keeping with the research objective, which is to profile the performance of the FLDPLN model code as it is written, MATLAB code was inserted to record the computational time cost and size of key data variables for each height iteration in the processing:

M1 - Measurement #1 recorded the computation time for each segment at each DTF height iteration.

M2 - Measurement #2 recorded the floodplain pixel (FPP, or the number of inundated pixels) variable size after each DTF height iteration.

M3 - Measurement #3 recorded the inundation boundary size, in pixels, after each DTF height iteration.

For the S2 scenario, to evaluate the effects of iteration height, another run of the same S1 segments was processed at 0.5m change in DTF per iteration with corresponding performance measurements recorded. This produced 30 iterations over 195 segments. The M1, M2, and M3 measurements were recorded for each iteration, as above.

For the S3 scenario, the same parameters were evaluated as in S1, but the spillover step was disabled. This was done to establish the magnitude of the primary backfill component relative to the full steady-state version of the FLDPLN model. This was also done to determine if the backfill-only runtime is strongly correlated with the steady state runtime. Again, all performance measurements were recorded.

For the S4 scenario, to evaluate the effect of stream length on overall processing times, another set of segments was developed with a maximum segment length of one mile. The segments were otherwise prepared as outlined above, which yielded 945 stream segments. The performance measurements were recorded for these segments as well.

Anomalous runtime segment features were examined to determine explanatory causes, including visually to determine if any explanatory landscape-level features could be identified as the cause of longer runtime behavior. These might include wide floodplains, tributaries, or other potential landscape factors. Summary results are reported along with explanatory interpretations. Recommendations for optimization or alternative workflow strategies are offered if applicable.

MATLAB PARFOR vs PARFEVAL

Although not originally part of the planned methods, the code profiling observations revealed insights into the behavior of the MATLAB PARFOR (parallel FOR loop) function. Analysis of this behavior indicated that the PARFEVAL function might yield improved workstation performance. Although it was not immediately known that the PARFEVAL function was the resolution, research into the functionality of the PARFOR loop pointed to the PARFEVAL loop as an alternative for non-internally optimized MATLAB code. To compare the overall efficiencies of these functions, three scenarios were evaluated for overall runtime using the 195 segment, 1m step size dataset:

1) PARFOR loop where the segment IDs are sent to the PARFOR loop in numeric order,

2) PARFEVAL loop where the segment IDs are sent to the PARFOR loop in numeric order, and

3) PARFEVAL loop where longest running segments are sent to PARFEVAL first, in descending order of runtime.

The third scenario was informed by the runtimes collected in the first scenario. More on this will be reviewed in the results section.

Results

The findings below are presented in a way that is designed to offer insights into the range of expected segment and iteration runtimes, and to expose some of the factors that influence trends and outliers, both at the segment and iteration levels. A variety of tables and graphical representations of the data, combined with reference maps, show the key relationships. This is not meant to be an exhaustive examination of the data, but is intended to broaden the understanding of the computational performance of the FLDPLN model, as written, and lay the foundation for future efforts toward wide area SLIE production. This is intended to inform two different production strategies: 1) distributed desktop production (DDP) and 2) distributed high performance computing production (HPC). Most of the model performance insights covered here are useful for both strategies, but specific relevance to each will be provided where appropriate. The DDP is characterized by multiple multi-core machines on an *ad hoc* local network, whereas the HPC environment under consideration is the KU Advanced Computing Facility, which operates a 500-node high-performance computing (HPC) cluster that accepts job submissions via Portable Batch System (PBS) scripts. The key consideration that is the focus of the profiling here is the real-world time, or wall-clock time (walltime), that needs to be specified with

each HPC job submission. This allows the PBS scheduler to allocate the appropriate resources for each job requested. Insufficient walltime requests will result in early job termination. Longer walltime requests receive lower prioritization in the job queue. It is, therefore, advantageous to have a firm understanding of the processing time requirements of the FPDPLN model for individual segments.

The composite 15m DTF map for the study area is shown in Figure 4-5. Note that while the mapped potential floodplain widths vary throughout the study area, upper reaches tend to have narrower floodplain widths. Also, there are a number of areas in Wilson and Montgomery Counties with notably wide floodplain areas, and there are three sizable reservoirs, one each in Woodson, Greenwood, and Montgomery Counties. While close inspection of all the study area is not possible, areas with notable features that affect FLDPLN model processing times are described below.

Scenario S1

The S1 segment set serves as the primary dataset for examination of runtimes and variable sizes for segments across a range of FLDPLN model DTF iterations. While 5 miles is the maximum segment length parameter, Figure 4-6 shows the distribution of FSP segment lengths, in 5m pixels, across all 195 segments. Segment #99 is the largest, with 1597 pixels, segment #177 is the smallest, with just 5 pixels, and the average segment length is 855 pixels.

Summary statistics for the segments runtimes, M1, are given in Table 4-1. Iteration 15 had the longest total processing time when summed across all segments. The initial iteration had the largest total computation time of the first seven iterations. Previous work has shown that this is attributable to the filling of the width of the stream surface within that channel, spreading out from the 1-pixel wide representation of the FSPs within the stream channel. The total iteration processing time totals remained relatively low for iteration 2 through 6, which previous work has also associated with the filling of the stream channel below bankfull depths (and thus limited opportunity for horizontal spreading). The processing time totals jump significantly at DTF iteration 8 and then generally increases though iteration 15. Table 4-2 shows the same statistics, but normalized for stream length. These data, then, present times in terms of cost per FSP. The data follow the same general trends outlined above for the full segment processing times.

For segment runtimes summed across all iterations, segment #175 (319 FSPs) had the longest runtime of 33.98 hours, and segment #31 (343 FSPs) the shortest runtime of 0.53 hours. Figure 4-7 shows that the overall distribution is positively skewed, with a median runtime of 5.88 hours and an average runtime of 7.93 hours. The disparity in runtimes between segments #175 and #31, which are virtually identical in length, suggests that segment runtime cannot be reliably predicted based on segment length. Figure 4-8, which plots segment runtime vs. segment length, lends support to this assertion as there is no discernable relationship between runtime and segment length. In Figure 4-9, which plots

segment runtime against the start of segment FAC value, presents a view that is more informative. Low FAC value segments have smaller catchment size, experience lower flows, and are lower order streams that occur in the upper reaches of the watershed or are small catchments along higher order stream segments. The clustering of low FAC, short runtime segments in the lower left corner of block 'A' in Figure 4-9 represents the upper reaches of low order streams. Examination of the data suggests that the low FAC segments with longer runtimes are those that either connect directly to higher order streams or connect to the floodplains of higher order streams during spillover iterations of the FLPLN model. Blocks 'B' and 'C' correspond with the cluster of long runtime segments surrounding the junction of major tributaries, which is discussed below and is highlighted later in Figure 4-15. Block D corresponds to the Verdigris River segments in Montgomery County between Independence and Coffeyville. The jump in FAC values between block C and D occurs at the junction of the Elk River and Verdigris River just to the northeast of Independence.

Because the segment lengths vary substantially, it is useful to normalize the runtimes by dividing these values by the number of pixels in each segment. The histogram in Figure 4-10 shows that, like the overall segment runtime distribution, the normalized distribution is positively skewed. There is, however, a greater number of outliers in the right tail of the distribution. It should be noted that segment #177 was removed from this and other normalized plots because the extremely short (5 pixel) length of the segment represented such an extreme outlier that the information value of the plots was negatively affected. To

examine the cause of the outliers more closely, the data are presented in a different form in Figure 4-11. Here the normalized runtimes are plotted against segment length. An exponential decay line is included to illustrate the upper envelope of the scatter plot. What this plot shows is that short segments are computationally inefficient compared to longer segments because short segments have a disproportionately longer runtime on a per FSP basis. These data are also presented in a semi-log plot in Figure 4-12, which highlights the fact that the lower bound also follows a similar trend as the upper bound. These results suggest two opportunities to improve the overall computational efficiency: 1) if the normal segmentation process produces segments below a certain threshold, consideration should be given to merging the segment with another adjacent segment; and 2) from a computational efficiency standpoint, the longer the segment, the more computationally efficient it is likely to be. Application, data management, and other considerations may necessitate shorter segmentation strategies, but these findings should be considered during wide area SLIE production planning.

Computing the accumulated M2 measurement across all iterations for each segment, the resulting FPP counts show the relationship between runtimes and the size of the floodplain. Figure 4-13 plots overall FPP set size vs segment runtimes. This plot clearly shows that runtimes are correlated to the size of the floodplain, with an R^2=0.52, but it is not a strong correlation. This suggests that there are other factors that influence segment runtimes, but it is not clear what those factors are. One way to examine this relationship more closely is to plot the increase in

FPP area at each iteration against runtime for the segment iteration, which is shown in Figure 4-14. In addition to exposing iteration-specific information, this increases the number of data points by a factor of 15, to nearly 3000. It is also useful to compare these data alongside the view presented in Figure 4-15, which shows a line plot of the runtime profiles for all segments at each iteration. Outliers in Figure 4-14 are generally those with runtimes of greater than two hours. These same segment iterations are evident in the profile plot.

Explanatory analysis of outliers enumerated Figure 4-15(a) is given through maps, shown in Figures 4-16 and 4-17. Segments #58 and #59, shown in Figure 4-16, lie just upstream of Elk City Lake. The areas mapped in blue correspond to FPPs with low DTF values that would be inundated on the first iteration. The spillover component of the FLPLN model code causes segment #58 to also flood a majority of the area flooded by segment #59, which is why #58 has an even longer runtime. Low, flat, large areas where spillover flooding plays a major part in recruiting new FPPs is a known issue for causing exceptional, disproportionately large runtimes. It is for this reason that lakes and reservoirs are cut from the processing area, and why there is an associated need to minimize the lake level influence on nearby upstream segments. These extreme cases of spillover-dominated iterations suggest that there may be opportunities to improve performance of the model code, though this is beyond the scope of the current study.

The rest of the enumerated outliers in 4-15(a) are mapped in Figure 4-17. Of note is segment #177, the segment that was removed from the normalized plots

above. This segment is positioned between upstream #176 and downstream #178. From upstream to downstream, the overall segment runtimes are 32.7, 29.5, and 29.3 hours, with respective segment lengths of 1533, 5, and 1316 pixels. This again illustrates the point made above, that short segments can be grossly computationally inefficient. Figure 4-15(a) shows that the lower mainstem Verdigris segments, #178-181, spike at the 8m DTF iteration, as do segments #63 and #66, which are tributaries to those segments. Segments #176 and #177, which are directly upstream of segment #178, spike at the 11m DTF iteration. Segments #174 and #175, which are upstream of those, spike at the 14m DTF iteration. The sequencing and magnitude of the anomalies suggest that this occurs when the model spills into a wide floodplain area that is not hydrologically accessible (via FLDPLN model mechanisms) at a lower DTF iteration. This scenario explains why the downstream segments spike at lower DTF iterations, and may also indicate why segments that spill into the area at higher DTF levels require more computation time to fill the area with spillover flooding to the higher DTF level.

The outliers enumerated in the normalized profiles of Figure 4-15(b) are examined in the map shown in Figure 4-18. In all cases, these are extremely short segments with lengths of 31, 29, 71 for segments 154, 156, and 160, respectively. While the overall runtimes for these segments are not remarkable, running 10.27, 8.81, and 13.36 hours, respectively, the per FSP times are quite high. This, again, leads to the recommendation that these short segments be appended to a neighboring segment before being processed by the model.

The FPP boundary sizes (measurement M3) for each iteration are shown in Figure 4-19. This plot closely mirrors the behavior of the increase in FPP area size. When FPP boundary size is plotted against FPP area on a log-log plot, an interesting feature emerges. In Figure 4-20, this plot is broken out into DTF iterations up to 6m (blue), and those above 6m. The two distinct groupings that emerge largely represent the in-channel group in blue and the overbank group in red. The relatively discontinuous jump in values of both variables is the result of a rapid increase in area and boundary size once flood waters overtop the channel. That this consistently occurs near the 6m DTF may be a feature that can be exploited for applications that benefit from differentiation of in-channel vs. overbank flow. Figure 4-21 plots the changes in boundary size vs segment iteration runtime. One noteworthy characteristic in the plot is the presence of negative values. This might occur when interior islands are subsumed at greater flood depths, or as complex, fractal-like shorelines give way to less complex flood boundaries (e.g. when a levee or the valley wall is reached). The last representation of these data is shown in Figure 4-22, which highlights the negative values in boundary size change by plotting boundary size against boundary size change. This also illustrates the contractions noted above. These features are minor and represent insignificant variations in the data.

Scenario S2

The 0.5m DTF iteration data are presented in Figure 4-21 and Table 4-4. The figure plots the 0.5m DTF iteration runtimes against the 1m runtimes. The primary finding is that it takes approximately 1.63 times as long to process

segments to the same maximum depth but with twice as many iterations. Although this correlation is strong, there are a few exceptions where the half-meter processing was faster overall, illustrated by the six segments that lie below the 'break even' threshold shown in Figure 4-23. The most notable of these is segments #58, which took 22.1 hours to process at the 1m DTF increment, but took only 11.5 hours to process at the half-meter. This and the other five segments that showed improved performance are all positioned just upstream of reservoirs. It is unclear why this is the case, but given the fact that these segments upstream of reservoirs are prone to exceptionally long runtimes, it would be worthwhile to examine this in more detail in future work. Although it is beyond the scope of this work, determination of a data driven optimization of DTF step size that also preserves model output accuracy should be considered for wide area processing.

Scenario S3

A priori estimation of segment runtimes could inform FLDPLN model workflow development. One way to gain understanding of potential runtimes is to evaluate the computationally less expensive primary backfill step (performed at the beginning of each iteration) of the FLDPLN model to determine the feasibility of using this information to forecast the runtimes of the steady-state model. This was done for all 195 stream segments, the results of which are shown in Figure 4-24. The ratio of steady state runtime to backfill-only runtime ranges from 5.1 to 116.5, with a median value of 22.82 (Figure 4-25). This shows that calculation of initial backfill runtimes costs only about 4% of the overall runtime. If there were

a strong correlation between the corresponding runtimes, it might be useful for identifying long-running segments in advance and allow routing of those segments to more strategically appropriate computer resources, possibly coupled with alternate FLDPLN model versions that could speed processing or better cope with long processing times. These data show that although there is a moderate correlation between backfill-only and steady-state runtimes, it is not strong enough to clearly guide workflow efficiency gains. There may be sufficient correlation at the shorter end of the range useful for ordering of the segment job scheduling, which is covered in greater detail below. For backfill runtimes below 0.25 hours, marked by the red line in the figure, there appears to be a much stronger correlation, with fewer outliers.

Scenario S4

The last run of the FLDPLN model considered in this study is for 945 segments that have a maximum length of 1 mile. The same input stream segments were used for this analysis as in the previous runs, but these have been further subdivided into smaller segments. The distribution of segment lengths is shown in Figure 4-26. Overall, processing of these segments took four times as long (Table 4-4), using 6453 CPU hours compared to 1547 CPU hours for the 195 segment, 1m step-size set. These data support other findings of this study that show that, when considering processing time per unit length, shorter segments are less computationally efficient. Although the previous specific segments that were examined were few and exceptionally short compared with the average segment lengths, comparing the 945 segment runtimes to the 195 segment results shows

the inverse relationship between processing time per unit length and segment length to be a general property of the FLDPLN model. Figures 4-27 and 4-28, mirroring Figures 4-11 and 4-12 above, show the segment length normalized runtimes for all 945 segments. These finding again suggest that careful consideration should be paid to the selection of the maximum segment length, with longer segments being favored over short segments, unless there are computational or application justifications that would necessitate otherwise.

MATLAB PARFOR vs PARFEVAL

The initial intent of this study did not include an examination and comparison of the PARFOR and PARFEVAL looping functions of MATLAB. Observation of the CPU resource usage of the processing node indicated a long tail of declining CPU usage (in a stair-step fashion) at the conclusion of the initial processing run. This apparent inefficiency prompted a closer examination of how MATLAB implements PARFOR. There is little published on the internal workings of the PARFOR function, but Sharma and Martin (2009) give a sufficient explanation that indicates that the function allocates jobs using index blocks, not new jobs for each element of the index (Figure 4-29). What this means for processing of the FLDPLN model in a workstation environment is that if there is no *a priori* knowledge of processing runtimes, some PARFOR allocations of segment blocks might clump multiple long-runtime segments into the same block. Because PARFOR locks all workers until the processing is complete for every worker, and the FLDPLN model does not utilize parallel optimization within its code, workers that have completed their job lists sit idle

until the end of the processing run. The PARFEVAL function, on the other hand, functions like a simple job scheduler, running the next segment in the index as soon as a worker is available. In addition, this function runs all jobs in the background, so it does not lock down unutilized workers.

To enable comparison of the PARFOR vs the PARFEVAL functions, the 195-segment set was run at the 1m step size using both functions, and overall runtimes were recorded (Table 4-1). The PARFOR processing took 85.7 hours on the 24-core ACF node, while the PARFEVAL took only 71.4 hours, an improvement of 16.7%. One job scheduling theory, the longest processing time (LPT) rule, states that to achieve maximum efficiency, independent jobs run on multiple CPUs should be sequenced from longest to shortest runtimes, if possible (R. L. Graham, 1969). Typically, the FLDPLN segment runtimes are not known *a priori*, but to further evaluate the potential improvements in processing time using the ordered approach, the output from the PARFOR processing times was used to reorder the index used for a second run using the PARFEVAL function. The results of this run show that all jobs were processed in 65.4 hours on the ACF 24-core node. This represents an overall improvement of 23.7% over the PARFOR function. A comparison of the three CPU usage profiles is given in Figure 4-30. The bottom plot shows the PARFOR processing, with an extended right tail as the last blocks of segments are completed. The middle plot shows the use of the unordered PARFEVAL function. The job termination on the right side of the plot is much shorter and smoother. A larger, side-by-side comparison of these two functions is also given in Figure 4-31. The top plot in Figure 4-30

shows the CPU profile of the ordered PARFEVAL function processing. The termination of the processing in that top plot is the sharpest of the three, indicating that MATLAB workers are completing their respective job sequences at nearly the same time, which is the desired effect.

Workflow implementation

Table 4-5 outlines computational resource estimates for processing of the gaged stream network for the continental US, outlined in Figure 4-2. While there are many factors that are not considered in this simple estimation, it serves as a starting point for outlining time and cost estimation for such an undertaking. 1, 6, and 12-month production timelines are offered for comparison for the S1, S2, and S3 FLDPLN model parameterizations considered in this study. DDP workflows have been the primary method of FLDPLN model inundation library production to date. While dedicated DDP offers a conceptually simpler approach, there are advantages to investing in development of HPC workflows. Production of global scale inundation libraries at the 5 to 10-meter DEM resolution scale would require substantial resources and careful consideration of many of the parameters considered above.

Conclusions

The results of this research showed that outliers in computational processing time with the FLDPLN model are tied to flat areas where significant lateral spreading of flood waters would occur with only a small change in water surface elevation. Though this was a known problem for reservoirs,

quantification of the impact on processing time will help guide future efforts to mitigate the issue, which is particularly needed for floodplains along major rivers.

Short segment lengths showed significantly increased processing time per unit length. For very short segments this per unit cost was exceptionally high. Results indicate that long segment lengths are the most efficient. Overall runtimes, however, increase proportionally with segment length. This presents a challenge for job scheduling in the HPC environment where shorter runtimes are desirable, but computational efficiency is also desirable. Implementing a strategy for scaled production of wide area SLIE development in a distributed computing environment with the FLDPLN model code will require a more sophisticated strategy than is within the scope of this study, but the results presented here will help guide that work.

One result that was not anticipated was the discovery that the PARFOR loop in MATLAB is not the most efficient function for management of segment processing in an "embarrassingly parallel" environment. Because the FDPLN model is not written in a way that takes advantage of internal parallelization, the PARFOR loop is acting simply as a job scheduler. Because PARFOR assigns jobs to workers based on blocks of indices, the allocation of which is determined internally and dynamically within MATLAB, this leads to extended runtime for segment processing sets. Use of the PARFEVAL function yielded improved overall performance for segment set processing, though there are not gains or losses in processing time at the segment level.

Use of backfill preprocessing to estimate segment runtime did not show promising results. While for short runtimes the correlation appears to be reasonably good, segments with longer runtime do not appear sufficiently correlated to be useful for runtime estimation. It is possible that backfill runtimes could be used in conjunction with the PARFEVAL function to position potentially longer running jobs toward the front of the job queue for desktop processing. For DDP workflows, quantifying gains in performance by using RAM for temporary file storage should be examined.

Currently the FLDPLN model code is written in the compiled MATLAB language. Porting to C++, or similarly efficient language, is likely to yield significant performance gains (Blas et al., 2016). One other strategy for improving the computational efficiency is to utilize more efficient data structures within the FLPLN model code. Recent work has been done with a similar application for calculation of sea level rise (Li, Grady, & Peterson, 2014). This approach implements a minimum priority queue and compares two approaches, minimum binary heap (min-heap) and Fibonacci heap data structure, to manage the inundation front, which are essentially equivalent to the boundary pixels described above. The authors observed a significant improvement in processing times using both approaches, noting that the min-heap approach yielded a 30x improvement in processing time for the study data. In terms of scalability, a potential way forward would be to take advantage of tiled data managements architectures, such as MrGeo (Giachetta, 2015), to handle sub-setting and scaling. This would also address fundamental challenges with subsetting the input data to

include only the data needed for the processing of the current segment. This would, however, require a significant level of effort and a fundamental rearchitecting of the model itself.

Tables

Table 4-1: Segment processing time statistics for 5-mile maximum, 195 segments scenario. Note: highlighted column time units are in hours, others are in seconds.

Processsing Time per Segment				
Iteration	**Total (h)**	**Max (h)**	**Min (s)**	**Median (s)**
1	107.53	18.88	8.99	298
2	18.90	1.97	9.28	168
3	27.31	2.02	10.69	216
4	36.08	2.04	26.65	286
5	36.46	1.31	29.73	407
6	52.74	2.63	35.99	517
7	76.84	4.00	75.69	753
8	116.56	7.53	100.76	911
9	126.03	5.43	110.59	1272
10	122.64	3.87	67.51	1613
11	134.70	11.03	100.90	1549
12	137.93	5.19	149.85	1865
13	154.97	5.31	135.44	1666
14	178.43	11.78	173.55	2008
15	211.20	5.77	169.24	2308

Table 4-2: Segment processing time statistics for 5-mile maximum, 195 segments scenario, normalized by segment length. Results show times per FSP. Time units are in seconds.

Processing Time Normalized by Segment Length				
Iteration	**Total (s)**	**Max (s)**	**Min (s)**	**Median (s)**
1	261.74	45.96	0.01	0.20
2	46.01	4.79	0.01	0.11
3	66.48	4.91	0.01	0.15
4	87.82	4.96	0.02	0.19
5	88.75	3.19	0.02	0.28
6	128.38	6.39	0.02	0.35
7	187.02	9.74	0.05	0.51
8	283.71	18.32	0.07	0.62
9	306.75	13.22	0.07	0.86
10	298.52	9.42	0.05	1.09
11	327.86	26.84	0.07	1.05
12	335.73	12.63	0.10	1.26
13	377.20	12.92	0.09	1.13
14	434.32	28.67	0.12	1.36
15	514.07	14.05	0.11	1.56

Table 4-3: Overall runtime on 24 cores. A limitation of the PARFOR loop is that job lists are determined internally up-front, leaving workers idle that complete their job lists until completion of all processes. The PARFEVAL loop, on the other hand, continues to assign jobs to workers until no jobs remain. Figure 4-30 shows the CPU activity profiles of each scenario.

Function	Runtime (h)	Decrease
parfor	85.7	0.0
parfeval	71.4	16.7%
parfeval (ordered)	65.4	23.7%

Table 4-4: Computation costs of three FLDPLN model scenarios in the study area.

	Segs	CPU Sec	CPU Hrs	Hrs/core	Hrs/mile
5 Mile Max, dh = 1.0m	195	5,567,672	1546.6	64.4	2.5
5 Mile Max, dh = 0.5m	195	9,071,003	2519.7	105.0	4.1
1 Mile Max, dh = 1.0m	945	22,150,980	6153.1	256.4	10.1

Table 4-5: Simple extrapolation of computation costs from the study area to a Continental US (CONUS) input dataset of the same 5m resolution. This is offered as a rough estimate that is certainly on the low end of what would be required. The inclusion of large rivers with wide floodplains would increase computation costs substantially. CPU specifications, max stream length, iteration height (DTF step size), and other factors could significantly alter these figures. Data preparation is not factored into these calculations. In order to cover the full National Hydrography Dataset (NHD) that is being supported by the National Water Center, at 7.5 million stream miles, one would multiply these estimates by 50.

	est. CONUS Hrs	Years(1-core)	1 Month	6 Month	12 Month
			# Cores	# Cores	# Cores
5 Mile Max, dh = 1.0m	380,305	43	521	87	43
5 Mile Max, dh = 0.5m	619,604	71	849	141	71
1 Mile Max, dh = 1.0m	1,513,045	173	2073	345	173

Figures

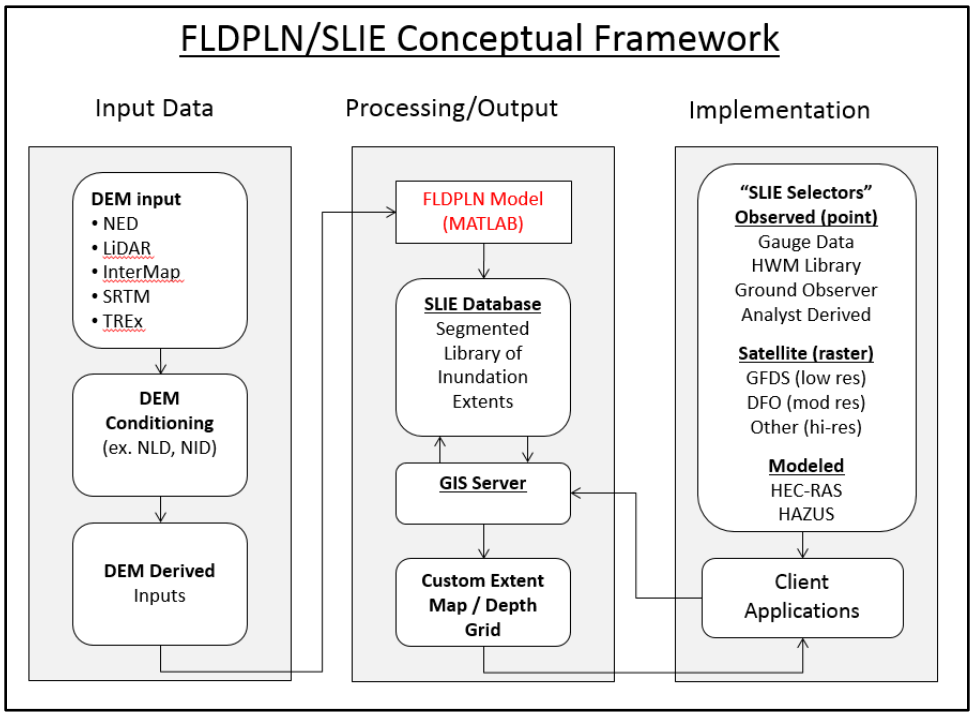

Figure 4-1: Workflow and conceptual diagram for operational implementation of the FLDPLN model. Red text indicates the focus of the current work. Although the focus is on the production of SLIE databases, the motivation is to support application development in the implementation column.

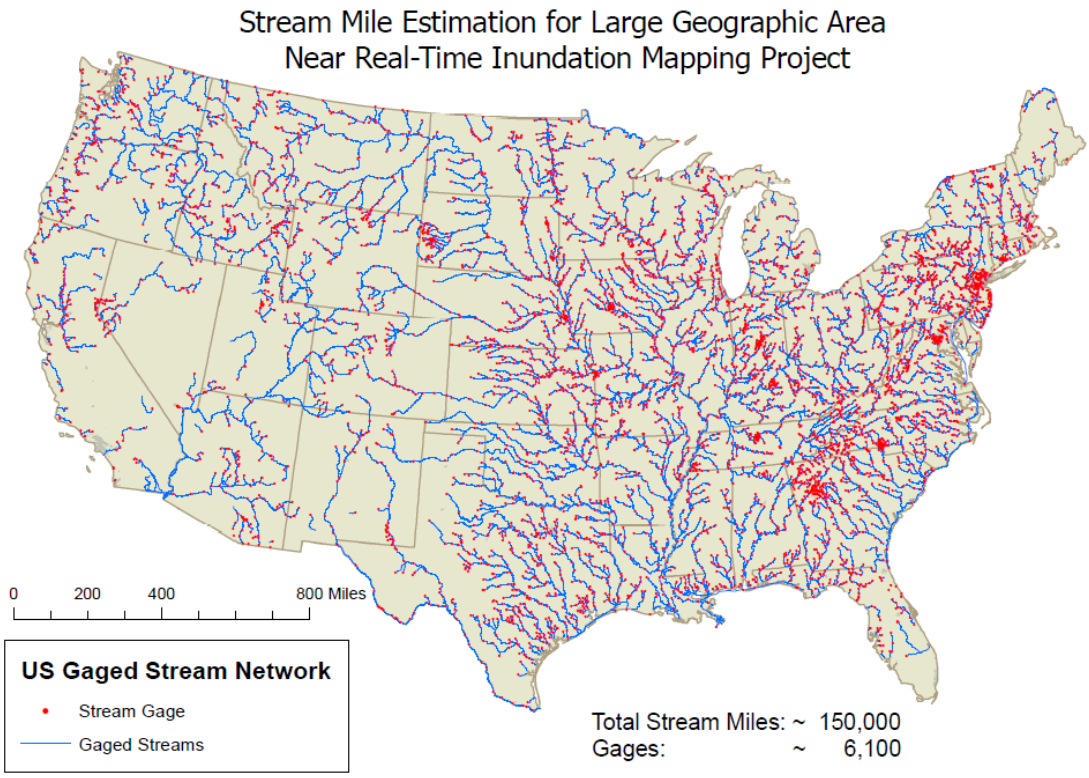

Figure 4-2: Estimated gaged stream network in the continental US. While this estimate was developed to support estimates of gage-based application SLIE production estimates, the full National Hydrology Dataset (NHD) covers 7.5 million stream miles, or 50 times this estimate.

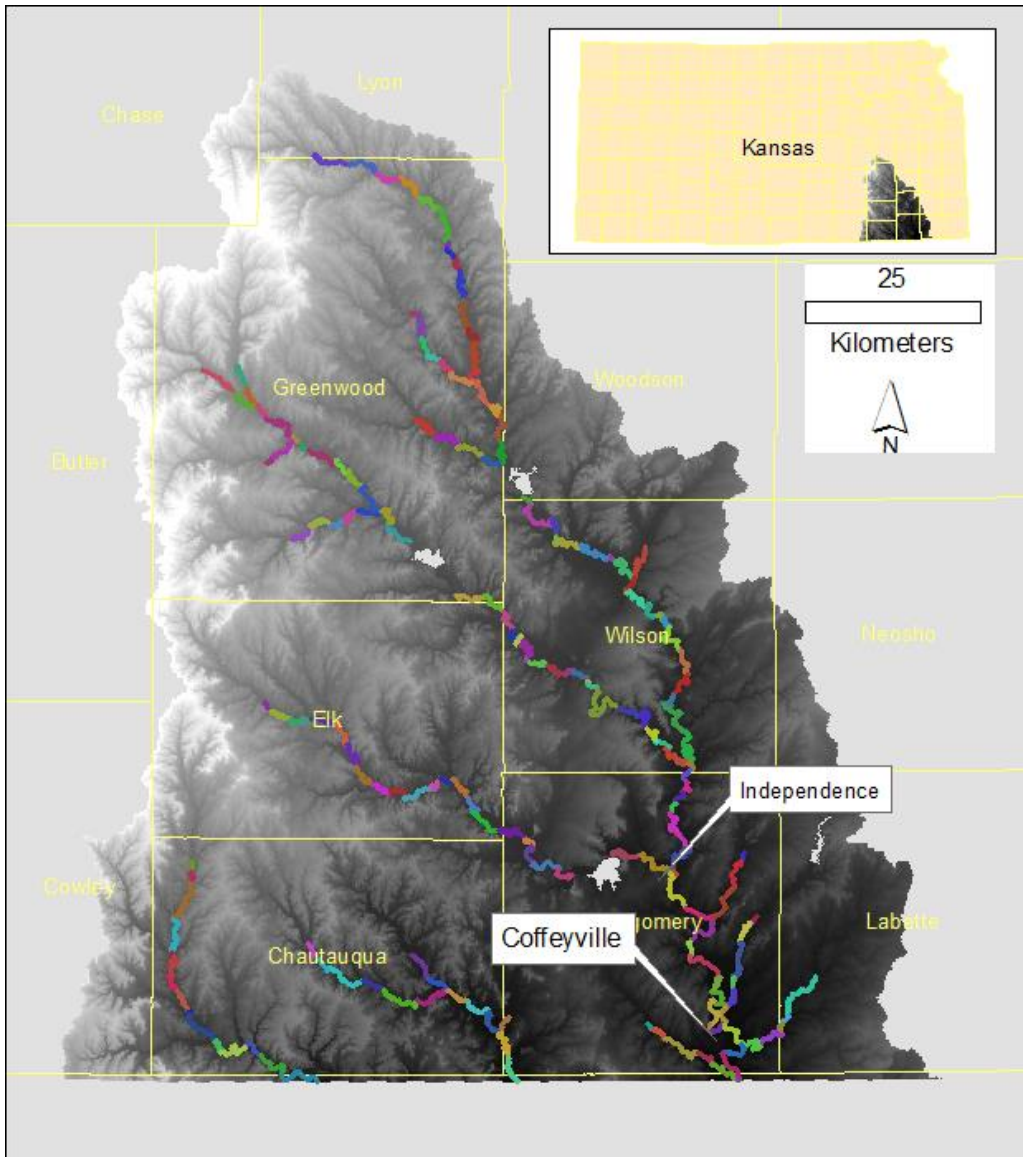

Figure 4-3: Southeast Kansas study area with 195 stream segments.

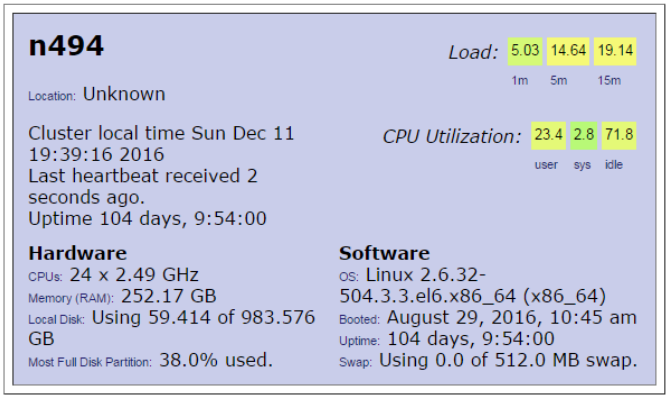

Figure 4-4: 24 core ACF node specifications. It is a Linux system running MATLAB 2016b.

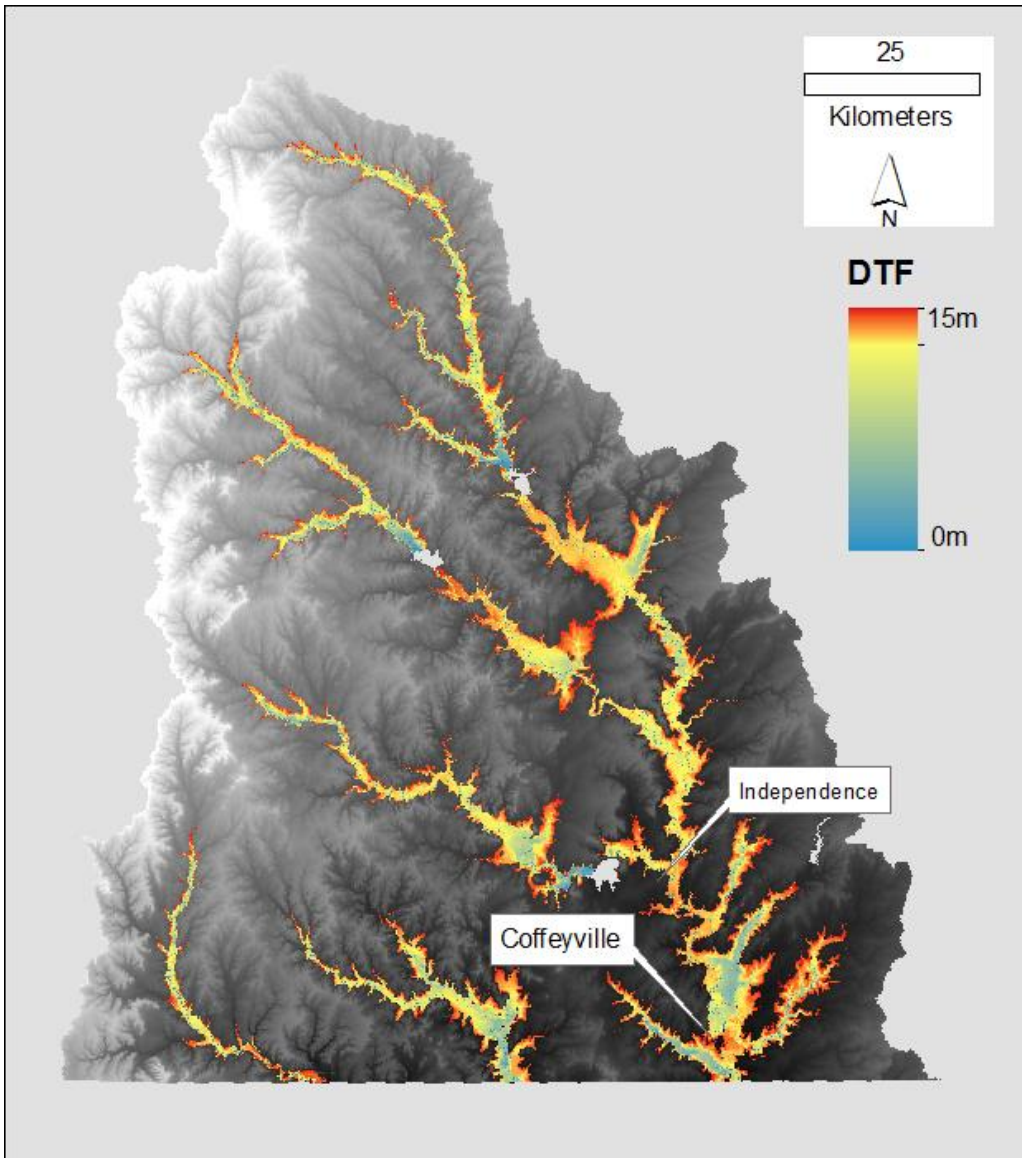

Figure 4-5: Composite 15m DTF map for 195 stream segments over the study area.

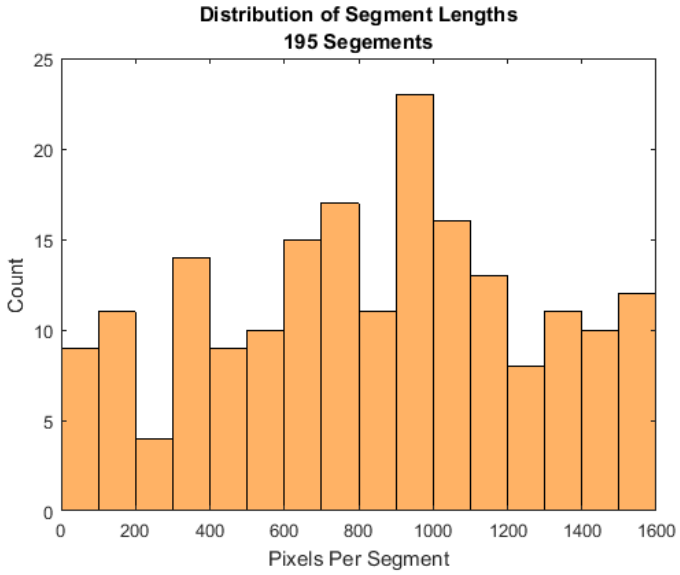

Figure 4-6: Size distribution of segment lengths in 5-mile maximum segment length set. Each stream pixel (FSP) is 5x5m. Segmentation of the synthetic stream network is performed by MATLAB code that imposes a minimum flow accumulation (FAC) of 70 square miles, with segment breaks installed at all confluences and at all other tributary inflow points with FAC value increases of 25 square miles or greater, and at additional major inflows such that maximum segment length does not exceed 5 miles. These segmentation parameters are specified by the user.

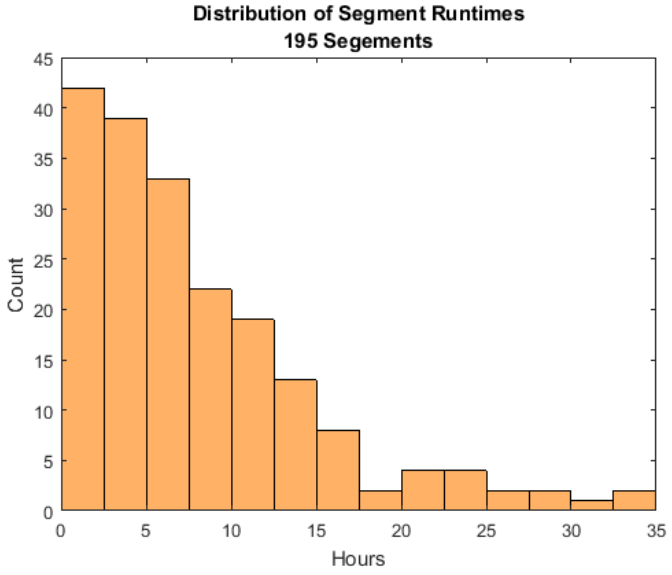

Figure 4-7: FLDPLN model runtime distribution for the 5-mile maximum segment length set.

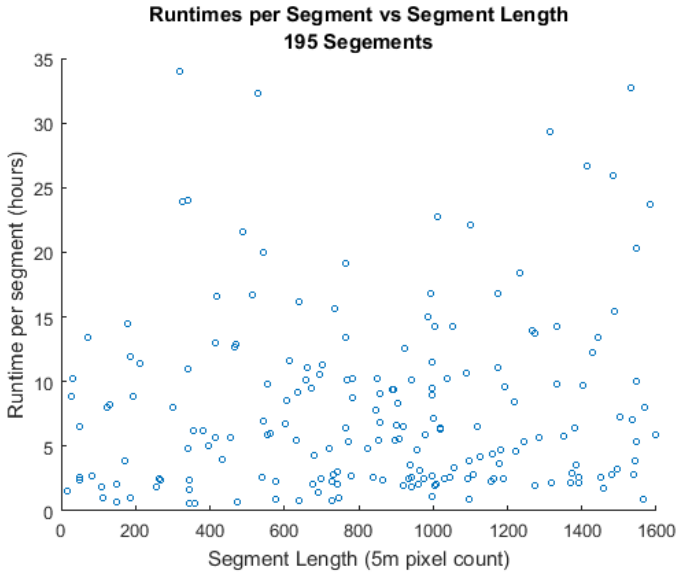

Figure 4-8: 5-mile maximum segment FLDPLN model runtime vs segment length for the study area (5m DEM). This scatter plot suggests that based on segment length alone, there is no correlation with FLPLN model runtime.

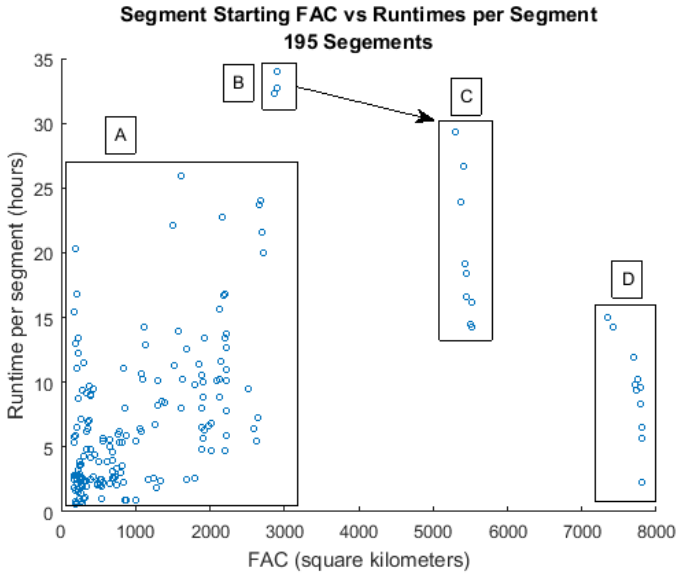

Figure 4-9: FLDPLN model runtime vs FAC scatter plot. Low FAC segments are lower order streams, which generally are situated higher in the watershed and have narrower floodplains. The grouping of segments in the lower left corner of block A represents segments in the upper reaches of the watershed with the smallest number of FPPs. Examination of the data shows that low FAC segments with longer runtimes are those that are connected directly to, or spill into larger floodplains. Blocks B and C are all associated with the junction detailed in Figure 4-15. Just downstream, these segments join those outlined in block D.

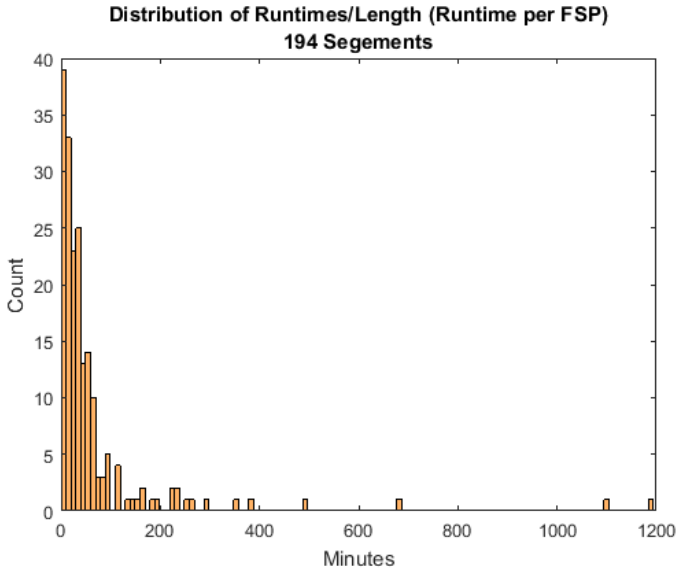

Figure 4-10: Runtime distribution of 5mi maximum length set, normalized by segment length and segment 177 removed. The anomalous segment 177 is only 5 pixels long. Inclusion of this data point significantly impacts the graphical representation of the data, so it is not included here. Further analysis of the data suggests that one should consider merging short segments with longer segments prior to FLDPLN processing.

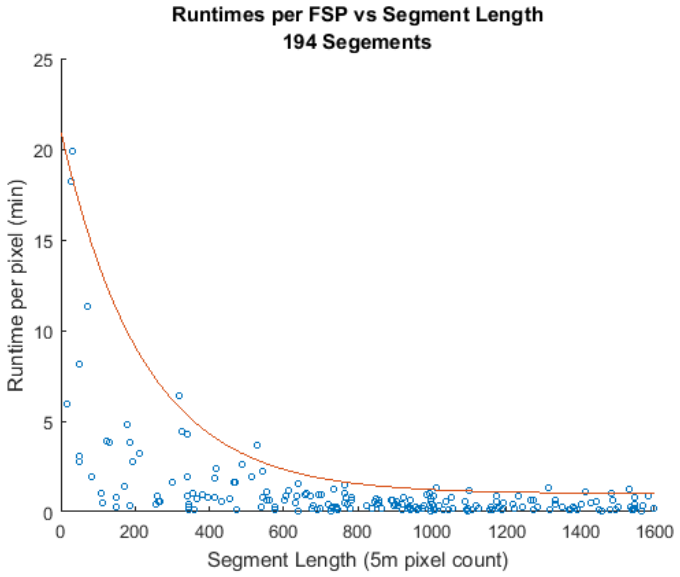

Figure 4-11: Scatter plot of runtime per FSP vs segment length. The plot shows that shorter segments are less computationally efficient. These findings suggest that, unless there are application or production requirements for shorter segments, longer segments are desirable.

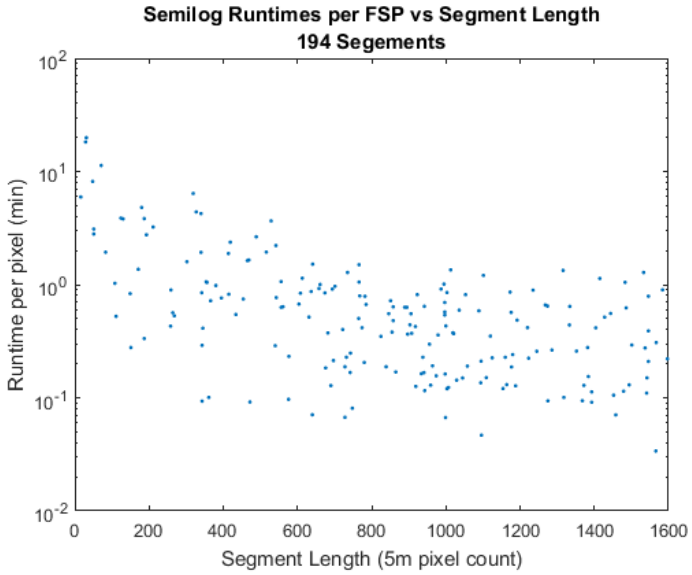

Figure 4-12: This plot shows the same data as the Figure 4-11, but the y-axis is on a log scale. This helps visualize the lower-bound envelope as well. The envelope trends are more pronounced in Figure 4-23 below.

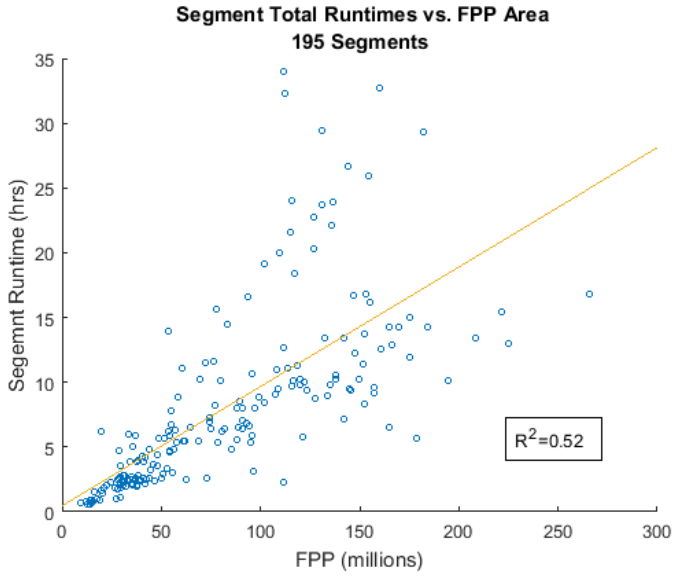

Figure 4-13: This scatter plot shows that total segment runtimes are generally proportional to the total size of the floodplain. There is a grouping of outliers in the upper middle portion of the plot. These outliers correspond to those outlined in Figures 4-27 and 4-28.

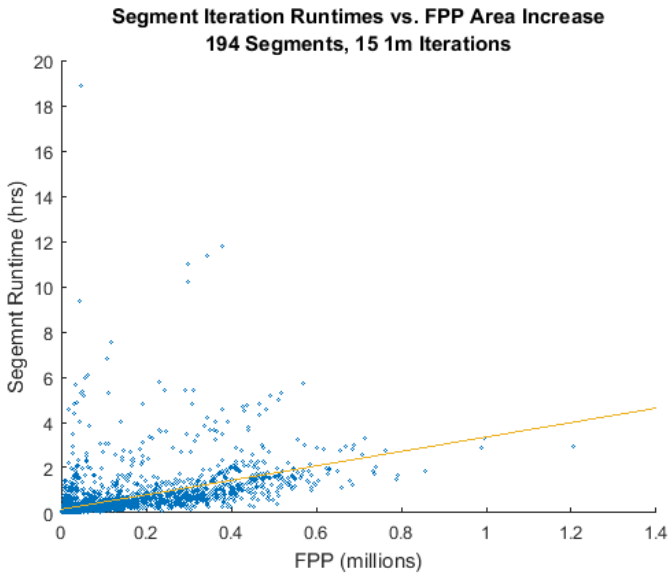

Figure 4-14: Larger increases in runtimes correspond well with increases in FPP coverage, as indicated by the linear trendline in this plot. The outliers below 250K pixels correspond to the initial filling of the stream channel, while longer runtime outliers above that value correspond to segments discussed in Figure 4-15.

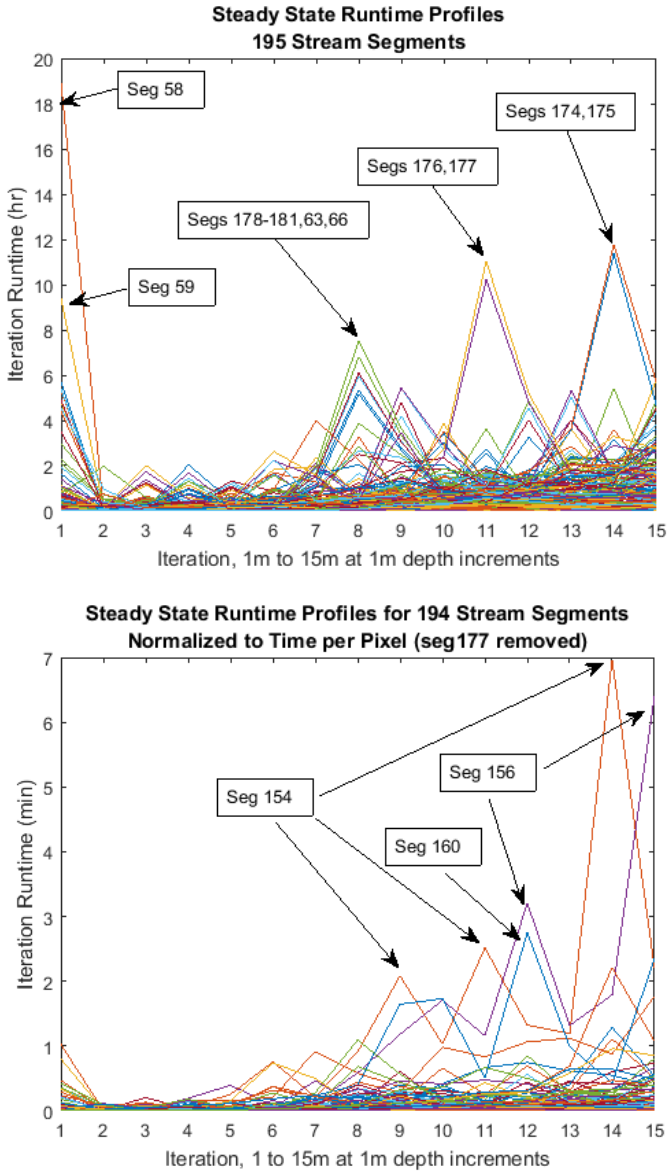

Figure 4-15: (a-top) Overall segment runtimes for each iteration are presented here. Note that the first iteration tends to be longer than the next few iterations. This is caused by the initial flooding of the stream channel across its width, followed by bank-confined water level rise. These subsequent iterations, through roughly 6m DTF, show stable, low computation cost. After 6m, the number of FPPs grows rapidly as floodwaters overbank, leading to increased computational cost. Figures 4-16 and 4-17 illustrate these segments in maps. (b-bottom) Runtimes normalized by segment length, or number of FSPs, are shown here. As with the non-normalized results, the first iteration tends to be longer than the next few iterations. This is caused by the initial flooding of the stream channel across its width. Subsequent iterations, through roughly 6m, show stable, low computation cost. This is the result of very limited lateral spreading of FPPs, which is restricted as the water is retained within the streambank. After 6m, overbanking increases and the number of FPPs grows rapidly, leading to increased computational cost. The outliers are caused by very short segment lengths, which can have the same computational cost as neighboring segments of much greater length (Figure 4-18).

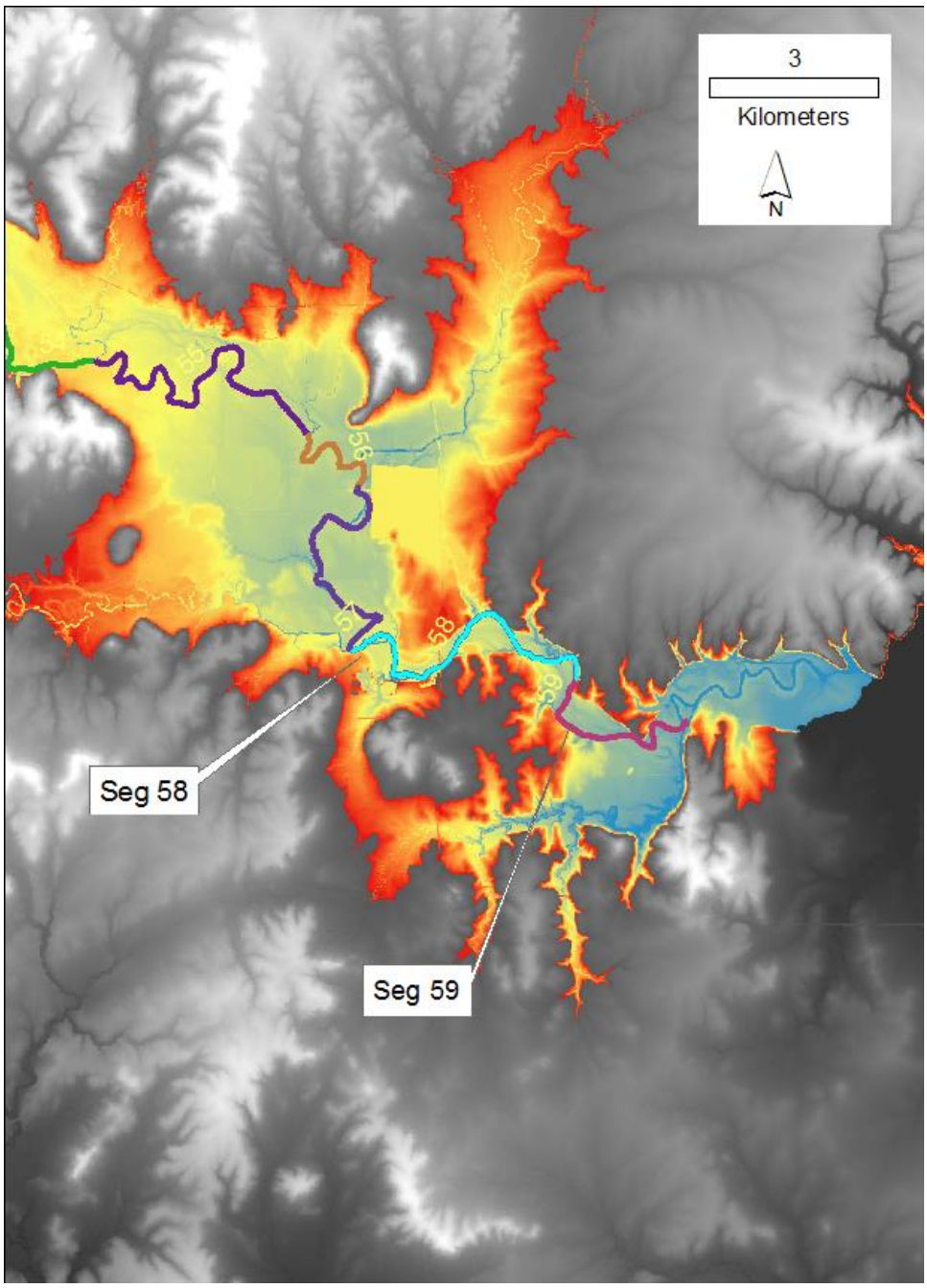

Figure 4-16: The two segments that show exceptionally long runtimes on the first iteration in Figure 4-15(a), 58 and 59, are both directly upstream of Elk City Lake. This is attributable to lake-level impacts that inflate the original lidar channel bottom elevation values.

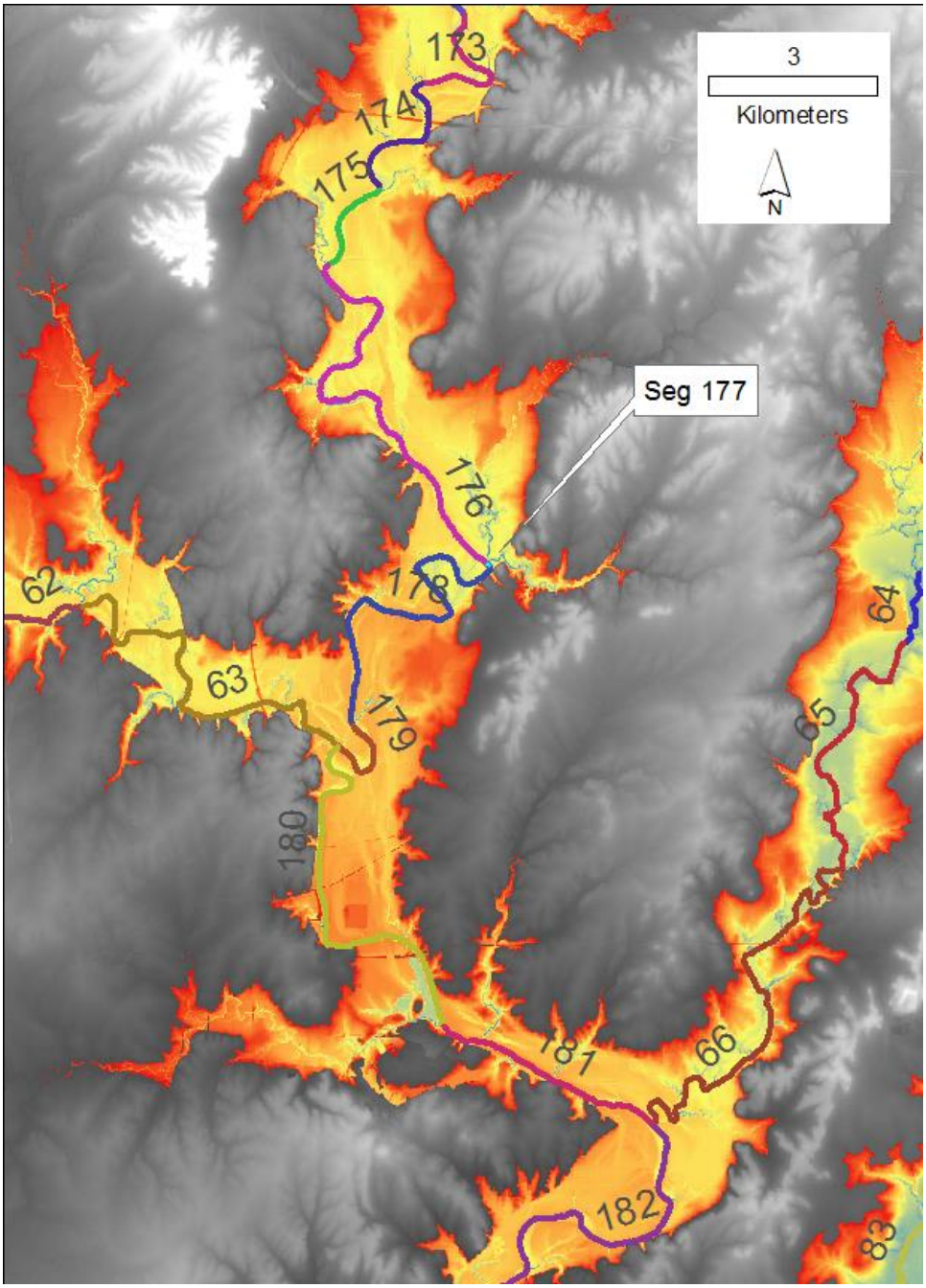

Figure 4-17: With the exception of the 1m DTF iteration, this map captures all of the long overall runtime anomalies shown in Figure 4-15(a). Segment 177 was removed in Figure 4-15(b) because it skewed the results so strongly. It serves as a good example of the inefficiency of short segments. For example, 177 has an overall runtime of 29.5 hours, where segments 176 and 178, upstream (US) and downstream (DS), respectively, have runtimes of 32.7 and 29.3 hours, respectively. The exceptionally long runtimes of segments 174 thru 181 appear to be the result of wide floodplains US and DS along with nearby intersections with tributaries that also have wide floodplains. This confluence of factors causes each of the segments to have an exceptionally large flooded area.

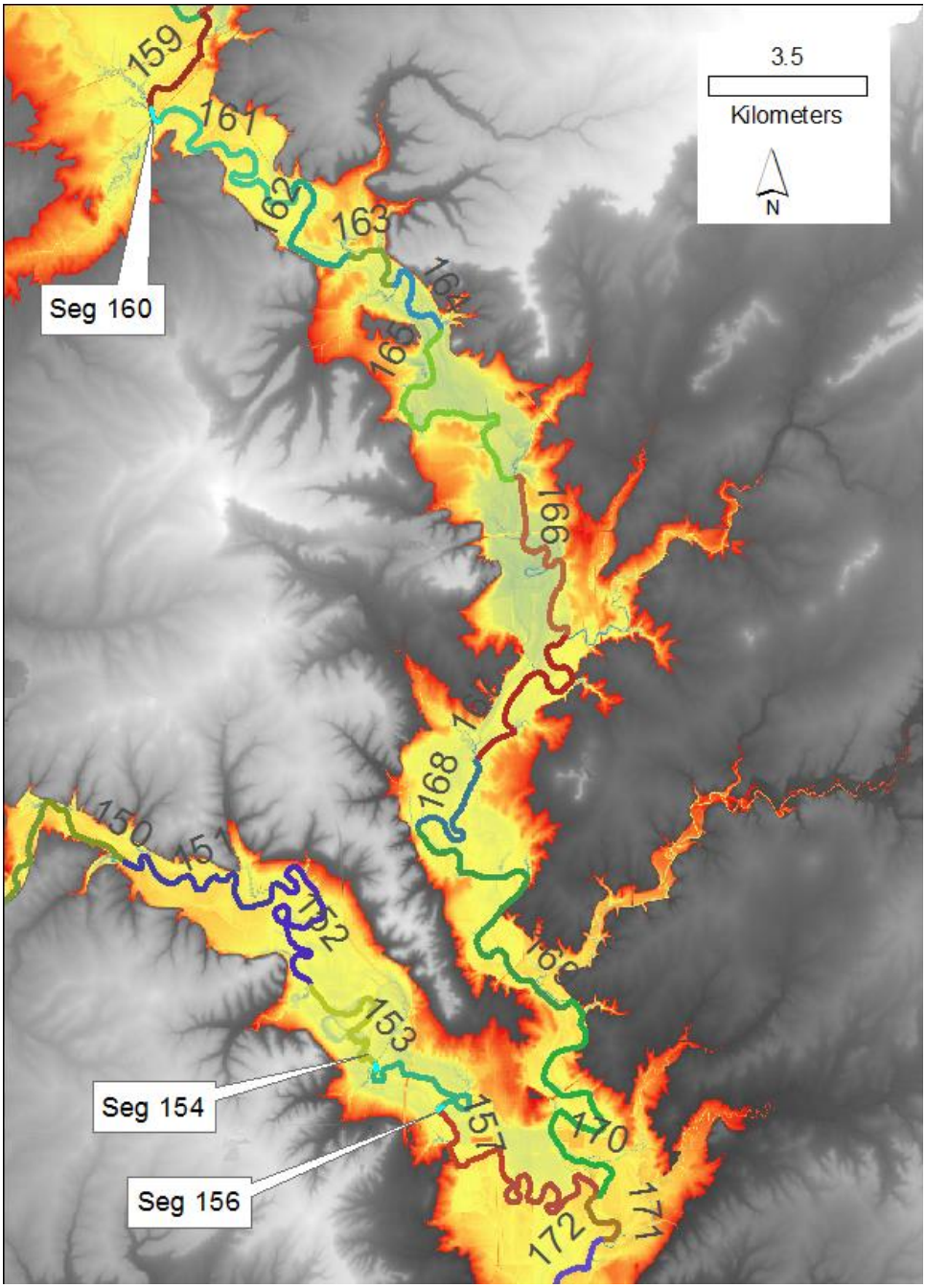

Figure 4-18: This map identifies segments that have abnormally long runtimes when normalized by the number of FSPs (Figure 4-15(b)). This is caused by very short segment lengths, which have runtimes similar to the much larger US and DS segment neighbors. Anomalous segments are highlighted in blue.

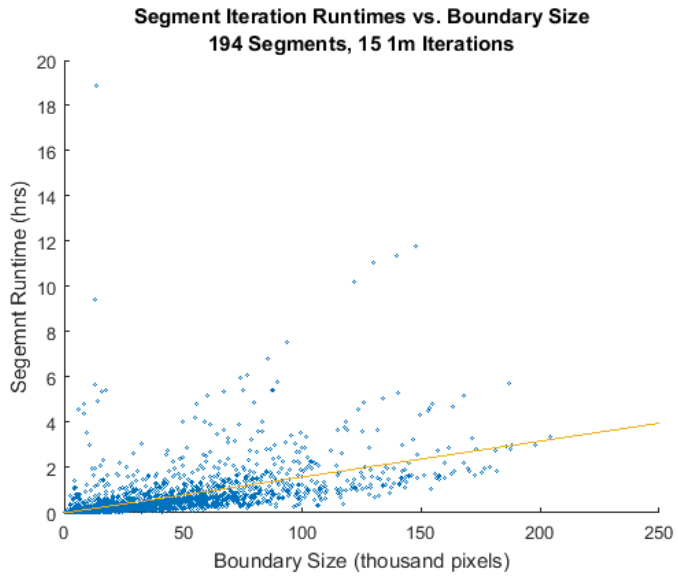

Figure 4-19: For most boundary sizes, the correlation between size and runtime is approximated with the linear trendline shown in the plot. The outliers, both in the small and mid-sized boundary range, are examined more fully in Figures 4-11 and 4-12.

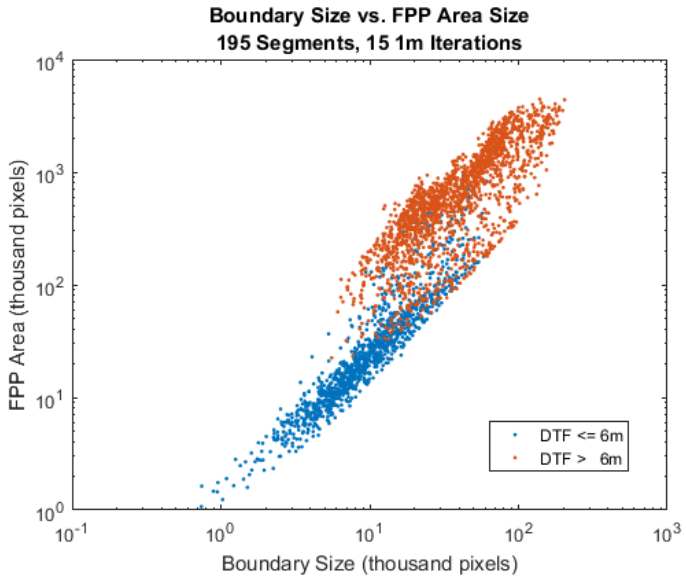

Figure 4-20: FPP vs boundary size. This log-log plot shows the relationship between boundary size and flooded area. The blue grouping, generally, shows the in-channel pixels, and the red grouping represents out of bank flood pixels.

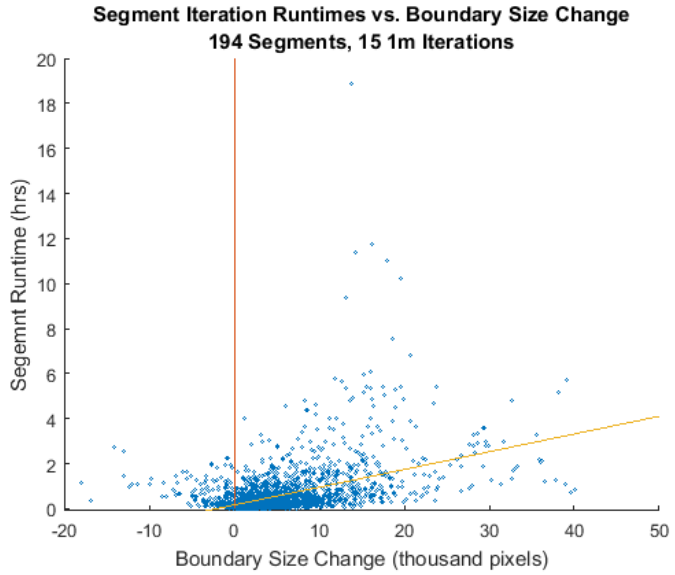

Figure 4-21: Boundary shrinks with some iterations, grows for most, and grows substantially with some. Other than outliers that occur between the 10K and 25K boundary size, which are further examined in Figures 4-16 and 4-17, there are no remarkable features in the scatter plot.

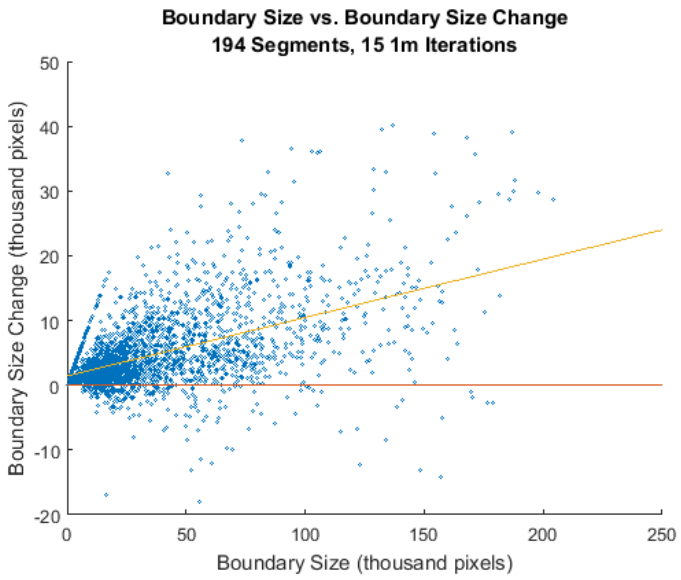

Figure 4- 22: In this scatter plot, the most noticeable feature is the linear grouping that emanates from the origin. This is an anomaly that corresponds to the identical values of the boundary size and boundary size change at the beginning of the first iteration for all segments.

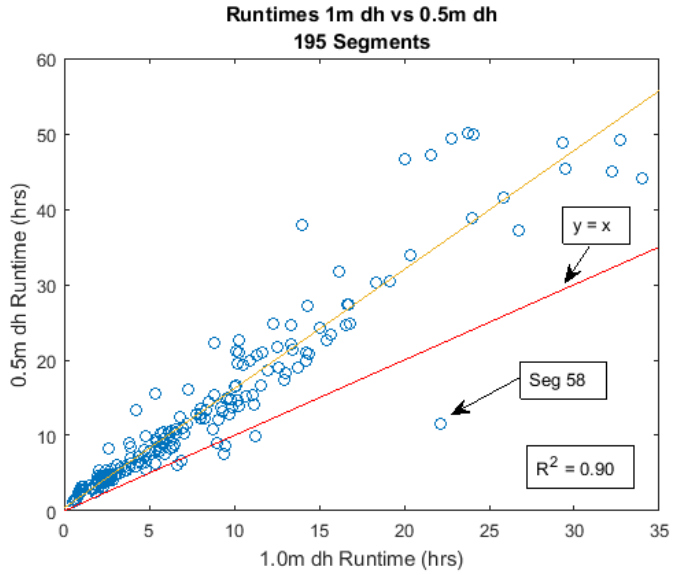

Figure 4-23: This scatter plot shows the 0.5m step size iteration takes about 1.63 times as long (yellow linear fit line) to process than using a 1m step size iteration. Although finer vertical resolution evaluation would likely expose more details of this relationship, smaller vertical DTF step sizes appear to be computationally expensive overall, but with a substantial reduction in time per iteration. For reference, the red line is shown to delineate the "break even" threshold, above which the 0.5m processing is more expensive. Curiously, there are six segments for which there is a computational advantage, those below the red line. The most notable outlier is segment is #58, which is a segment upstream of Elk City Lake. The other five also occur just upstream of reservoirs, though none with the exceptionally improved performance shown by segment #58. Considering the above-reservoir location of the outliers, processing time gains might be attributable to a greater proportion of FPPs being identified during the primary backfill step rather than during spillover.

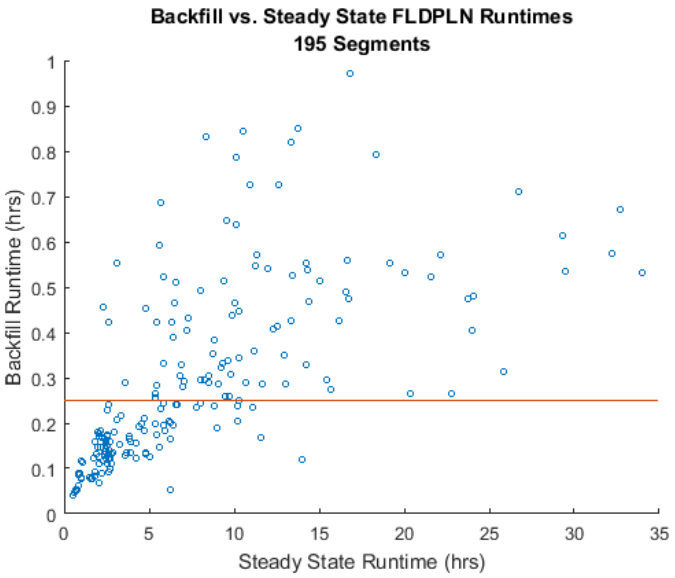

Figure 4-24: Plotting the backfill runtimes vs the steady state FLDPLN model shows that these values are weakly correlated. Backfill runtimes below 0.25 hours, however, are more

strongly correlated. This could be used to inform job sequencing in conjunction with the PARFEVAL function.

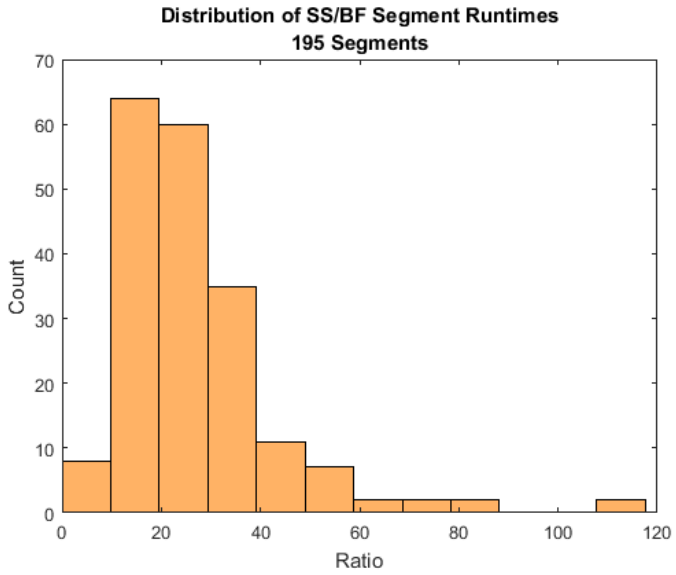

Figure 4-25: Distribution of the ratio of FPDPLN model steady state runtimes to the backfill runtimes. The median ratio is 22.8, with a minimum and maximum of 5.1 and 116.3, respectively.

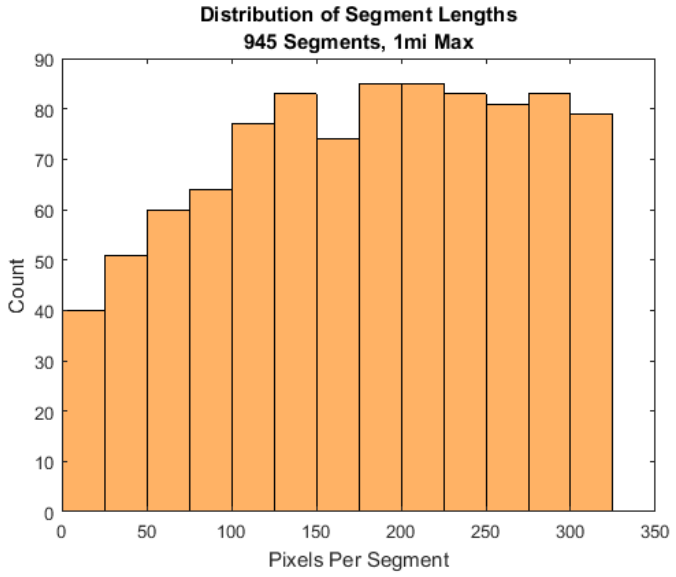

Figure 4-26: Size distribution of the 1-mile maximum segment length set. Each stream pixel (FSP) is 5x5m. Segmentation of the synthetic stream network is performed by MATLAB code that imposes a minimum flow accumulation (FAC), breaks at tributaries based on the FAC values, and a maximum segment length. These values are specified by the user.

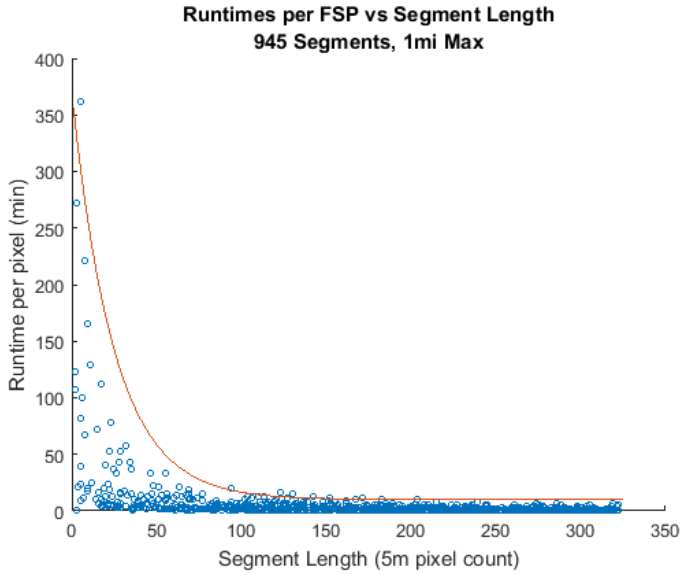

Figure 4-27: Runtimes for short segments are shown to be disproportionately long for shorter segments, which varies as a function of segment length. Computationally, the longer the segment, the more efficient the processing utilization.

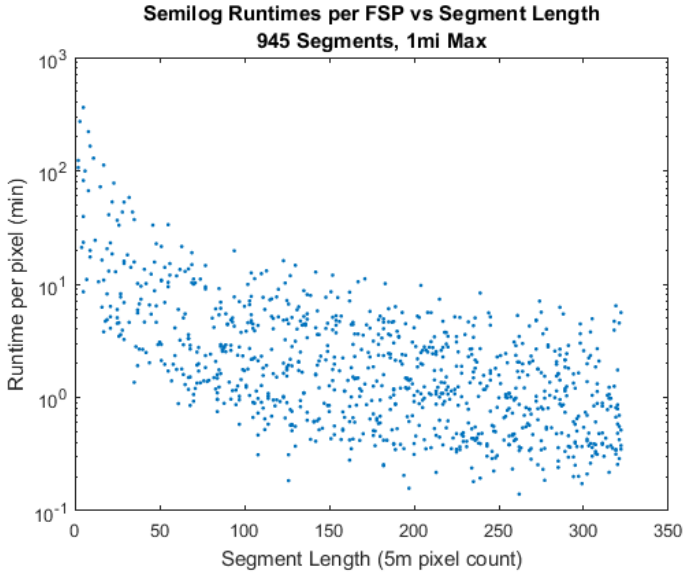

Figure 4-28: This plot shows the same data as Figure 4-27, but the y-axis is on a log scale. This helps visualize the lower-bound envelope as well. Envelope trends are more pronounced here with the larger number of samples, when compared to Figure 4-12 above.

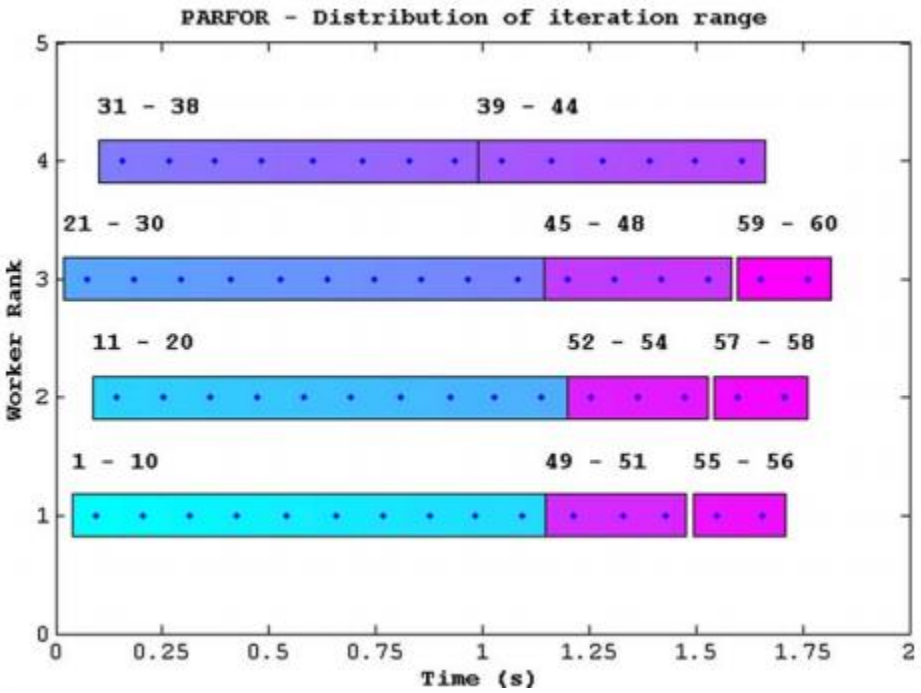

Figure 4-29 PARFOR distribution of iteration range (from Sharma and Martin, 2009). Although this graphic is a general representation of the PARFOR loop implementation, it illustrates that the initial partitioning of the index is somewhat arbitrary. Because the FLDPN model does not benefit from internal parallelization that could be efficiently used by PARFOR, this function is simply utilized at a job scheduler. A more efficient function for job scheduling is the PARFEVAL loop. The results of this implementation with the FLDPLN model are presented in Table 4-1.

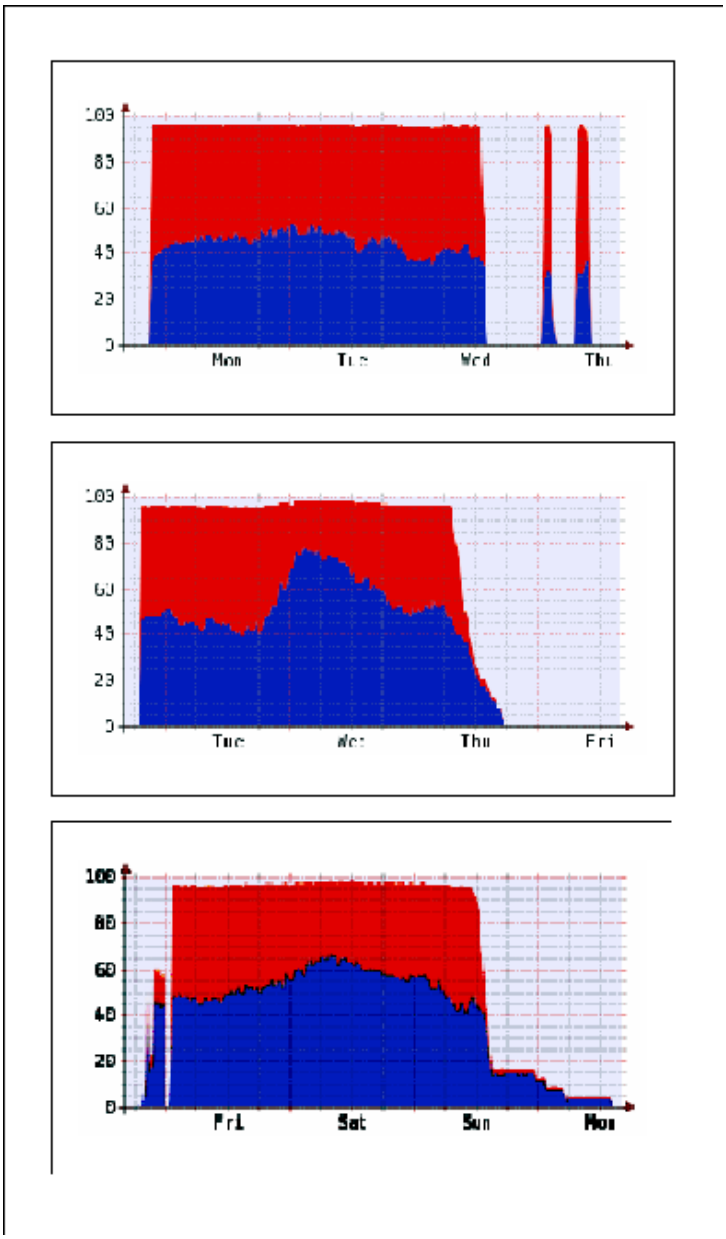

Figure 4-30: The bottom graph represents processing of 195 segments using the PARFOR loop function. The middle graph shows the same segments processing using the PARFEVAL function. Notice that there is no extended tail on the right side of the PARFEVAL graph as there is in the PARFOR graph. The top graph shows the processing of the same segments, but processed in sequence from the longest running segment to the shortest. This is the most efficient way to schedule jobs, but it requires some *a priori* knowledge of segment runtimes.

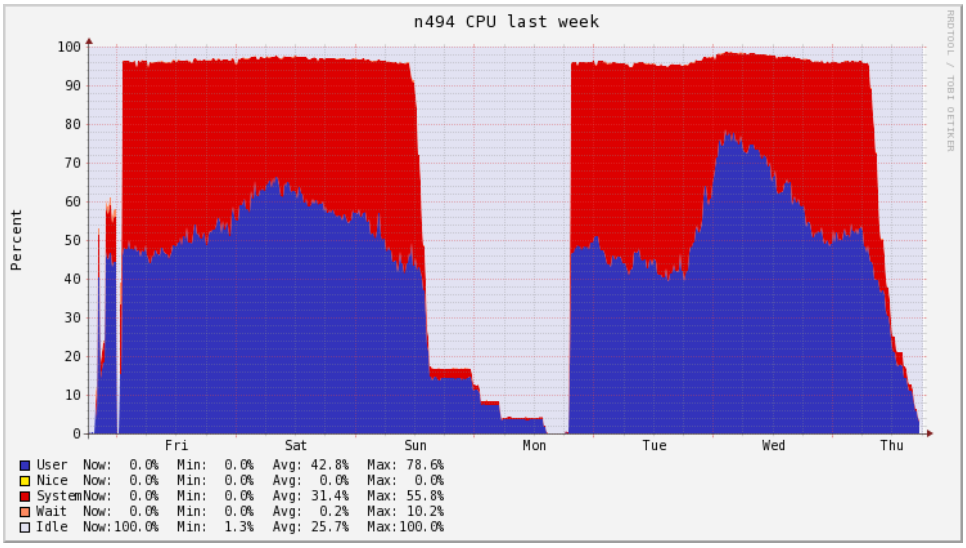

Figure 4-31: The graph on the left shows the execution of the PARFOR loop compared to the PARFEVAL loop on the right. By simply switching the parallel processing scheduling function, nearly 16.7% of the overall processing time was eliminated.

References Cited

Awadallah, A. G., & Tabet, D. (2015). Estimating flooding extent at high return period for ungauged braided systems using remote sensing: a case study of Cuvelai Basin, Angola. *Natural Hazards, 77*(1), 255-272. doi:10.1007/s11069-015-1600-6

Bates, P. D., & De Roo, A. P. J. (2000). A simple raster-based model for flood inundation simulation. *Journal of Hydrology, 236*(1-2), 54-77.

Bhatt, C. M., Rao, G. S., Diwakar, P. G., & Dadhwal, V. K. (2016). Development of flood inundation extent libraries over a range of potential flood levels: a practical framework for quick flood response. *Geomatics, Natural Hazards and Risk*, 1-18. doi:10.1080/19475705.2016.1220025

Blas, J. G., Dolz, M. F., Daniel Garcia, J., Carretero, J., Daducci, A., Aleman, Y., & Canales-Rodriguez, E. J. (2016). Porting Matlab Applications to High-Performance C++ Codes: CPU/GPU-Accelerated Spherical Deconvolution of Diffusion MRI Data. In J. Carretero, J. Garcia-Blas, R. K. L. Ko, P. Mueller, & K. Nakano (Eds.), *Algorithms and Architectures for Parallel Processing: 16th International Conference, ICA3PP 2016, Granada, Spain, December 14-16, 2016, Proceedings* (pp. 630-643). Cham: Springer International Publishing.

Brakenridge, R., & Anderson, E. (2006). MODIS-BASED FLOOD DETECTION, MAPPING AND MEASUREMENT: THE POTENTIAL FOR OPERATIONAL HYDROLOGICAL APPLICATIONS. In J. Marsalek, G. Stancalie, & G. Balint (Eds.), *Transboundary Floods: Reducing Risks Through Flood Management* (pp. 1-12). Dordrecht: Springer Netherlands.

Davies, D. K., Murphy, K. J., Michael, K., Becker-Reshef, I., Justice, C. O., Boller, R., . . . Morin, P. J. (2015). The Use of NASA LANCE Imagery and Data for Near Real-Time Applications. In C. D. Lippitt, D. A. Stow, & L. L. Coulter (Eds.), *Time-Sensitive Remote Sensing* (pp. 165-182). New York, NY: Springer New York.

De Groeve, T. (2010). Flood monitoring and mapping using passive microwave remote sensing in Namibia. *Geomatics, Natural Hazards and Risk, 1*(1), 19-35. doi:10.1080/19475701003648085

Dobbs, K. E. (2010). *Evaluation of the USGS national elevation dataset and the Kansas Biological Survey's FLDPLN ("floodplain") model for inundation extent estimation.* (1477630 M.A.), University of Kansas, Ann Arbor. Dissertations & Theses @ University of Kansas; ProQuest Dissertations & Theses Global database.

Dyer, J. M., & McClelland, J. (2017). Paradigm Change in Earth Observation - Skybox Imaging and SkySat-1. In S. Hatton (Ed.), *Proceedings of the 12th Reinventing Space Conference* (pp. 69-89). Cham: Springer International Publishing.

Giachetta, R. (2015). A framework for processing large scale geospatial and remote sensing data in MapReduce environment. *Computers & graphics, 49*, 37-46. doi:10.1016/j.cag.2015.03.003

Gomez, C., & Purdie, H. (2016). UAV- based Photogrammetry and Geocomputing for Hazards and Disaster Risk Monitoring – A Review. *Geoenvironmental Disasters, 3*(1), 23. doi:10.1186/s40677-016-0060-y

Graham, R. L. (1969). Bounds on Multiprocessing Timing Anomalies. *SIAM Journal on Applied Mathematics, 17*(2), 416-429. doi:10.1137/0117039

Grimaldi, S., Li, Y., Pauwels, V. R. N., & Walker, J. P. (2016). Remote Sensing-Derived Water Extent and Level to Constrain Hydraulic Flood Forecasting Models: Opportunities and Challenges. *Surveys in Geophysics, 37*(5), 977-1034. doi:10.1007/s10712-016-9378-y

Kastens, J. H. (2008). *Some New Devolopments On Two Separate Topoics: Statistical Cross Validation and Floodplain Mapping.* (Mathematics Dissertation), The University of Kansas, Lawrence.

Kastens, J. H., Dobbs, K. E., & Luna, M. (2010). Reconstructing the Texas Flood of 1938. Retrieved from http://kars.ku.edu/geodata/maps/reconstructing-texas-flood-1938/

Li, X., Grady, C. J., & Peterson, A. T. (2014). Delineating Sea Level Rise Inundation Using a Graph Traversal Algorithm. *Marine Geodesy, 37*(2), 267-281. doi:10.1080/01490419.2014.902884

Murphy, K. J., Davies, D. K., Michael, K., Justice, C. O., Schmaltz, J. E., Boller, R., . . . Wong, M. M. (2015). LANCE, NASA's Land, Atmosphere Near Real-Time Capability for EOS. In C. D. Lippitt, D. A. Stow, & L. L. Coulter (Eds.), *Time-Sensitive Remote Sensing* (pp. 113-127). New York, NY: Springer New York.

NASA. (2017). Surface Water & Ocean Topography (SWOT) Retrieved from https://swot.jpl.nasa.gov/mission/

Policelli, F., Slayback, D., Brakenridge, B., Nigro, J., Hubbard, A., Zaitchik, B., . . . Jung, H. (2017). The NASA Global Flood Mapping System. In V. Lakshmi (Ed.), *Remote Sensing of Hydrological Extremes* (pp. 47-63). Cham: Springer International Publishing.

Prigent, C., Lettenmaier, D. P., Aires, F., & Papa, F. (2016). Toward a High-Resolution Monitoring of Continental Surface Water Extent and Dynamics, at Global Scale: from GIEMS (Global Inundation Extent from Multi-Satellites) to SWOT (Surface Water Ocean Topography). In A. Cazenave, N. Champollion, J. Benveniste, & J. Chen (Eds.), *Remote Sensing and Water Resources* (pp. 149-165). Cham: Springer International Publishing.

Williams, B. S., D'Amico, E., Kastens, J. H., Thorp, J. H., Flotemersch, J. E., & Thoms, M. C. (2013). Automated riverine landscape characterization: GIS-based tools for watershed-scale research, assessment, and management. *Environmental Monitoring and Assessment, 185*(9), 7485-7499. doi:10.1007/s10661-013-3114-6

Witjes, N., Olbrich, P., & Rebasso, I. (2017). Big Data from Outer Space: Opportunities and Challenges for Crisis Response. In C. Al-Ekabi, B. Baranes, P. Hulsroj, & A. Lahcen (Eds.), *Yearbook on Space Policy 2015: Access to Space and the Evolution of Space Activities* (pp. 215-225). Vienna: Springer Vienna.

Xue, X., Hong, Y., Limaye, A. S., Gourley, J. J., Huffman, G. J., Khan, S. I., . . . Chen, S. (2013). Statistical and hydrological evaluation of TRMM-based Multi-satellite Precipitation Analysis over the Wangchu Basin of Bhutan: Are the latest satellite precipitation products 3B42V7 ready for use in ungauged basins? *Journal of Hydrology, 499*, 91-99. doi:http://dx.doi.org/10.1016/j.jhydrol.2013.06.042

Young, A. (2015). Reducing the Cost to Low-Earth Orbit for Small Satellites *The Twenty-First Century Commercial Space Imperative* (pp. 59-67). Cham: Springer International Publishing.

Yuan, C., Liu, Z., & Zhang, Y. (2017). Aerial Images-Based Forest Fire Detection for Firefighting Using Optical Remote Sensing Techniques and Unmanned Aerial Vehicles. *Journal of Intelligent & Robotic Systems*, 1-20. doi:10.1007/s10846-016-0464-7

CHAPTER 5

SUMMARY

Even within the past few years there have been rapid advances in the data availability, information delivery mechanisms, and response coordination that is enabling new integration of geospatial information into disaster response workflows. While some of the datasets that support global scale integration of novel approaches are not yet available, many significant improvements are fast approaching. Indeed, the time is right for developing the techniques and infrastructure that will support these applications. Understanding that there is no "one size fits all" approach to flood mapping, the methods presented in this work are designed with an awareness of 1) specific applications of derived inundation extent estimates, 2) the data quality needs of those applications, 3) the timeline within which delivery of the information is useful, and the format and delivery mechanisms that are needed.

Interpolation Comparison

In the US, gage-based implementation of FLDPLN model flood extents estimates is facilitated by the relatively high density of gaged stream. Methods for interpolation of DTF values between gaged locations were evaluated along the Verdigris River in Montgomery County, Kansas, between gage locations in Independence, Kansas, and Coffeyville, Kansas. HEC-RAS 2D modeled WSE was used to determine gage-specific DTF values for two discharge levels that represent a moderate, 1K cms flood and an extreme, 4.8K cms discharge flood.

Horizontal and vertical interpolation of DTF values between the gage locations were calculated for both flood levels and used to produce custom flood extents estimates using FLDPLN model DTM profile methods. The resulting flood extents were compared, pixel for pixel, with the output of the HEC-RAS 2D model and correspondence was measured using an F-statistic. The HEC-RAS WSE profiles and FLDPLN DTM profiles were also plotted and inspected visually for correspondence.

The results indicate that there is little difference between correspondence, using F-statistic as a measure, between the vertical and horizontal interpolation approaches. The conditioned interpolation analysis showed that extrapolating the 1K cms profile upward to estimate the 4.8K cms DTF profile gave good results, but this may be due to the fact that larger floods are less sensitive to inaccuracies in the DTF profile. Use of the 4.8K cms DTF profile to condition the 1K profile did not perform well because the conditioned profile was below bankfull, which resulted in a larger underestimation of flooding. The best results were achieved when a 500 cms DTF profile was used as a lower bound, and the 4.8K DTF profile was use as the upper bound. This does, of course, require the use of another model, but it may be possible to use imagery-derived boundary points to achieve a similar effect, but that would require further study.

Sensitivity Analysis

One application that shows great promise is the integration of remote sensing data acquired during a flood event, or shortly after peak flooding, with the FLDPLN model output. Operationally, given DEM inputs of sufficiently quality

that can be utilized as inputs to the FLDPLN model, along with co-registered remote sensing data, flood boundary points could be used to create a SLIE DTF profile that could be used to create custom flood extent estimates. This concept was tested with simulated flood boundary points (SBP) derived from HEC-RAS 2D models for two flood levels, a 1K cms and a 4.8K cms discharge representing moderate and extreme flooding within the study area.

Random selections of SBPs were generated for both flood scenarios at increments of 5-100 SBS, at 5 point increments, 100-100 SBPs at 100 point increments, and 100-10,000 points at 1000 point increments. For each point level, 100 randomized samples were tested. For each sample, the DTF values of the SBP were related to the corresponding FSP. Intermediate DTF values were calculated for all intermediate FSP. The full DTF profile was then used to generate custom flood extent estimates for each simulation. Each corresponding flood extent estimate was evaluated against the corresponding HEC-RAS 2D flood extent, using the F-statistic. For each flood scenario, 1k and 4.8k cms, 4000 SBP samples were evaluated, ranging from 5 SBPs to 10,000 SBPs. The results show there is an asymptotic upper limit to the level of correspondence that is achievable, regardless of the number of SBPs selected. Furthermore, greater correspondence is achievable at higher flood levels than lower flood levels. For the 1K cms and 4.8K cms discharger levels, average upper limit achievable was 86.7 and 96.9, respectively. More remarkable though, is that with only 5 SBPs the average F-statistic is 67.1 and 90.7, with ranges between 48.5 to 79.1 and 80.0 and 94.6, respectively. For 100 SBPs the averages are 83.5 and 96.0, ranging

from to 80.9 and 85.4 and 93.8 and 96.6, respectively. The finding then, is that with a modicum of input flood boundary points, this method can yield good results for inundation estimates. This has important implications for reducing the amount of analyst time and effort necessary for flood inundation mapping, and points toward opportunities for automated flood mapping using image classification techniques.

FLDPLN Model Performance Profiling

Because this study aims to make headway toward development of new, operational, real-time flood mapping tools and systems, key motivations of the author are wide area production of pre-built SLIE databases and the understanding of user needs that will drive SLIE application development. Efficient computational workflows are a key component to building production capacity that can support user needs. To pursue funding opportunities that support continental to global-scale production of SLIE databases, it is critical that production time and cost estimates can be estimated and articulated accurately, and ultimately be improved where possible.

Toward these goals, the FLDPLN model computational performance was profiled to gain insight into the runtime requirements and internal model variable size behavior under a set of three parameterization scenarios. The key measures that were collected on each model run were 1) computation time during each DTF iteration for each stream segment, 2) the number of pixels inundated within each iteration, and 3) the size of the flood boundary (in pixels) at the end of each iteration. These key measures and a range of derivative relationships were

explored to better understand the performance characteristics of the model as well as how the model behaves when presented with typical input data across a range of parameterizations.

Four parameterization scenarios were studied: 1) 195 stream segments with a maximum length of 5-miles, a minimum flow accumulation of 70 mi^2, segment breaks at flow accumulation discontinuities of greater than 25 mi^2, and DTF increment processing of 1m, 2) 195 stream segments, as described above, but with 0.5m DTF increment processing, 3) 945 segments with a maximum stream length of 1-mile and otherwise parameterized as in the first scenario, and 4) the backfill-only implementation of scenario #1. All scenarios were conducted over the same study are in Southeast Kansas in the Verdigris River and Caney River watersheds, which comprises a 11,455 km^2 area.

The results showed that in general, from an overall computational efficiency perspective, shorter segments are less computationally efficient than longer segments. In fact, for segments of only a few pixels the runtimes can be nearly the same as for segments that are several hundred times as long. The implications for this are that, unless otherwise necessary, stream segmentation should favor longer segments unless there are application-specific reasons for shorter segmentation. The results also showed that segments immediately upstream of reservoirs can have exceptionally long runtimes due to areas that encounter wide lateral spreading of inundation. Current best practices already eliminate segments that lie directly on lakes and reservoirs, so there are no immediate insights into how to remedy this anomalous behavior. The halving of

the DTF size parameters showed that overall runtimes are increased by a factor of 1.6, which implies that, unless there are application-specific or output data quality considerations, larger DTF iterations are less computationally expensive. The current 1m DTF iteration step size practice is the result of trial and error, but may need to be examined more closely for optimization for wide area production.

Backfill-only runtimes vs steady-state runtimes showed stronger correlation for shorter runtime, but are weakly correlated for longer runtimes. The backfill-only runtimes for the full DTF processing were only about 4% of the steady-state runtimes. A stronger correlation could inform workflow design, particularly if longer runtime segments could be identified as a way to schedule distributed desktop production segment processing. There may be sufficient information in this approach to make incremental improvements, but this needs further study. For HPC processing, the relationship does not appear to be strong enough to inform accurate estimation of 'walltime' request in PBS scripts.

Examination of the PARFOR vs PARFEVAL MATLAB functions shows that, for distributed desktop production, efficiencies are possible through the utilization of the PARFEVAL function over the PARFOR function. For the test data, an improvement of 16.7% was observed with unordered segments, and an improvement of 23.7% was observed for model runs where segments were ordered from longest running to shortest running. In practice, however, *a priori* knowledge of segment runtimes is not available, unless informed by preprocessing of backfill-only runtime or other mechanisms that have not yet been identified.

Current and Future Research

The availability of improved DEM inputs presents opportunities for evaluation of applications presented in this research, and others, both in the US and abroad. DEM quality within the US will be driven by the 3DEP program of the USGS, which aims to make lidar quality DEM data available across the continental US that are updated on an 8-year cycle, which is unprecedented. For global data, the forthcoming availability of TREx data, derived from TanDEM-X and TerraSAR-X data, also presents unprecedented availability of global DEM data of sufficient quality to support novel applications. Other datasets, including VRICON DEM data, JAXA ALOS 3D data, and others represent new opportunities for FLDPLN model synergies that have not been possible in the past.

Some of the synergies between the FLDLN model and other inputs, presented in the conceptual framework, have been explored in this study, but there are others that are valid lines of inquiry also. The work of the Global Flood Partnership, spearheaded by the Dartmouth Flood Observatory and the European Commission Joint Research Centre, is focused on exploiting synergies between global flood modeling and monitoring efforts to create timely and relevant products that support the needs of the disaster response community. It is the view of this author that the FLDPLN model and the SLIE databases that are derived from it can be an important contribution to this effort. For instance, SLIE data could be coupled with GFDS data to offer refined estimates of flood impacts over those which are derivable by the GFDS alone. The NASA near real-time MODIS flood data could be refined with SLIE libraries to offer a terrain-based representation of

MODIS-derived flood data that more accurately represents actual flood extents. Domestically, gage data could be coupled with SLIE data, which is the focus of current efforts with Riverside Technology, Inc. The anticipated abundance of remotely sensed data that will be available via commercial smallsats will be certainly be an area to explore in greater detail given the positive results of the simulated boundary point application presented in the study.

The greater, long-term vision motivating the author has been to produce continental to global scale SLIE libraries built with the best available DEMS, and that are operationally integrated with applications that improve that quality and timeliness of flood disaster response. The novel nature of this approach to flood mapping has presented challenges, at time, because it is non-traditional in nature and represents a fundamental departure from the way that things have been done for decades. It is hoped that the results of this studies presented here will make headway toward gaining support for advancing the ideas presented.

References Cited

Abdullah, Q. A. (2016). A Star is Born: The State of New Lidar Technologies. *Photogrammetric Engineering & Remote Sensing, 82*(5), 307-312. doi:10.14358/PERS.82.5.307

Adhikari, P., Hong, Y., Douglas, K. R., Kirschbaum, D. B., Gourley, J., Adler, R., & Robert Brakenridge, G. (2010). A digitized global flood inventory (1998–2008): compilation and preliminary results. *Natural Hazards, 55*(2), 405-422. doi:10.1007/s11069-010-9537-2

Awadallah, A. G., & Tabet, D. (2015). Estimating flooding extent at high return period for ungauged braided systems using remote sensing: a case study of Cuvelai Basin, Angola. *Natural Hazards, 77*(1), 255-272. doi:10.1007/s11069-015-1600-6

Bates, P. D., & De Roo, A. P. J. (2000). A simple raster-based model for flood inundation simulation. *Journal of Hydrology, 236*(1-2), 54-77.

Becek, K., & Becek, K. Evaluation of Vertical Accuracy of the WorldDEM™ Using the Runway Method. *Remote sensing (Basel, Switzerland), 8*(11), 934. doi:10.3390/rs8110934

Bhatt, C. M., Rao, G. S., Diwakar, P. G., & Dadhwal, V. K. (2016). Development of flood inundation extent libraries over a range of potential flood levels: a practical framework for quick flood response. *Geomatics, Natural Hazards and Risk*, 1-18. doi:10.1080/19475705.2016.1220025

Blas, J. G., Dolz, M. F., Daniel Garcia, J., Carretero, J., Daducci, A., Aleman, Y., & Canales-Rodriguez, E. J. (2016). Porting Matlab Applications to High-Performance C++ Codes: CPU/GPU-Accelerated Spherical Deconvolution of Diffusion MRI Data. In J. Carretero, J. Garcia-Blas, R. K. L. Ko, P. Mueller, & K. Nakano (Eds.), *Algorithms and Architectures for Parallel Processing: 16th International Conference, ICA3PP 2016, Granada, Spain, December 14-16, 2016, Proceedings* (pp. 630-643). Cham: Springer International Publishing.

Brakenridge, R., & Anderson, E. (2006). MODIS-BASED FLOOD DETECTION, MAPPING AND MEASUREMENT: THE POTENTIAL FOR OPERATIONAL HYDROLOGICAL APPLICATIONS. In J. Marsalek, G. Stancalie, & G. Balint (Eds.), *Transboundary Floods: Reducing Risks Through Flood Management* (pp. 1-12). Dordrecht: Springer Netherlands.

Capitol, S. t. (2016, 2016/06/03/). New Remote Sensing Findings from University of Minnesota Described [An automated, open-source pipeline for mass production of digital elevation models (DEMs) from very-high-resolution commercial stereo satellite imagery], Article. *Skirting the Capitol,* p. 1904. Retrieved from http://go.galegroup.com.www2.lib.ku.edu/ps/i.do?p=EAIM&sw=w&u=ksstate_ukans&v=2.1&it=r&id=GALE%7CA453716187&asid=ec95f9bd9f5b2944d72b0d3d503ecc84

Cook, A., & Merwade, V. (2009a). Effect of topographic data, geometric configuration and modeling approach on flood inundation mapping. *Journal of Hydrology, 377*(1–2), 131-142. doi:http://dx.doi.org/10.1016/j.jhydrol.2009.08.015

Cook, A., & Merwade, V. (2009b). Effect of topographic data, geometric configuration and modeling approach on flood inundation mapping. *Journal of Hydrology, 377*(1/2), 131-142.

Coveney, S. (2013). Land Cover Dependent Error in Intermap IFSAR DTM. *Photogrammetric Engineering & Remote Sensing, 79*(3), 277-286. doi:10.14358/PERS.79.3.277

Coxon, G., Freer, J., Westerberg, I. K., Wagener, T., Woods, R., & Smith, P. J. (2015). A novel framework for discharge uncertainty quantification applied to 500 UK gauging stations. *Water Resources Research, 51*(7), 5531-5546. doi:10.1002/2014WR016532

Davies, D. K., Murphy, K. J., Michael, K., Becker-Reshef, I., Justice, C. O., Boller, R., . . . Morin, P. J. (2015). The Use of NASA LANCE Imagery and Data for Near Real-Time Applications. In C. D. Lippitt, D. A. Stow, & L. L. Coulter (Eds.), *Time-Sensitive Remote Sensing* (pp. 165-182). New York, NY: Springer New York.

De Groeve, T. (2010). Flood monitoring and mapping using passive microwave remote sensing in Namibia. *Geomatics, Natural Hazards and Risk, 1*(1), 19-35. doi:10.1080/19475701003648085

Di Baldassarre, G., Schumann, G., & Bates, P. (2009). Near real time satellite imagery to support and verify timely flood modelling. *Hydrological Processes, 23*(5), 799-803. doi:10.1002/hyp.7229

Dobbs, K. E. (2010). *Evaluation of the USGS national elevation dataset and the Kansas Biological Survey's FLDPLN ("floodplain") model for inundation extent estimation.* (1477630 M.A.), University of Kansas, Ann Arbor. Dissertations & Theses @ University of Kansas; ProQuest Dissertations & Theses Global database.

Dyer, J. M., & McClelland, J. (2017). Paradigm Change in Earth Observation - Skybox Imaging and SkySat-1. In S. Hatton (Ed.), *Proceedings of the 12th Reinventing Space Conference* (pp. 69-89). Cham: Springer International Publishing.

Gall, M., Boruff, B. J., & Cutter, S. L. (2007). Assessing Flood Hazard Zones in the Absence of Digital Floodplain Maps: Comparison of Alternative Approaches. *Natural Hazards Review, 8*(1), 1-12.

Giachetta, R. (2015). A framework for processing large scale geospatial and remote sensing data in MapReduce environment. *Computers & graphics, 49*, 37-46. doi:10.1016/j.cag.2015.03.003

Gomez, C., & Purdie, H. (2016). UAV- based Photogrammetry and Geocomputing for Hazards and Disaster Risk Monitoring – A Review. *Geoenvironmental Disasters, 3*(1), 23. doi:10.1186/s40677-016-0060-y

Graham, R., & Koh, A. (2002). Digital Aerial Survey - Theory and Practice: Whittles Publishing.

Graham, R. L. (1969). Bounds on Multiprocessing Timing Anomalies. *SIAM Journal on Applied Mathematics, 17*(2), 416-429. doi:10.1137/0117039

Grimaldi, S., Li, Y., Pauwels, V. R. N., & Walker, J. P. (2016). Remote Sensing-Derived Water Extent and Level to Constrain Hydraulic Flood Forecasting Models: Opportunities and Challenges. *Surveys in Geophysics, 37*(5), 977-1034. doi:10.1007/s10712-016-9378-y

Horritt, M. S., & Bates, P. D. (2001). Effects of spatial resolution on a raster based model of flood flow. *Journal of Hydrology, 253*(1-4), 239-249.

InterMap. (2017). InterMap Data. Retrieved from http://www.intermap.com/data

Kastens, J. H. (2008). *Some New Devolopments On Two Separate Topoics: Statistical Cross Validation and Floodplain Mapping.* (Mathematics Dissertation), The University of Kansas, Lawrence.

Kastens, J. H., Dobbs, K. E., & Luna, M. (2010). Reconstructing the Texas Flood of 1938. Retrieved from http://kars.ku.edu/geodata/maps/reconstructing-texas-flood-1938/

Klemas, V. (2014). Remote Sensing of Floods and Flood-Prone Areas: An Overview. *Journal of Coastal Research*, 1005-1013. doi:10.2112/JCOASTRES-D-14-00160.1

Knebl, M. R., Yang, Z. L., Hutchison, K., & Maidment, D. R. (2005). Regional scale flood modeling using NEXRAD rainfall, GIS, and HEC-HMS/RAS: a case study for the San Antonio River Basin Summer 2002 storm event. *Journal of Environmental Management, 75*(4), 325-336. doi:http://dx.doi.org/10.1016/j.jenvman.2004.11.024

Kwak, Y., Park, J., & Fukami, K. (2014). Estimating floodwater from MODIS time series and SRTM DEM data. *Artificial Life and Robotics, 19*(1), 95-102. doi:10.1007/s10015-013-0140-y

Leon, A. S., & Goodell, C. (2016). Controlling HEC-RAS using MATLAB. *Environmental Modelling & Software, 84*, 339-348. doi:http://dx.doi.org/10.1016/j.envsoft.2016.06.026

Li, X., Grady, C. J., & Peterson, A. T. (2014). Delineating Sea Level Rise Inundation Using a Graph Traversal Algorithm. *Marine Geodesy, 37*(2), 267-281. doi:10.1080/01490419.2014.902884

Mallet, C., & Bretar, F. (2009). Full-waveform topographic lidar: State-of-the-art. *ISPRS Journal of Photogrammetry and Remote Sensing, 64*(1), 1-16. doi:http://dx.doi.org/10.1016/j.isprsjprs.2008.09.007

Mason, D. C., J-p. Schumann, G., & Bates, P. D. (2010). Data Utilization in Flood Inundation Modelling *Flood Risk Science and Management* (pp. 209-233): Wiley-Blackwell.

Mason, D. C., Schumann, G. J. P., Neal, J. C., Garcia-Pintado, J., & Bates, P. D. (2012). Automatic near real-time selection of flood water levels from high resolution Synthetic Aperture Radar images for assimilation into hydraulic models: A case study. *Remote Sensing of Environment, 124*, 705-716. doi:http://dx.doi.org/10.1016/j.rse.2012.06.017

Merwade, V., Olivera, F., Arabi, M., & Edleman, S. (2008b). Uncertainty in Flood Inundation Mapping: Current Issues and Future Directions. *Journal of Hydrologic Engineering, 13*(7), 608-620.

Moya Quiroga, V., Kure, S., Udo, K., & Mano, A. (2016). Application of 2D numerical simulation for the analysis of the February 2014 Bolivian Amazonia flood: Application of the new HEC-RAS version 5. *RIBAGUA - Revista Iberoamericana del Agua, 3*(1), 25-33. doi:http://dx.doi.org/10.1016/j.riba.2015.12.001

Murphy, K. J., Davies, D. K., Michael, K., Justice, C. O., Schmaltz, J. E., Boller, R., . . . Wong, M. M. (2015). LANCE, NASA's Land, Atmosphere Near Real-Time Capability for EOS. In C. D. Lippitt, D. A. Stow, & L. L. Coulter (Eds.), *Time-Sensitive Remote Sensing* (pp. 113-127). New York, NY: Springer New York.

NASA. (2017). Surface Water & Ocean Topography (SWOT) Retrieved from https://swot.jpl.nasa.gov/mission/

NGA. (2015). NGA, Germany's Bundeswehr Geoinformation Centre sign geospatial data sharing agreement. Retrieved from https://www.nga.mil/MediaRoom/News/Pages/NGA,-Germany%E2%80%99s-Bundeswehr-Geoinformation-Centre-sign-geospatial-data-sharing-agreement-.aspx

Noh, M.-J. (2015). Automated stereo-photogrammetric DEM generation at high latitudes: Surface Extraction with TIN-based Search-space Minimization (SETSM) validation and demonstration over glaciated regions. *GIScience and remote sensing, 52*(2), 198-217. doi:10.1080/15481603.2015.1008621

Onyango, M. A., & Uwase, M. (2017). Humanitarian Response to Complex Emergencies and Natural Disasters A2 - Quah, Stella R *International Encyclopedia of Public Health (Second Edition)* (pp. 106-116). Oxford: Academic Press.

Peterson, D. L., Whistler, J. L., Lomas, J. M., Dobbs, K. E., Jakubauskas, M. E., Egbert, S. E., & Martinko, E. A. (2008). *2005 Kansas Land Cover Patterns Phase I: Final Report*. Retrieved from

Policelli, F., Slayback, D., Brakenridge, B., Nigro, J., Hubbard, A., Zaitchik, B., . . . Jung, H. (2017). The NASA Global Flood Mapping System. In V. Lakshmi (Ed.), *Remote Sensing of Hydrological Extremes* (pp. 47-63). Cham: Springer International Publishing.

Prigent, C., Lettenmaier, D. P., Aires, F., & Papa, F. (2016). Toward a High-Resolution Monitoring of Continental Surface Water Extent and Dynamics, at Global Scale: from GIEMS (Global Inundation Extent from Multi-Satellites) to SWOT (Surface Water Ocean Topography). In A. Cazenave, N. Champollion, J. Benveniste, & J. Chen (Eds.), *Remote Sensing and Water Resources* (pp. 149-165). Cham: Springer International Publishing.

Revilla-Romero, B., Thielen, J., Salamon, P., De Groeve, T., & Brakenridge, G. R. (2014). Evaluation of the satellite-based Global Flood Detection System for measuring river discharge: influence of local factors. *Hydrol. Earth Syst. Sci., 18*(11), 4467-4484. doi:10.5194/hess-18-4467-2014

Riegler, G., & Riegler, G. (2015). WORLDDEM – A NOVEL GLOBAL FOUNDATION LAYER. *ISPRS - International Archives of the Photogrammetry, Remote Sensing and Spatial Information Sciences, XL-3/W2*, 183-187. doi:10.5194/isprsarchives-XL-3-W2-183-2015

Robert Brakenridge, G., Cohen, S., Kettner, A. J., De Groeve, T., Nghiem, S. V., Syvitski, J. P. M., & Fekete, B. M. (2012). Calibration of satellite measurements of river discharge using a global hydrology model. *Journal of Hydrology, 475*, 123-136. doi:http://dx.doi.org/10.1016/j.jhydrol.2012.09.035

Sarhadi, A., Soltani, S., & Modarres, R. (2012). Probabilistic flood inundation mapping of ungauged rivers: Linking GIS techniques and frequency analysis. *Journal of Hydrology, 458–459*, 68-86.

doi:http://dx.doi.org/10.1016/j.jhydrol.2012.06.039
Scawthorn, C., Blais, N., Seligson, H., Tate, E., Mifflin, E., Thomas, W., . . . Jones, C. (2006). HAZUS-MH Flood Loss Estimation Methodology. I: Overview and Flood Hazard Characterization. *Natural Hazards Review, 7*(2), 60-71.
Schumann, G., Hostache, R., Puech, C., Hoffmann, L., Matgen, P., Pappenberger, F., & Pfister, L. (2007). High-Resolution 3-D Flood Information From Radar Imagery for Flood Hazard Management. *IEEE Transactions on Geoscience and Remote Sensing, 45*(6), 1715-1725. doi:10.1109/TGRS.2006.888103
Tayefi, V., Lane, S. N., Hardy, R. J., & Yu, D. (2007). A comparison of one- and two-dimensional approaches to modelling flood inundation over complex upland floodplains. *Hydrological Processes, 21*(23), 3190-3202.
USGS. (2017). Interferometric Synthetic Aperture Radar (IFSAR) Alaska. Retrieved from https://lta.cr.usgs.gov/IFSAR_Alaska
Williams, B. S., D'Amico, E., Kastens, J. H., Thorp, J. H., Flotemersch, J. E., & Thoms, M. C. (2013). Automated riverine landscape characterization: GIS-based tools for watershed-scale research, assessment, and management. *Environmental Monitoring and Assessment, 185*(9), 7485-7499. doi:10.1007/s10661-013-3114-6
Witjes, N., Olbrich, P., & Rebasso, I. (2017). Big Data from Outer Space: Opportunities and Challenges for Crisis Response. In C. Al-Ekabi, B. Baranes, P. Hulsroj, & A. Lahcen (Eds.), *Yearbook on Space Policy 2015: Access to Space and the Evolution of Space Activities* (pp. 215-225). Vienna: Springer Vienna.
Wu, H., Adler, R. F., Hong, Y., Tian, Y., & Policelli, F. (2012). Evaluation of Global Flood Detection Using Satellite-Based Rainfall and a Hydrologic Model. *Journal of Hydrometeorology, 13*(4), 1268-1284. doi:doi:10.1175/JHM-D-11-087.1
Xue, X., Hong, Y., Limaye, A. S., Gourley, J. J., Huffman, G. J., Khan, S. I., . . . Chen, S. (2013). Statistical and hydrological evaluation of TRMM-based Multi-satellite Precipitation Analysis over the Wangchu Basin of Bhutan: Are the latest satellite precipitation products 3B42V7 ready for use in ungauged basins? *Journal of Hydrology, 499*, 91-99. doi:http://dx.doi.org/10.1016/j.jhydrol.2013.06.042
Yan, K., Neal, J. C., Solomatine, D. P., & Di Baldassarre, G. (2015). Chapter 4 - Global and Low-Cost Topographic Data to Support Flood Studies *Hydro-Meteorological Hazards, Risks and Disasters* (pp. 105-123). Boston: Elsevier.
Young, A. (2015). Reducing the Cost to Low-Earth Orbit for Small Satellites *The Twenty-First Century Commercial Space Imperative* (pp. 59-67). Cham: Springer International Publishing.
Yuan, C., Liu, Z., & Zhang, Y. (2017). Aerial Images-Based Forest Fire Detection for Firefighting Using Optical Remote Sensing Techniques and Unmanned Aerial Vehicles. *Journal of Intelligent & Robotic Systems*, 1-20. doi:10.1007/s10846-016-0464-7